Geological, Mineralogical and Textural Impacts on the Distribution of Environmentally Toxic Trace Elements in Seafloor Massive Sulfide Occurrences

Emily K. Fallon [1,2,]*[ID]**, Matthias Frische [3], Sven Petersen [3]**[ID]**, Richard A. Brooker [1]**[ID] and Thomas B. Scott [2]**

[1] School of Earth Sciences, University of Bristol, Bristol BS8 1RJ, UK; Richard.Brooker@bristol.ac.uk
[2] Interface Analysis Centre, School of Physics, HH Wills Physics Laboratory, University of Bristol, Bristol BS8 1TL, UK; T.B.Scott@bristol.ac.uk
[3] GEOMAR Helmholtz-Zentrum für Ozeanforschung Kiel, Wischhofstr. 1-3, 24148 Kiel, Germany; mfrische@geomar.de (M.F.); spetersen@geomar.de (S.P.)
[*] Correspondence: e.fallon@bristol.ac.uk

Abstract: With mining of seafloor massive sulfides (SMS) coming closer to reality, it is vital that we have a good understanding of the geochemistry of these occurrences and the potential toxicity impact associated with mining them. In this study, SMS samples from seven hydrothermal fields from various tectonic settings were investigated by in-situ microanalysis (electron microprobe (EMPA) and laser ablation inductively coupled plasma mass spectrometry (LA-ICP-MS)) to highlight the distribution of potentially-toxic trace elements (Cu, Zn, Pb, Mn, Cd, As, Sb, Co, Ni, Bi, Ag and Hg) within the deposits, their minerals and textures. We demonstrate that a combination of mineralogy, trace element composition and texture characterisation of SMS from various geotectonic settings, when considered along with our current knowledge of oxidation rates and galvanic coupling, can be used to predict potential toxicity of deposit types and individual samples and highlight which may be of environmental concern. Although we cannot quantify toxicity, we observe that arc-related sulfide deposits have a high potential toxicity when compared with deposits from other tectonic settings based on their genetic association of a wide range of potentially toxic metals (As, Sb, Pb, Hg, Ag and Bi) that are incorporated into more reactive sulfosalts, galena and Fe-rich sphalerite. Thus, deposits such as these require special care when considered as mining targets. In contrast, the exclusive concern of ultra-mafic deposits is Cu, present in abundant, albeit less reactive chalcopyrite, but largely barren of other metals such as As, Pb, Sb, Cd and Hg. Whilst geological setting does dictate metal endowment, ultimately mineralogy is the largest control of trace element distribution and subsequent potential toxicity. Deposits containing abundant pyrrhotite (high-temperature deposits) and Fe-rich sphalerite (ubiquitous to all SMS deposits) as well as deposits with abundant colloform textures also pose a higher risk. This type of study can be combined with "bulk lethal toxicity" assessments and used throughout the stages of a mining project to help guide prospecting and legislation, focus exploitation and minimise environmental impact.

Keywords: sulfide geochemistry; SMS; LA-ICP-MS; trace elements; seafloor mining; environment; toxicity; oxidation; leaching

1. Introduction

Heightened interest in seafloor mining in international waters is emphasised by the International Seabed Authority (ISA) issuing 29 exploration contracts as of end-2018. Of those 29, seven are contracts to explore for polymetallic sulfides, also known as seafloor massive sulfide (SMS) deposits. Whilst

more difficult to track, there are also an estimated 26 exploration projects within national jurisdiction areas of individual states' economic exclusion zones (EEZs) as well as 70 territories applying to extend their continental shelf and subsequent EEZ to lay claim to larger expanses of seafloor and associated mineral resources [1,2]. Highlighting specific interest in SMS deposits is Nautilus Minerals Inc., who are in the process of planning mineral extraction in what could be the world's first SMS mine at the Solwara 1 deposit in the national waters of Papua New Guinea.

SMS deposits at both active and inactive vents are currently being considered as exploration targets. The only published concept for SMS mining is provided by Nautilus Minerals Inc. which is expected to include both an "in situ" extraction phase, where the sulfide is cut on the seafloor, and a dewatering process, where the mineral slurry is carried to the surface, dewatered and the waste water (containing fine sulfide) is returned to 25–50 m above the seafloor [3]. During this process, fine sulfide particulates are created and may also undergo geochemical changes including partial dissolution and oxidation. If any leaching of metals produced during dissolution is not balanced by their precipitation (as oxide/oxy-hydroxide/chloride) or adsorption onto oxides, there is the potential for local accumulation of dissolved metals into the water column as shown in leaching experiments not only by the scientific community but also those taken as a regulatory need for environmental risk assessments [4–9]. All studies demonstrate a release of metals and highlight Cu, Zn, Pb and Cd as having the highest dissolved concentrations, which they largely attribute to galvanic coupling [4,5,9]. What these studies do not address, however, is the effect of bioleaching of sulfide minerals. It is widely accepted that redox reactions utilising Fe^{3+} produced by bacteria can catalyse dissolution rates of sulfide minerals [10–14] as well as accelerate galvanic coupling in a polymineralic ore in acidic conditions [15–20]. Whilst slower, there have also been studies reporting bioleaching of sulfide minerals at neutral pH conditions [21,22]. It has been postulated that colonization of freshly ground mineral surfaces is unlikely under the rapid time spans of mining (<30 min based on mining scenarios) [23,24]. However, bioleaching does have the potential to be a concern if mining occurs over months of operation as well as once any fine sulfide material has settled after initial extraction and dewatering [4].

Dissolution and release of metals can ultimately have a detrimental impact in terms of toxicity on not only local vent ecosystems (both active, inactive and weathering) [25–29], but also the surrounding deep or coastal ocean including background fauna (soft sediment benthos) and charismatic marine megafauna as a result of plume formation, dispersal through sediment porewaters and currents and/or unwanted spoil loss [30]. However, it is important to emphasise that toxicity of a given element is ultimately dependent upon chemical speciation and bioavailability of those species, rather than solely upon the concentration of metals released [31]. Chemical species in solid form (e.g., natural sulfide mineral, released metals precipitated as or adsorped onto secondary oxides/hydroxides) are considered less bioavailable and have lower potential to be toxic to benthic invertebrates [32]. Chemical species aqueously complexed with other elements can be more or less bioavailable and/or toxic, with less bioavailable aqueous complexes also capable of producing toxicity [32–34]. However, one study in particular suggests that sulfide complexation can ameliorate toxicity to some organisms [33]. In contrast, partially oxidized sulfide minerals which are expected to be produced during mining, will have a higher proportion of more soluble, weakly bound metalloids which are ultimately more bioavailable as well as produce a higher risk of toxicity [32].

No regulations or guidelines on metal toxicity limits currently exist for deep-sea vent ecosystems [35]; a result of our lack of understanding of these unique and complex ecosystems. Whilst it has been demonstrated that there can be a high tolerance of particular species adapted to live at active vents [33,36–40], this has not been fully constrained for fauna that is present at inactive vent sites or weathering sites due to exposure to oxygenated seawater. Furthermore, whether the tolerance of any vent species (either at active, inactive or weathering sites) is high enough to cope with concentrations released by mining is also unconstrained. Exposure tests to a range of dissolved metals (predominantly Cu) on a variety of deep-sea species (vent and background fauna) have been undertaken to assess the potential impact [33,36,41–44]. Different strains of bacteria and archaea from

active vent systems demonstrate no consistent tolerance levels across a range of metals with some highly sensitive to Cu, or Cd and Zn/Pb and resistant to Co and Ni and vice versa [33,36]. Edgcomb et al. (2004) [33] discuss the propensity of Zn and Cu to form stronger sulfide complexes than Co based on other studies [45,46], indicating Co could be more bioavailable. One study by Vetriani et al. (2005) demonstrates that vent bacteria at inactive sites are more sensitive to Hg in comparison to those that are adapted to active vents along the East Pacific Rise, indicating the higher potential toxicity at inactive sites during mining [37]. Experiments on macrofauna find that even active vent fauna are sensitive to Cu exposure, with damage to tissues observed (albeit inconsistent across all tissues within each organism) [41,42]. Auguste et al. (2016) [41] specifically noted lipid membrane damage in vent mussels collected from Lucky Strike at Cu concentrations >300 µg/L. Observations of behavioral avoidance by mobile organisms, specifically Cu, have been noted in numerous studies, indicating an immediate response to protect the organism from toxicity [47,48].

Despite these noteworthy studies, Hauton et. al (2017) [35] highlight the numerous difficulties of reliably determining toxicity to individual organisms. This most notably includes the fundamental differences in metal uptake from solution and toxic effects at non-standard laboratory conditions (e.g., in situ deep-sea low temperatures and high pressures) [44,49], with a natural mineral ore containing complex mixtures of metals with a range of oxidation states that can ultimately interact with one another as well as change with mineral weathering [50,51]. They propose that instead of applying any existing toxicological data established at standard lab conditions or attempting to identify lethal limits for single or simple combinations of metals, that the "bulk toxicity of each mineral deposit is assessed to identify a priori the potential risk" under controlled and ecologically relevant conditions for biological proxy organisms at a range of life cycle stages [35].

Studies undertaken on the disposal of mine tailings in coastal and deep ocean can also provide an indication of sulfide mineral oxidation in seawater and subsequent potential toxicity and impact [52–55] where significant accumulations of heavy metals (Zn, Pb, Cu and Cd) have been observed in sediment porewaters tens of years after tailings disposal [56–60]; in some cases this has translated to high dissolved Cu in local seawater (coastal Chile; [59,60]). Of particular interest is a study of submarine tailings deposition from a Pb-Zn mine in Greenland by Josefson et al. (2008) [56] that provided a threshold response of benthic macrofauna for Pb of 200 mg/kg. Moreover, in the context of accidental leakage and dispersion of sulfides during mining, the shallow marine environment also has the potential to be impacted and, based on a recent study by Fuchida et al. (2017) [5], has the strong potential to be toxic for marine phytoplankton with Pb, Cu and As highlighted as significant toxicants. This is in agreement with other studies, where phytoplankton in particular is very sensitive to As (3 µg/L), suggested to be a result of its range of oxidation states and subsequent bioavailability [61,62]. These studies highlight the necessity to evaluate mining impact and any associated potential toxicity for not only vent ecosystems (active, inactive and weathering), but also surrounding deep-ocean and shallow-marine ecosystems.

It needs to be emphasised in this respect that not all SMS occurrences are geochemically similar. These occurrences form in a range of tectonic settings including mature volcanic-hosted mid-ocean ridges and younger sediment-rich rifts (with varying rates of spreading), hot spots and arc-related settings [63]. The host rock lithology is dictated by the tectonic environment, with a range of host rock compositions occurring including predominantly mafic to ultramafic (basalt, gabbro and serpentinite) along mid-ocean ridges (MORs) and more evolved compositions (andesite, dacite and rhyolite) in arc settings as well as prominent pelagic and/or volcanoclastic sediments in near-coastal settings [63]. These volcanic and tectonic controls ultimately dictate the source and availability of major and minor elements for the seafloor massive sulfide ore deposits. SMS deposits and their economic potential has been discussed extensively in the literature, with Cu and Au driving most commercial interest, although presence of Zn, Pb and Ag could also be key [64–66]. Monecke et al. (2016) [66] document variation of SMS deposits with the most comprehensive database of bulk chemistry analyses to date. As a consequence, this also provides some knowledge of metal concentrations of SMS deposits

that could potentially be toxic to marine fauna. Combined Cu + Zn + Pb contents were compared across a range of tectonic environments to highlight economic worth where sediment covered ridges (1.5 wt %) < basalt-hosted ridges (3.2 wt %) < arc volcanoes (3.6 wt %) < rifted arc crusts (11.1 wt %) < ultramafic-hosted (13.2 wt %), with back arc spreading centres demonstrating the highest content (16.1 wt %). Common trends in the bulk chemistry of minor elements of SMS deposits from different settings are also observed. Mafic to ultramafic host rock dominated MORs consistently demonstrate high concentrations of Cu, Fe, Co, Se, Ni, Mo and Te. In comparison, volcanic arcs and young back arc rifts where more evolved volcanic host rocks are dominant show high concentrations of Zn, Cd, Pb, As, Sb, Hg, Ba, Tl and Au [63,66,67]. An extreme example of the enrichment of potentially toxic elements is the shallow-water (200 m) Calypso vent field north of New Zealand that is characterized by abundant native mercury and Hg-sulfides [68]. The trace element enrichment at this site might even influence the faunal communities in the photic zone. Knowledge about the enrichments of potentially toxic elements is therefore crucial in determining boundary conditions for environmental baseline studies and monitoring during exploration and mining. Based on studies, high bulk contents of Cu, Pb, As, Cd, Sb and Hg are largely associated with arc related settings. However, the high concentrations of major heavy metals (Cu, Zn, Pb) from ultramafic-hosted ridges also suggest that they have the potential to cause toxicity during any future mining. Temperature also plays a large role, with higher temperature Cu-rich chimneys ~350 °C), being associated with high concentrations of Co, Se and Mo. Lower temperature fluids (<250 °C) show an association with Cd, Pb, As, Sb and Ag [66,67].

However, in order to constrain the potential toxicity of SMS deposits, it is important to study not only the bulk chemistry but also the mineralogy and trace element distribution. Understanding the trace content of sulfides is imperative to understanding their subsequent dissolution, where particular impurities are known to increase the oxidation rate of specific minerals [69–74]. Characteristics of a deposit that affect its oxidation and dissolution potential can be helpful tools in predicting leaching and associated potential toxicity, and ultimately allow comparisons of potential environmental impact [75]. This can permit development of strategies for dealing with mine waste and remediation. Of course, a corollary to this is that the same information feeds into an appreciation of economic worth and recovery of economically important (toxic or not) elements.

A compilation of available trace element data in sulfide minerals (derived from EMPA and LA-ICP-MS) from SMS samples collected worldwide is discussed in Fallon et al. (2017) [76] and provides a basis for assessment of potential toxicity and highlighted the gaps in our knowledge. LA-ICP-MS in particular has been highlighted in the literature as an ideal tool to investigate the distribution and zonation of trace elements in sulfide minerals, due to its lower detection limits in comparison to EMPA and its ability to investigate the nature of trace element incorporation (e.g., homogeneous distribution versus presence of micro-inclusions; [77–80]. Major base metal concentrations in sulfide deposits are primarily controlled by the abundance of pyrite/marcasite/pyrrhotite for Fe, chalcopyrite/isocubanite/bornite/covellite/digenite/chalcocite for Cu and sphalerite/wurtzite for Zn. In contrast to Cu and Zn, Fe is generally expected to pose less potential toxicity as a result of its ease of oxidation and subsequent precipitation due to the low solubility of Fe(III). Where Pb is present in sufficiently high concentrations within deposits, it is controlled by the presence of galena or Pb-bearing sulfosalts [66]. Arsenic and Sb concentrations tend to be high in samples from arc-related settings, and where present in high enough concentrations, are controlled by tennantite-tetrahedrite solid solution minerals [66]. The presence of large amounts of tennantite-tetrahedrite also has the potential to control the abundance of Cu.

In this study, 11 different sulfide minerals were characterised by in situ microanalysis (EMPA and LA-ICP-MS spot analyses) for 23 samples representing a wide range of black smoker vent environments. This study combines the observations of mineralogy and texture of a range of SMS deposits with analytical results on the trace element distributions to allow us to highlight SMS deposits or individual mineral phases/textures that may have a greater potential toxicity on the surrounding environments during any future deep-sea mining ventures.

2. Materials

Location and details of the 7 hydrothermal fields and their respective geological settings studied are presented in Figure 1 and Table 1. Three of the sample sites are located along the Mid-Atlantic Ridge (Trans-Atlantic Geotraverse (TAG), Logatchev and Turtle Pits). TAG is one of the most extensively studied and is unique in that it is a mature deposit showing distinct zonation due to extensive hydrothermal reworking and recrystallization [81]. Turtle Pits varies from other MAR hydrothermal fields because of the extraordinary high vent fluid exit temperatures (±407 °C) that were recorded here [82] whereas Logatchev is distinct due to its ultramafic host rock composition [83].
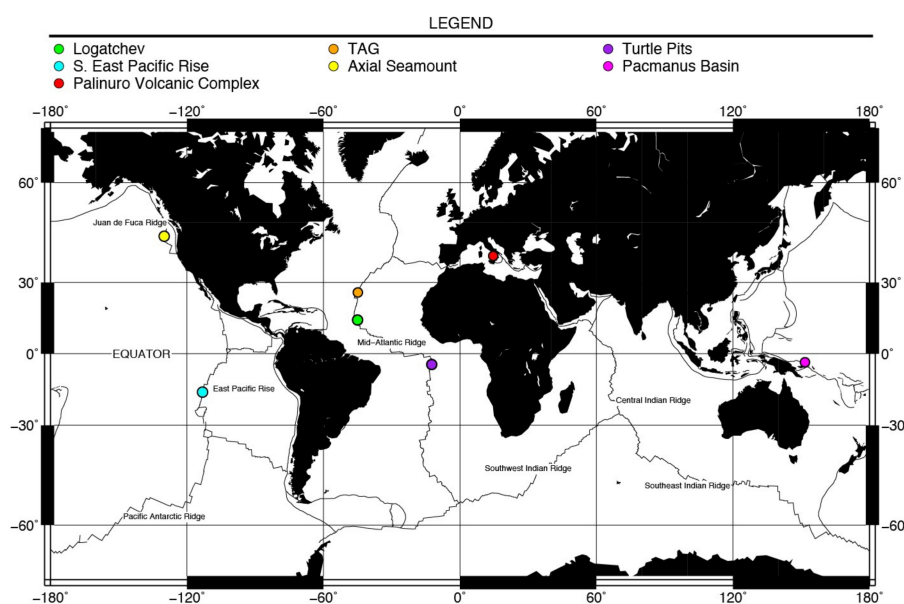
Figure 1. Coloured circles represent the global distribution of the hydrothermal fields and seafloor samples investigated in this study including ASHES, located at Axial Volcano on the Juan de Fuca Ridge, 16°43′S hydrothermal field along the South East Pacific Rise, active Trans-Atlantic Geotraverse (TAG) mound, Logatchev-1, Turtle Pits, Pacmanus and Palinuro Volcanic Complex (PVC).

Other samples include those from the ASHES (Axial Seamount Hydrothermal Emissions Studies) vent field located within the hotspot associated caldera of Axial Volcano on the Juan de Fuca Ridge and those from a young vent field at 16°43′S at the ultra-fast spreading ridge of the East Pacific Rise. In contrast, the Pacmanus and Palinuro hydrothermal fields are part of wide range of deposits associated with subduction zones. Pacmanus is felsic-hosted (dacite to rhyolite) rather than the more usual mafic-hosted setting typical of mid-ocean ridges. Palinuro (Tyrrhenian Sea) is different to other hydrothermal fields studied here, as it is located within an active volcanic arc. Sulfides at Palinuro are buried beneath a thin layer of sediment, and are suggested to have formed largely by sub-seafloor replacement and infiltration [84]. As a result, chimney structures that are typical for most SMS are not observed. Both Pacmanus (Satanic Mills area) and Palinuro are distinct from other hydrothermal fields because magmatic volatiles (CO_2, SO_2) from a degassing magma chamber at depth may contribute to the enrichment in magmatophile and trace elements including As, Sb, Bi and Te [84–86]. In addition to those metals, samples from Palinuro also display anomalously high concentrations of Hg [84].

Table 1. Location and features of the hydrothermal fields and their geological settings of the samples analysed in this study.

Hydrothermal Field	Location	Depth (m)	Tectonic Setting	Spreading Rate (mm/yr)	Host Rock	Characteristics	Max Recorded T of Fluids (°C)	No. Samples
Trans-Atlantic Geotraverse (TAG)	Mid-Atlantic Ridge (26°08′N, 44°49′W)	3650	Mature, sediment starved spreading ridge	Slow (23)	Basalt	5 × 5 km hydrothermal field Mature active mound (200 m diameter) with Cu-rich deep core and Zn-rich outer margins Black Smoker Complex includes cluster of cp-anh rich active chimneys	363	11
Turtle Pits	Mid-Atlantic Ridge (4°48′S)	2990	Mature, sediment starved spreading ridge	Slow (31)	Basalt	Very active volcanism Two major sulfide talus mounds with active and inactive chimneys superimposed	407	2
Logatchev-1	Mid-Atlantic Ridge (14°45′N, 44°58′W)	3000	Mature, sediment starved spreading ridge	Slow (24)	Ultra-mafic complex of peridotite, gabbronorite, minor basalt	"Smoking crater" vent morphologies Unusually rich in Cu and Au Zn rich restricted to northern field (not sampled here)	370 [87]	2
ASHES	Axial Volcano, Juan de Fuca Ridge (45°56′N, 130°00′E)	1530	Spreading ridge and hot spot (Cobb-Eikelberg)	Intermediate (51)	Basalt	Located within the caldera 200 × 1200 m hydrothermal field	348 [87]	1
16°43′S	East Pacific Rise (South) (16°43′S, 113°04W)	2745	Young spreading ridge	Ultrafast (141)	Basalt	Clusters of active chimneys and inactive massive sulfides and hydrothermal mounds	N/A High T (>300) based on microscopic observations	1

Table 1. *Cont.*

Hydrothermal Field	Location	Depth (m)	Tectonic Setting	Spreading Rate (mm/yr)	Host Rock	Characteristics	Max Recorded T of Fluids (°C)	No. Samples
Pacmanus	Manus Basin, Pual Ridge, Papua New Guinea (03°43′S, 151°40′W)	1650–1800	Arc/Back-arc basin (rifted arc)	Ultrafast (140)	Dacite/Rhyolite	>20,000 m^2 hydrothermal area Distinct areas of venting: SW–S (Satanic Mills—SM, Solwara-8—S-8) and NE (Roman Ruins—RR) cluster SM S-8 RR: Largest field in the area with mounds, chimneys (mostly inactive, some active up to 7 m) and lower T diffuse chimneys. Two mineral assemblages: py-sp and cp-sp with minor barite SM: Central cluster of branched thin chimney structures (up to 10 m high, 20 cm diameter). Cp-rich mineralogy, minor sp. Vent fluids display enrichments of CO_2, SO_4, H_2S and F, with associated presence of magmatophile trace elements all linked to presence of an exsolved magmatic fluid component S-8: Clusters of chimneys up to 12 m both Cu and Zn rich	SM: 345 S-8: 305 RR: 341	4
Palinuro	Palinuro Volcanic Complex, Marsili Basin, Tyrrhenian Sea, Italy	600–630	Arc/Back-arc basin (active volcanic arc)		Basalt/Andesite	Due to close proximity to an eroding landmass, the deposit is buried beneath tens of centimeters to metres of sediment with no classic chimney structures observed. Formed by sub-seafloor replacement, infiltration and microbial processes. Consists of metal-enriched upper vuggy-barite-sulfide zone and barren lower zone. Samples enriched with precious metals (Au, Ag) and anomalously high epithermal elements (As, Hg, Bi and Sb) linked to the presence of an exsolved magmatic fluid component with high volatiles (CO_2 and SO_2)	58 (in diffuse fluids of waning stage)	2

3. Methods

In order to produce a comprehensive study, samples were selected from a range of tectonic settings, host rocks, active/inactive vents and vent exit temperatures. A mixture of one-inch polished mounts and/or thin sections were prepared for each sample. A combination of reflected light optical microscopy and scanning electron microscopy (SEM) in back scattered electron (BSE) mode were used to characterise the sulfide mineralogy of each sample. Specific attention was given to any heterogeneity within the sulfide minerals, mineral inclusions, compositional zoning and texture. Quantitative analysis of the sulfide minerals present in each sample was undertaken using an electron microprobe (EMPA) for major element composition and laser ablation inductively coupled plasma mass spectrometry (LA-ICP-MS) for trace element analysis. Each whole rock sample (hand-sized, up to 10 cm) was crushed and dry sieved to various grain size distributions. An aliquot of the <50 μm size fraction (~2 g) was used for X-ray diffraction to determine modal mineral abundances.

3.1. Electron Microprobe Analysis

All sulfide minerals were analysed using a Cameca SX100 Electron Probe Micro Analyser at the School of Earth Sciences, University of Bristol, UK. Analyses were conducted using an accelerating voltage of 25 kV, with beam currents between 50 and 200 nA and a spot size of either 1 or 5 μm (dependent on grain size). Natural pyrite and galena were used for standardisation of Fe, S and Pb. Synthetic HgTe and GaAs were used for standardisation of Hg and As respectively, while all other elements (Cu, Zn, Mn, Co and Sb) were standardised on metals. Calibration was performed with a beam current of 10 nA with the exception of Pb on galena (150 nA to avoid high dead time). Background count times were always half of the peak count time. Analyses of standards as unknown were undertaken to ensure the quality of the produced data. Where no or limited LA-ICP-MS was obtained, EMPA data for Fe, Cu, Zn, Mn, Co, Pb, As and Sb are used (in the case of all Palinuro samples and for sulfide minerals with small grain sizes, e.g., pyrrhotite). Analysis of Hg was undertaken separately, with wave scans performed over each sulfide mineral to identify potential interferences with the Hg peak and create mineral-specific set up parameters. Detailed set up parameters including beam currents, spot sizes, peak count times, background positions and detection limits for each element are quoted in Table S1 in Supplementary Materials.

3.2. Laser Ablation Inductively Coupled Mass Spectrometry

Trace elements were analysed by LA-ICP-MS using a 193 nm Excimer laser ablation system (Coherent, GeoLasPro) coupled to a double-focusing, high-resolution magnetic sector mass spectrometer (Nu Instruments, AttoM) at GEOMAR, Helmholtz Centre for Ocean Research, Kiel. Ablation was carried out under He carrier gas. Argon transport gas was added after the ablation cell. Gas flows, torch position and ion-optics-focusing were optimized in order to provide a maximum in ion transmission, low polyatomic cluster production rate (ThO/Th $\leq$ 0.03%; CuAr/Cu $\leq$ 0.003%) by hot plasma (normalized argon index NAI > 30; [88]) and fast sample wash-out.

Spot analyses on sulfide minerals (in pre-defined areas of the thin sections and polished blocks) were accomplished by 30 s ablation at a laser repetition rate of 5 Hz using spot diameters between 16 and 44 μm and a fluence of 2 J·cm^{-2}. Prior to each ablation 50 s gas background were collected. The spot size was modified as a function of phase size, homogeneity and thickness of the sample. The pulse rate per spot was modified as a function of grain size and subsequent spot size. Where phases were small or irregularly shaped, 2 or 3 spots of smaller size (16 μm) in the same region were combined and used to ablate enough material continuously during the 30 s ablation interval. A suite of 66 isotopes were monitored for quantitative analysis including: ^{34}S, ^{55}Mn, ^{57}Fe, ^{59}Co, ^{60}Ni, ^{63}Cu, ^{66}Zn, ^{75}As, ^{107}Ag, ^{111}Cd, ^{118}Sn, ^{121}Sb, ^{202}Hg (Palinuro samples only), ^{208}Pb and ^{209}Bi. These elements are the focus of this contribution as they are considered to have a tendency to form toxic species at

high concentrations or impact oxidation rate in the marine ecosystem [89] as well as hydrothermal vent systems as discussed earlier [33–38,90–94].

Quantification was performed using NISTSRM610 (30 s, 32 μm, 10 Hz, 5 J·cm^{-2}) as external standard. Two synthetic sulfide standards (PGE_Ni7b and trans1; 30 s, 44 μm, 5 Hz, 2 J·cm^{-2}) [95] were additionally used as external references for sulfur calibration. MPI-DING glasses (ATHO-G, T1-G, GOR132-G and KL2-G; 30 s, 32–44 μm, 10 Hz and 5 J·cm^{-2}) [96] were used as reference materials. The external standards were applied to all sample spots by analysing all at the start, middle and end of each analytical run. Comparisons of measured concentrations of the same elements obtained from different external standards gives excellent correlations of Fe, Cu, Zn, Ni, Co Mn and Pb concentrations, with precision shown in Table 2 (detailed comparison presented in Table S2). As MPI-DING glasses are not representative reference materials for high concentrations (>100 ppm) of As, Ag, Cd, Sn, Sb and Bi (see Table S2) due to their sub-ppm contents of these elements, later investigations under comparable analytical conditions on SRM MASS-1 were undertaken and demonstrate the confidence in our precision (Table 2). EMPA and LA-ICP-MS results of higher concentrated samples (Cd, Sb, Sn) are also compared as a further check on the validity of results and show mean concentrations are within the standard deviation of the mean of respective LA-ICP-MS measurements (Figure S1, Table S3). Quantification of Hg for Palinuro samples was only possible using one information value for MASS-1 standard reference material as it is not present in the NISTSRM610 external standard. However, this value has been used in several publications [97,98] and Hg was also quantified during EMPA analysis to provide validity on the LA-ICP-MS results.

Table 2. Precision of Mn, Fe, Co, Ni, Cu, Pb and Zn based on measurements of DING glasses (GOR132-G, KL2-G, StHs6-80-G, T1-G). Precision of Ag, Ag, Cd, Sn, Sb and Bi based on later investigations on SRM MASS1 (containing > sub ppm concentrations) under comparable analytical conditions.

	Mn	Fe	Co	Ni	Cu	Zn	Pb	As	Ag	Cd	Sn	Sb	Bi
Precision (RSD)	2.3	2.8	3.4	13.9	4.8	7.2	9.0	5.6	4.6	8.1	4.3	4.8	4.7
N	279	277	278	274	271	271	272	143	157	157	157	156	157

EMPA analysis of sulfide minerals provided an internal standard for the LA-ICP-MS data. Iron was used for pyrite/marcasite, Cu for chalcopyrite/bornite/tennantite-tetrahedrite, Zn for sphalerite/wurtzite and Pb for galena. Where EMPA data was unavailable or unsuitable (in the case of mixed, intergrown and solid solution phases) quantification was undertaken without use of an internal standard by scaling up the sum of the main components to 100 wt %.

Minimum detection limits (99% confidence) for LA-ICP-MS data were calculated for each element analysed during a spot analysis. Average detection limits for each element in each mineral phase were calculated and are presented in all figures with detection limits of a selection of elements displayed in Table 3. Detection limits for each element within sulfosalts were not calculated but assumed to be similar to those of galena, and these are presented in figures.

As a result of the potential large range of trace element distribution even within one sample, spot analyses were undertaken across the whole sample rather than focused within one area of a sample. Furthermore, where possible, spot analyses were undertaken on both chips and thin sections to ensure the data is representative of the sample as a whole.

Table 3. LA-ICP-MS average detection limits (ppm) for selected elements (Fe, Cu, Zn, As, Pb, Sb, Cd, Co, Ni and Mn) in each mineral phase.

Mineral	Average Detection Limits (ppm)									
	As	Cd	Co	Cu	Fe	Mn	Ni	Pb	Sb	Zn
Pyrite (N = 63)										
	0.24	0.19	0.05	0.29	5.44	0.05	2.43	0.02	0.03	0.28
Marcasite (N = 36)										
	0.39	0.26	0.08	0.33	7.41	0.08	3.60	0.02	0.04	0.49
Pyrrhotite (N = 4)										
	394	1.34	0.23	77.6	38.6	0.45	9.63	0.11	0.24	194
Chalcopyrite (N = 53)										
	0.78	0.49	0.11	1.99	13.6	0.10	3.34	0.11	0.06	0.68
Isocubanite (N = 5)										
	2.13	0.21	0.08	0.90	11.9	0.23	3.85	0.03	0.05	1.05
Bornite (N = 14)										
	1.02	0.28	0.09	1.19	12.9	0.15	3.25	0.02	0.12	0.75
Covellite (N = 17)										
	0.38	0.18	0.06	0.66	7.55	0.08	2.00	0.02	0.04	0.45
Sphalerite (N = 58)										
	0.35	0.27	0.06	0.97	8.62	0.09	7.35	0.06	0.05	0.72
Galena (N = 7)										
	0.36	0.17	0.05	0.47	5.04	0.07	0.90	0.14	0.04	0.64

3.3. X-Ray Diffraction

All cleaned sulfide ore powders (<50 μm) were analysed using a Phillips X'Pert Pro diffractometer with a Cu Kα source at the School of Physics, University of Bristol, UK. XRD parameters used during analysis of powders are presented in Table S4. XRD data were subsequently processed with use of Match! Phase identification for powder diffraction software (Version 2.4.7, Crystal Impact, Bonn, Germany) using the COD-Inorg REV189751 reference database. This provided an overall representation of the phases present including semi-quantitative analysis.

4. Sample Descriptions

A total of 23 samples of seafloor massive sulfide, collected from black smoker chimneys across 7 hydrothermal vent systems, were investigated for elements that have the potential to form toxic species (Table 4). Samples were obtained through rock drilling (RD), video-assisted grab (GTV) and remotely operated vehicles (ROV).

Table 4. Sulfide samples used throughout this study, quoted with their semi quantitative mineral abundances calculated from powder X-ray diffraction (XRD) data where available. Where not available, mineral abundances have been estimated through reflected light microscopy and SEM analysis. Abbreviations used in this table are tr (trace), py (pyrite), mc (marcasite), pyr (pyrrhotite), cp (chalcopyrite), is (isocubanite), sp (sphalerite), cc-cv (chalcocite-covellite), bn (bornite), td (tennantite-tetrahedrite), gn (galena), ba (barite), atc (atacamite) and anh (anhydrite). "Others" include quartz, silicates, carbonate, jarosite, native sulfur and Fe oxide/oxyhydroxides.

Hydrothermal Field, Location	Sample	Type	Cruise	Ref	Brief Description	Assemblage	Mineral Abundances (%)													
							Py	Mc	Pyr	Cp	Iss	Sp	Cc-Cv	Bn	Td	Gn	Ba	Atc	Anh	Others
TAG-4, MAR	TAG-H *158/957/M/2/R/1/W/12-14cm*	RD	IODP Leg 158 (1994)	[99]	Active mound: Massive sulfide crust	Intermediate to low	38	44				1							1.0	15
TAG-4, MAR	TAG-I *158/957/K/1/X/1/W/3-4cm*	RD	IODP Leg 158 (1994)	[99]	Active mound: Upper mound—porous colloform py, mc	Intermediate to low	51	38				1							1	10
TAG-4, MAR	TAG-J *158/957/K/2/N/1/W/10-12cm*	RD	IODP Leg 158 (1994)	[99]	Active mound: Massive sulfide crust	Intermediate to low	84	6		5		1	1						1	3
TAG-5, MAR	TAG-K *158/957/P/1/R/1/W/79cm*	RD	IODP Leg 158 (1994)	[99]	Active mound: Semi massive pyrite-anhydrite	Intermediate to high	11			4									86 *	
TAG-5, MAR	TAG-L * *158/957/P/1/R/1/W/50-52 cm*	RD	IODP Leg 158 (1994)	[99]	Active mound: Semi massive pyrite-anhydrite breccias with cp	Intermediate to high	30			5									65	
TAG-1, MAR	TAG-M * *158/957/E/1/R/1/W/1-3 cm*	RD	IODP Leg 158 (1994)	[99]	Active mound: Semi massive pyrite-anhydrite breccias with cp	Intermediate to high	45			10									45	
TAG-4, MAR	TAG-46 *158/957/K/2/N/1/9*	RD	IODP Leg 158 (1994)	[99]	Active mound: Massive sulfide crust	Intermediate to low	56	37		5										3
TAG-4, MAR	TAG-47 *158/957/K/3/X/1/6*	RD	IODP Leg 158 (1994)	[99]	Active mound: Massive sulfide crust	Intermediate to low	62	33				1								4
TAG-4, MAR	TAG-48 *158/957/K/3/X/1/7*	RD	IODP Leg 158 (1994)	[99]	Active mound: Massive sulfide crust with porous colloform py, mc	Intermediate to low	48	38				3								11

Table 4. *Cont.*

Hydrothermal Field, Location	Sample	Type	Cruise	Ref	Brief Description	Assemblage	Mineral Abundances (%)													
							Py	Mc	Pyr	Cp	Iss	Sp	Cc-Cv	Bn	Td	Gn	Ba	Atc	Anh	Others
TAG-1, MAR	TAG-6F *158/957/C/7/N/1/6F*	RD	IODP Leg 158 (1994)	[99]	Active mound: Massive pyrite breccias with abundant cp	Intermediate to high	65			10									15	10
TAG-1, MAR	TAG-27 *158/957/C/7/N/1/6G*	RD	IODP Leg 158 (1994)	[99]	Active mound: Massive pyrite breccias with abundant cp	Intermediate to high	41			24	13								7	16
Turtle Pits Mound, MAR	TP2L *124-GTV-2L*	GTV	Meteor M64/1 (2005)	[100]	Outer part of massive inactive chimney	Low to intermediate	73	13		6							3		1 *	3
Southern Tower, Turtle Pits, MAR	TP4B *114-ROV-4B*	ROV	Meteor M64/1 (2005)	[100]	Cu-rich, interior of active chimney	High	51	24	2	6	12	4								2
Candelaber, Logatchev, MAR	LOG11 *64-ROV-11*	ROV	Meteor M60/3 (2004)	[101]	Cu-rich inactive chimney	High (some areas of oxidation)				81	11	3		3						
Irina-1, Logatchev, MAR	LOG13 *53-ROV-13*	ROV	Meteor M60/3 (2004)	[101]	Multilayered active Cu rich chimney (talus)	High				82		1						10	8	
ASHES vent field, JDFR	AS1 *SO109-89-GTV/4*	GTV	Sonne SO109 (1996)	[102]	Inactive Cu-rich chimney	High	19	7		44		29						1		1
16°43′S hydrothermal field, EPR	SEPR *SO62-310GTV*	GTV	Sonne SO62 (1991)	[103]	Inactive chimney	Intermediate to high	32	6		41		10		4						7
Roman Ruins, Pacmanus field, Manus Basin, PNG	PM2D *70-GTV-2D*	GTV	Sonne SO166 (2002)	[104]	Inactive chimney, porous massive sphalerite cementing dacite-sulfide breccia	Low	12	4		1		13				4	25			41
Satanic Mills, Pacmanus field, Manus Basin, PG	PM5E *58-GTV-5E*	GTV	Sonne SO166 (2002)	[104]	Active black smoker, in dacite matrix	High	5	tr †		35		22			5 ‡	1	27			5

Table 4. *Cont.*

| Hydrothermal Field, Location	Sample	Type	Cruise	Ref	Brief Description	Assemblage	Mineral Abundances (%)													
							Py	Mc	Pyr	Cp	Iss	Sp	Cc-Cv	Bn	Td	Gn	Ba	Atc	Anh	Others
Satanic Mills, Pacmanus field, Manus Basin, PNG	PM6B *58-GTV-6B*	GTV	Sonne SO166 (2002)	[104]	Active black smoker, porous sphalerite plus chalcopyrite	Intermediate	10	tr †		3		40			4 ‡	2	41			1
Solwara 8, Pacmanus field, Manus Basin, PNG	PM2F *33-GTV-02F*	GTV	Sonne SO216 (2011)	[105]	Talus, Secondary Cu-sulfides	High (some areas of oxidation)				28		6	3	12	4	tr †	32	15		1
Palinuro Volcanic Complex, Aeolian Island Arc, Italy	851-RD * *851-RD-011-015*	RD	M73/2 (2007)	[106]	Subseafloor SMS Vuggy-barite zone (Low T assemblage)	Intermediate to low	10					30			5 §	25	45			5
Palinuro Volcanic Complex, Aeolian Island Arc, Italy	932-RD * *932-RD-066-070*	RD	M73/2 (2007)	[106]	Subseafloor SMS Vuggy-barite zone (High T assemblage)	Intermediate to low	25			5					5	10	45			10

* Mix of anhydrite and gypsum, † Mineral abundance estimated through reflected light microscopy and SEM analysis, ‡ Includes enargite, § Includes Pb sulfosalts (jordanite).

Black smoker chimneys are generally zoned [77,78]; these often take the form of a high temperature inner zone assemblage comprising chalcopyrite, isocubanite and/or pyrrhotite, an intermediate temperature zone of pyrite and sphalerite and/or overgrown by chalcopyrite and an outer lower temperature zone including predominantly anhydrite with accessory pyrite overlain by marcasite crusts. In waning and/or oxidising stages, chalcopyrite is replaced to create an assemblage of secondary Cu sulfides including bornite, covellite, digenite and chalcocite, with the occasional presence of atacamite (a copper chloride) formed by these secondary processes (e.g., waning stages of hydrothermal fluid flow at lower temperatures or seafloor weathering at ambient temperatures). Each sample used in this study has been categorised into either high, intermediate or low based on mineralogical observations (Table 4). Samples include those of high temperature mineral assemblages (Logatchev: LOG11, Axial Seamount, Pacmanus: PM5E & PM2F, Turtle Pits: TP4B), intermediate (Southern East Pacific Rise, Pacmanus: PM6B) and low (Turtle Pits: TP2L, Pacmanus: PM2D).

It is important to note that not all samples are a perfect fit to each "zone" in terms of chimney growth. Samples from TAG are particularly difficult to categorise where the majority of samples (TAG-1, TAG-4 and TAG-5) do not take the characteristic chimney structure. Instead, TAG samples are representative of the mature end member of a SMS deposit where individual black smoker chimneys have been reworked (coalescence and accumulation of talus from chimneys) over time into a large active SMS mound [107]. However, the active mound is zoned overall, with a Cu-rich (higher temperature) deeper core and Zn-rich (lower temperature) outer margins, allowing for mineralogical classification. Similarly, whilst samples from Palinuro do not show the characteristic chimney formation due to their sub seafloor formation, they can still be classified by their mineralogical assemblage (which is a function of temperature). TAG samples (N = 11) are generally dominated by pyrite and range from intermediate to low and intermediate to high temperature mineral assemblages. Palinuro samples (N = 2) are representative of intermediate to low temperature assemblages, made up of considerable pyrite, barite, galena $\pm$ sphalerite. For further detailed descriptions, please refer to Appendix A.

In this study, three mineral textures are distinguished in the samples investigated, related to various stages of crystallisation. The earliest formed and prograde (or immature) texture identified is zoned colloform, which is highlighted in Figure 2B (sphalerite). An intermediate stage of recrystallisation can be identified by a porous texture (Figure 2A, pyrite (bottom left)) where the porosity of sulfides is reduced during recrystallisation of primary precipitates to fully massive sulfides [108]. A final or mature stage of recrystallisation is represented by massive textures that display interlocking subhedral to euhedral textures (seen in Figure 2A,C,D, pyrite/marcasite, chalcopyrite and chalcopyrite respectively.)

Modal abundances of minerals within most samples were determined using semi-quantitative powder XRD and are included in Table 4. Where XRD data is not available, mineral abundances have been estimated through reflected light microscopy and SEM analysis. Descriptions of the samples used in this study are given in Appendix A based on observations using a combination of reflected light microscopy in both plane-polarised (PP) and cross-polarised light (XP), scanning electron microscopy (SEM), electron microprobe analysis (EMPA) and powder XRD.
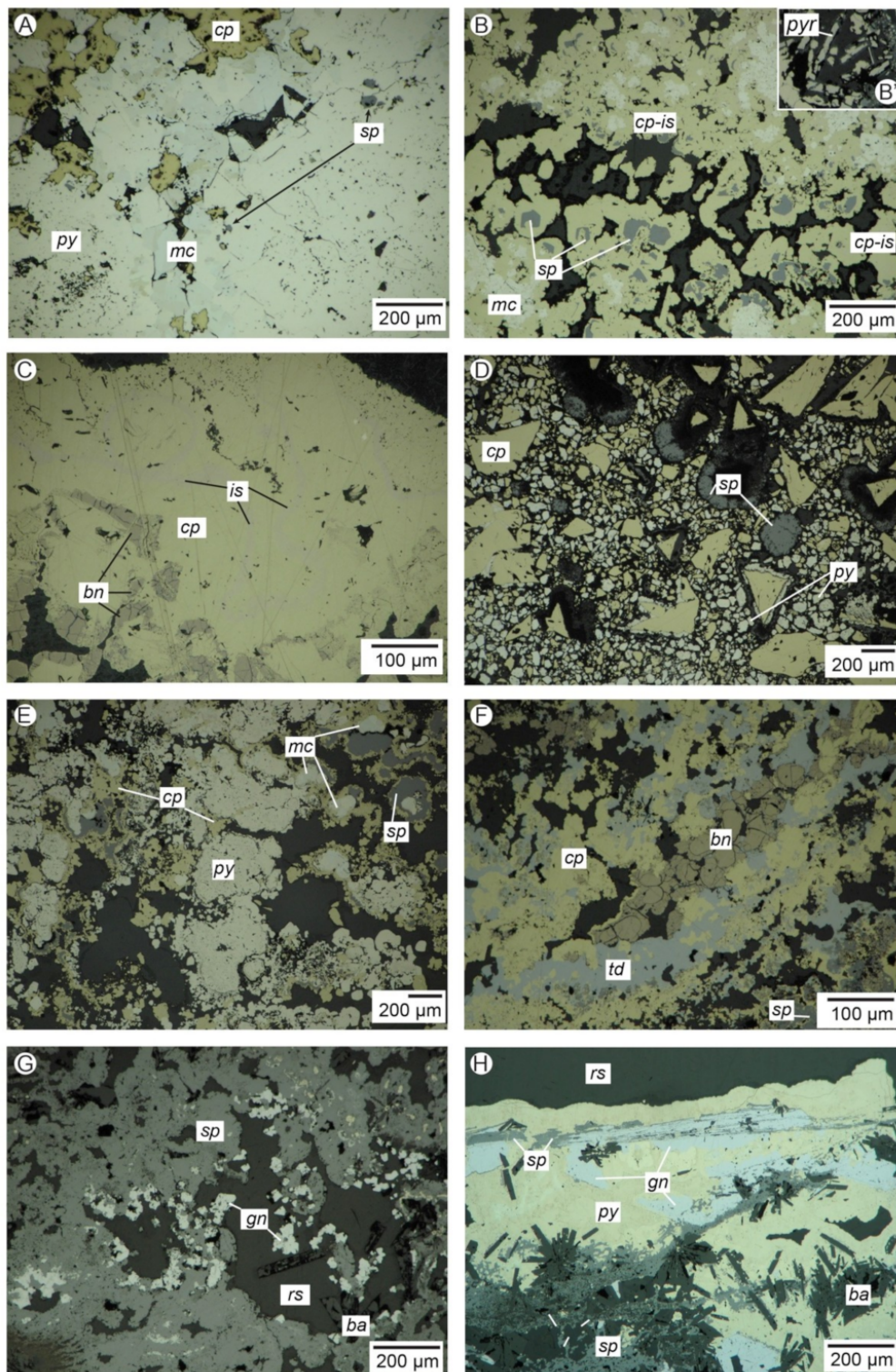
Figure 2. Reflected light photographs highlighting the range of seafloor sulfide minerals and common textures observed and analysed throughout this study. (**A**) Massive and porous textures of pyrite (py; porous—bottom left), euhedral marcasite (mc) with massive chalcopyrite (cp) and sphalerite (sp) inclusions from TAG, MAR (TAG-46); (**B**) Active sample from Turtle Pits, MAR (TP4B) showing early marcasite overgrown by chalcopyrite-isocubanite (cp-is) and sphalerite with colloform textures, (**B′**) Pyrrhotite (pyr) laths; (**C**) Active chimney talus from Logatchev, MAR (LOG-11) demonstrating patchy distribution of elongated isocubanite (is) exsolved within massive chalcopyrite and bornite (bn) forming along fractures and around grain boundaries of chalcopyrite; (**D**) Sample taken from an inactive chimney at the 16°43′S hydrothermal field along the East Pacific Rise (SEPR) showing sandy

sulfide particles consisting of grains of pyrite, chalcopyrite and marcasite infilling a large fracture of the chimney. The small sized fraction forms the matrix around larger euhedral chalcopyrite and colloform sphalerite; (**E**) Active chimney sample from ASHES vent field along the Juan de Fuca Ridge demonstrating colloform marcasite, sphalerite, chalcopyrite and pyrite; (**F**) Talus of an active chimney from the Solwara-8 area at Pacmanus hydrothermal field, Papua New Guinea. Sample shows anhedral secondary copper sulfides of bornite, chalcocite and covellite as well as tetrahedrite (td); (**G**) Sample PM6B from an active chimney within the Satanic Mills area at Pacmanus showing colloform sphalerite with massive galena (gn) and barite (ba) as well as resin (rs); (**H**) Subseafloor sulfide sample 932-RD taken from Palinuro Volcanic Complex within the Aeolian Island Arc in Italy, containing colloform pyrite, sphalerite and massive galena forming around barite crystals.

5. Results

Mean EMPA concentration data of major elements (S, Fe, Cu, Zn and Pb) and standard deviation (SD) for each mineral per individual thin section/mount (ppm) is presented in Table S5 in Supplementary Materials. The LA-ICP-MS data set (625 spot analyses) is reported in Supplementary materials (Table S6) and includes Ag, As, Bi, Cd, Co, Mn, Ni, Pb, Sb, Cu, Zn and Fe; as well as Hg for Palinuro sulfide minerals. For a few samples, trace element analyses rely on EMPA data due to lack of calibration standard, small grain size or intergrowths unsuitable for the laser ablation method. This includes As, Co, Cu and Zn for pyrrhotite from Turtle Pits (TP4B sample), As, Sb, Zn, Cu and Mn for colloform pyrite and chalcopyrite from Pacmanus (PM5E and PM6B) and Hg data for minerals from Palinuro (177 data points, mean concentrations and SD reported in Table S7). Only a few LA-ICP-MS analyses were gathered for these samples (3 for TP4B pyrrhotite and 4 for Pacmanus colloform pyrite).

All Hg EMPA data for sulfide minerals (pyrite, chalcopyrite, tennantite-tetrahedrite, sphalerite and galena) within the sample suite were below the detection limit for Hg (Table S1) with the exception of all Palinuro samples. Mercury EMPA data for Palinuro pyrite, sphalerite, tennantite-tetrahedrite and galena is reported in Table S7.

As highlighted by Wohlgemuth-Ueberwasser et al. (2015) [77], trace element contents in sulfide minerals are controlled by a range of variables including mineral type, mineral texture, zonation and the presence of micro-inclusions within the mineral. For each individual spot, LA-ICP-MS spectra were investigated for any strong shifts in signal intensity of certain major elements (Si, Fe, Cu, Zn, As, Sb and Pb) (Figure 3). Such strong shifts in intensity within the LA-ICP-MS spectra were assumed to be mineral inclusions and removed where possible by deleting the corresponding signal cycles; if not possible the data point was removed from the dataset entirely. Precision of trace element analysis is inherently difficult to assess when minerals are often heterogeneous and trace elements are not consistently above detection limits. However, based on external references, trace element concentrations have a precision <10% (Table 2).
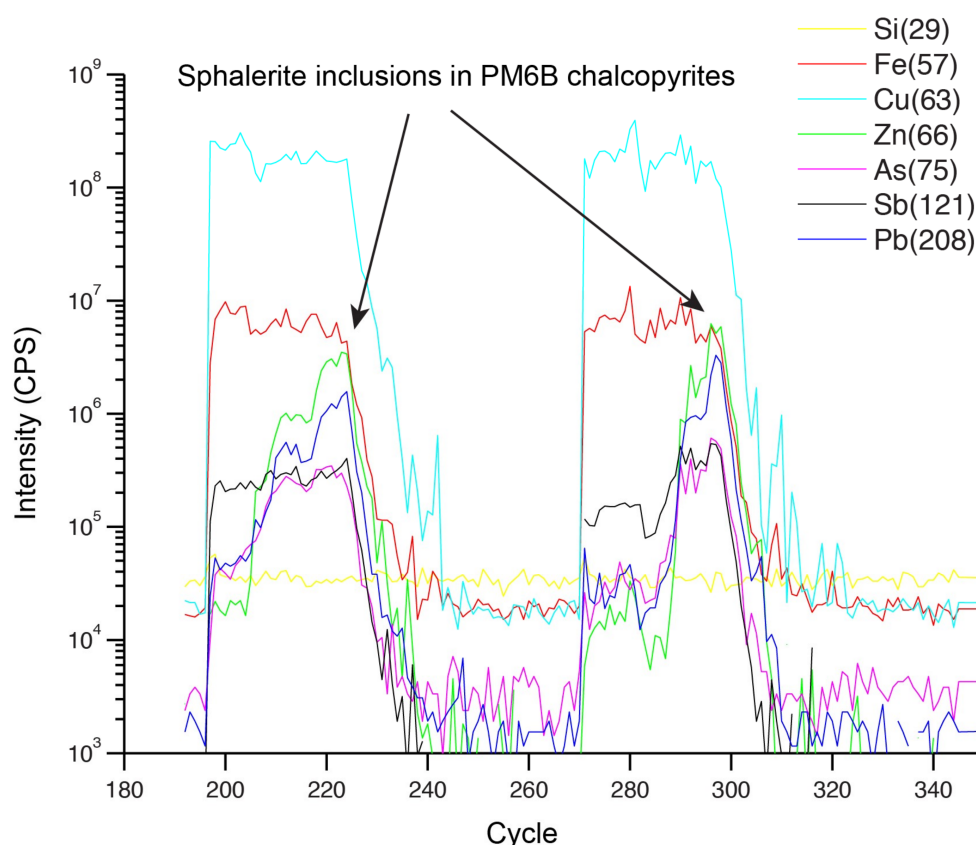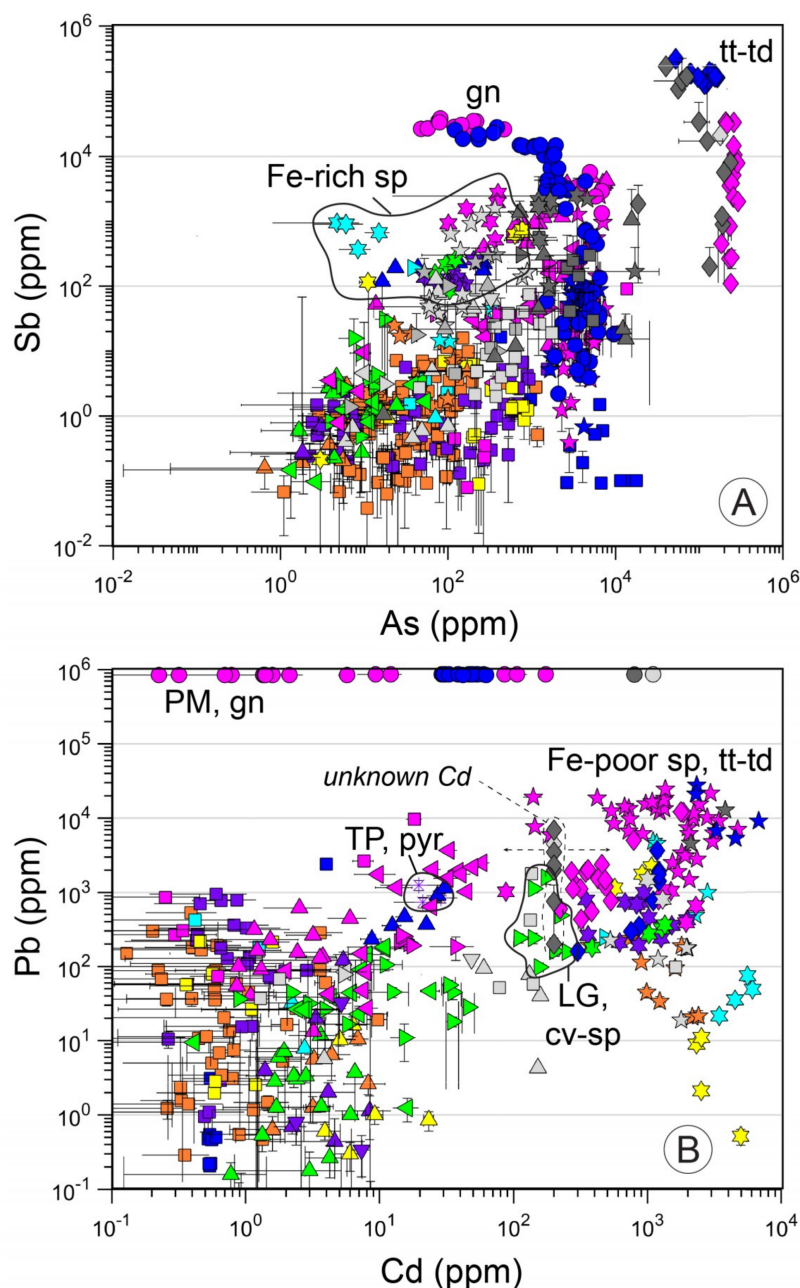
Figure 3. Laser ablation spectra with display of background signal for 7 elements (Si, Fe, Cu, Zn, As, Sb and Pb). Shown here are signal rises of Zn and Pb in chalcopyrite minerals (Sample PM6B)—interpreted as sphalerite inclusions that are rich in Pb (therefore may contain galena as well). Where possible, concentrations from laser spots were calculated from the flattest parts of the ablation spectra, with inclusion-signal removed.

Figures 4–6 present the LA-ICP-MS dataset for Cu, Zn, Fe, Mn, As, Sb, Pb, Cd, Co, Ni, Bi and Ag separated by mineral type and geological setting (mature, immature, ultramafic, hot spot, back arc, volcanic arc) combined with data from the published literature (grey symbols, Table S8) to provide a larger number of samples and for comparison with the data from this study. In the case of Cd for tennantite-tetrahedrite and Bi for tennantite-tetrahedrite, galena, Cu-phases and sphalerite, an estimate is taken in order to present published Ag and Pb data.
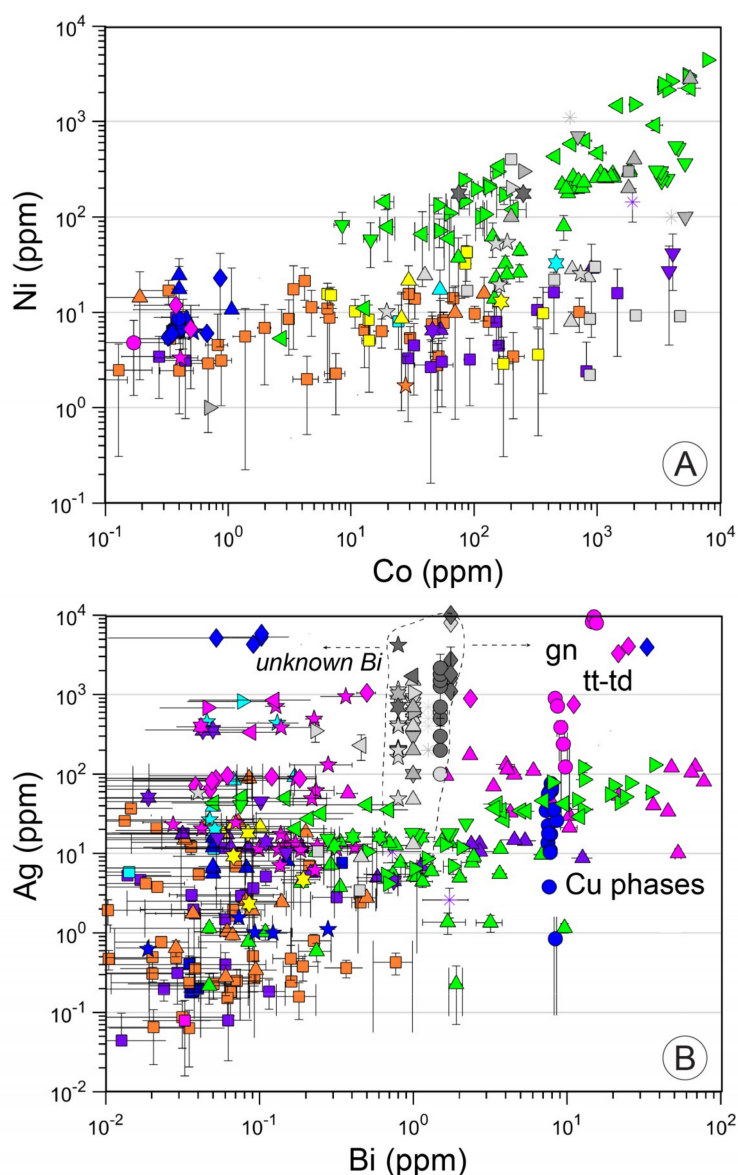
Cu, Zn and Fe are the major base metals observed in all SMS deposits, and consequently form their own minerals, however, all are observed in abundance (up to wt %) in other minerals (Figure 4A,B). Contrastingly, Mn is not present as its own sulfide mineral in SMS deposits and its highest concentrations are observed in sphalerite (Figure 4B, stars).
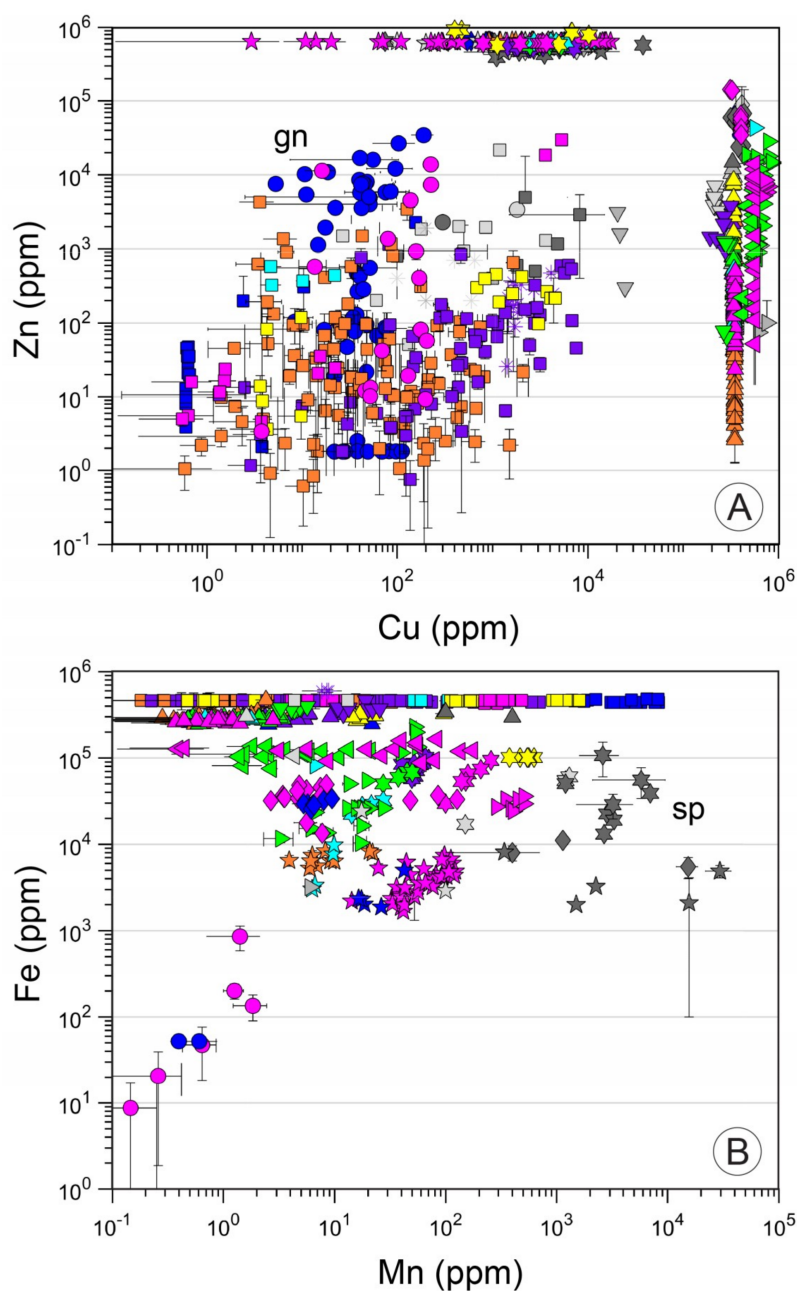
Figure 4. Logarithmic plots displaying a comparison of trace element concentrations (ppm) of (**A**) Cu versus Zn (**B**) Mn versus Fe in sulfide minerals from all hydrothermal vent sites investigated during this study. Abbreviations of minerals used in this figure include sp (*sphalerite*) and gn (*galena*). Shape denotes the type of mineral where squares: pyrite/marcasite, asterisks: pyrrhotite, triangles: Cu phases including downward-pointing triangle: isocubanite, upward-pointing triangle: chalcopyrite, right-pointing triangle: covellite/digenite/chalcocite, left-pointing triangle: bornite, diamond: tennantite-tetrahedrite, five-pointed star: Fe-poor sphalerite, six-pointed star: Fe-rich sphalerite, circles: galena. Colour dictates the tectonic setting where green: ultramafic-hosted MOR (Logatchev), orange: mature MOR (TAG), purple: high temperature MOR (Turtle Pits), cyan: immature MOR (SEPR), yellow: hot spot MOR (AS), magenta: back-arc basin (PM), blue: volcanic arc (PVC). Shown for comparison are data from the literature in grey-scale outlined in Table S8 (light grey: MOR, middle grey: ultramafic MOR and dark grey: arc-related).

Figure 5. Logarithmic plots displaying a comparison of trace element concentrations (ppm) of (**A**) As versus Sb (**B**) Cd versus Pb in sulfide minerals from all hydrothermal vent sites investigated during this study. Abbreviations of hydrothermal sites used in this figure include LG (*Logatchev*), and TP (*Turtle Pits*). Abbreviations of minerals used in this figure include sp (*sphalerite*), gn (*galena*), tt-td (*tennantite-tetrahedrite*), pyr (*pyrrhotite*) and cv (*covellite*). Shape denotes the type of mineral where squares: pyrite/marcasite, asterisks: pyrrhotite, triangles: Cu phases including downward-pointing triangle: isocubanite, upward-pointing triangle: chalcopyrite, right-pointing triangle: covellite/digenite/chalcocite, left-pointing triangle: bornite, diamond: tennantite-tetrahedrite, five-pointed star: Fe-poor sphalerite, six-pointed star: Fe-rich sphalerite, circles: galena. Colour dictates the tectonic setting where green: ultramafic-hosted MOR (Logatchev), orange: mature MOR (TAG), purple: high temperature MOR (Turtle Pits), cyan: immature MOR (SEPR), yellow: hot spot MOR (AS), magenta: back-arc basin (PM), blue: volcanic arc (PVC). Shown for comparison are data from the literature in grey-scale outlined in Table S8 (light grey: MOR, middle grey: ultramafic MOR and dark grey: arc-related).

Figure 6. Logarithmic plots displaying a comparison of trace element concentrations (ppm) of (**A**) Co versus Ni (**B**) Bi versus Ag in sulfide minerals from all hydrothermal vent sites investigated during this study. Abbreviations of minerals used in this figure include tt-td (*tennantite-tetrahedrite*) and gn (*galena*). Shape denotes the type of mineral where squares: pyrite/marcasite, asterisks: pyrrhotite, triangles: Cu phases including downward-pointing triangle: isocubanite, upward-pointing triangle: chalcopyrite, right-pointing triangle: covellite/digenite/chalcocite, left-pointing triangle: bornite, diamond: tennantite-tetrahedrite, five-pointed star: Fe-poor sphalerite, six-pointed star: Fe-rich sphalerite, circles: galena. Colour dictates the tectonic setting where green: ultramafic-hosted MOR (Logatchev), orange: mature MOR (TAG), purple: high temperature MOR (Turtle Pits), cyan: immature MOR (SEPR), yellow: hot spot MOR (AS), magenta: back-arc basin (PM) and blue: volcanic arc (PVC). Shown for comparison are data from the literature in grey-scale outlined in Table S8 (light grey: MOR, middle grey: ultramafic MOR and dark grey: arc-related).

The highest As and Sb concentrations are found in deposits forming within arc-related settings, where they often form as sulfosalts (tennantite-tetrahedrite solid solution series, Figure 5A, diamonds). Where present at high concentrations, Pb forms galena or Pb-sulfosalts, observed here only in samples from arc-related settings (Pacmanus and Palinuro). Notwithstanding the presence of galena, high Pb concentrations are also observed in Fe-poor sphalerite from all settings and sulfosalts (Figure 5B).

Cadmium is almost exclusively associated with sphalerite from all geological settings (Figure 5B, stars), but is also observed in tennantite-tetrahedrite from Pacmanus and Palinuro.

The highest average concentrations of Co (>1000 ppm) are observed in high-temperature forming minerals such as pyrrhotite and isocubanite from mafic to ultramafic-hosted sites (Turtle Pits and Logatchev). In contrast, the highest Ni concentrations in this study (>1000 ppm, Figure 6A) were only observed in sulfides from the ultramafic-hosted Logatchev (green symbols).

Bismuth concentrations in all phases from all settings are generally <100 ppm (Table S6). Ultramafic-hosted and back arc Cu-sulfides contain the highest Bi (green and magenta triangles), with averages ~5 ppm, and outliers at 10s of ppm (Figure 6B), although Bi was also observed to be high in galena from Pacmanus and Palinuro and sulfosalts from Pacmanus. However, the elevated [209]Bi observed in galena is likely to be the result of an interference contribution of [208]Pb-H$^+$ (~12 ppm) and can be disregarded. Silver is most abundant in sulfides from arc-related settings in this study (>100s to 1000s of ppm in galena and sulfosalts, and to a lesser degree in sphalerite and secondary-Cu sulfides from Pacmanus). Ag is also present in sphalerite and secondary Cu-sulfides from MOR settings investigated in this study.

Elevated Hg within the Palinuro sample suite allows an investigation into its distribution between particular sulfide mineral phases (Figure 7; shown for comparison are the only other Hg data available for SMS deposits: Palinuro and Hook Ridge—both associated with felsic host rocks and contributions from an exsolved magmatic fluid [84,109]). Based on this study, Hg is most abundant in sphalerite (2000 ppm up to 1.2 wt %) and tennantite-tetrahedrites (up to 4000 ppm, highest in tetrahedrite endmember).
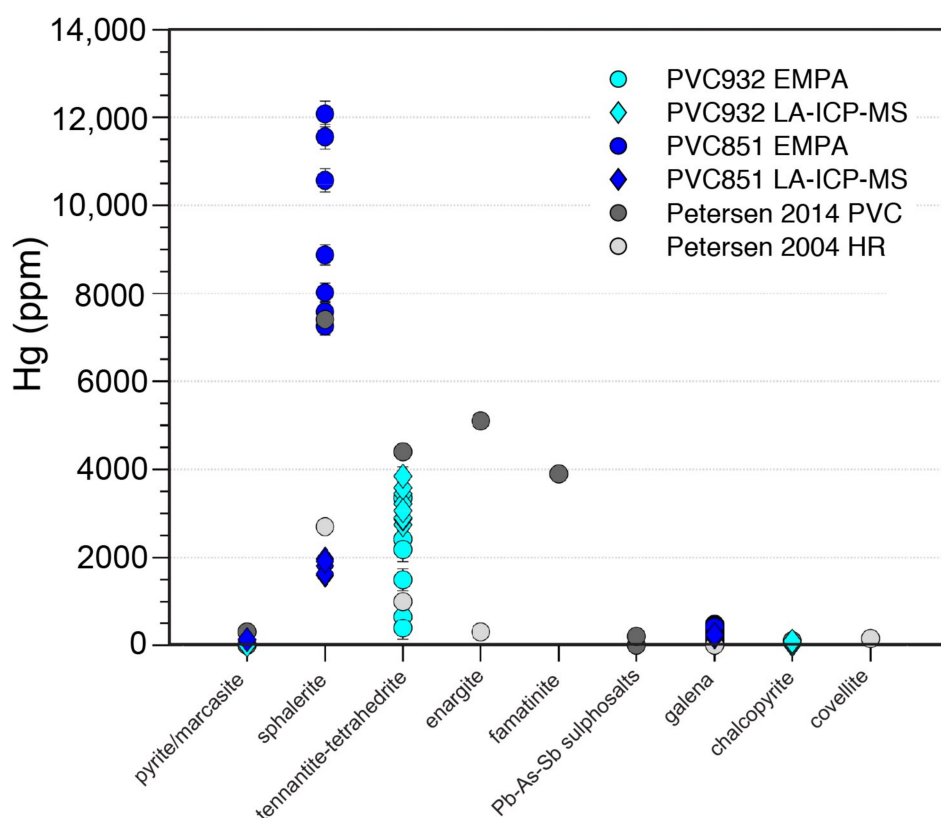
Figure 7. Hg (ppm) concentrations in pyrite, tennantite-tetrahedrite, sphalerite and galena from Palinuro based on EMPA and LA-ICP-MS analysis. Shown for comparison are Hg concentrations in a range of sulfide and sulfosalts minerals from Palinuro and Hook Ridge analysed by Petersen et al. (2014) [84] and Petersen et al. (2004) [109].

Principle component analysis (PCA) was undertaken using the MATLAB statistical toolbox "pca" to determine the major controls on trace element distribution across the LA-ICP-MS dataset including Fe, Cu, Zn, As, Sb, Pb, Cd, Mn, Co, Ni, Ag and Bi. Hg data from Palinuro are not included due to the non-availability of data for other samples (bdl). Prior to analysis, the dataset was z-scored (centred to have an arithmetic average of 0 and scaled to have a standard deviation of (1) to standardise the data so that all variables have a similar weight during PCA; this is particularly important when comparing the concentration of an element that is major in one mineral and a trace in another, e.g., Zn, Cu and Pb.

Four principle components that explain more than one variable's worth of information (8.3%, red line Figure 8A) have been identified and explain 64.2% of the variance in the dataset. Identification of the principle components was based on the coefficients calculated for each element. Principle component factor one (PC1) accounts for 21.3% of the variance has been identified as the concentration of magmatophile trace elements (Ag, Cd, Zn, Sb, As, Pb and Bi, Figure 8B), indicating that geological setting, e.g., MOR versus arc-related is a large control on trace elements. Whilst not possible to run PCA including Hg data, it can be expected that Hg would be associated with these magmatophile elements. This is consistent with other observations of elevated Hg at Palinuro as well as Hook Ridge [84,109]. However, superimposed on PC1 is mineralogy, with galena, sulfosalts and sphalerite displaying the highest magmatophile elements versus Fe-rich minerals of pyrite, pyrrhotite, marcasite and chalcopyrite.
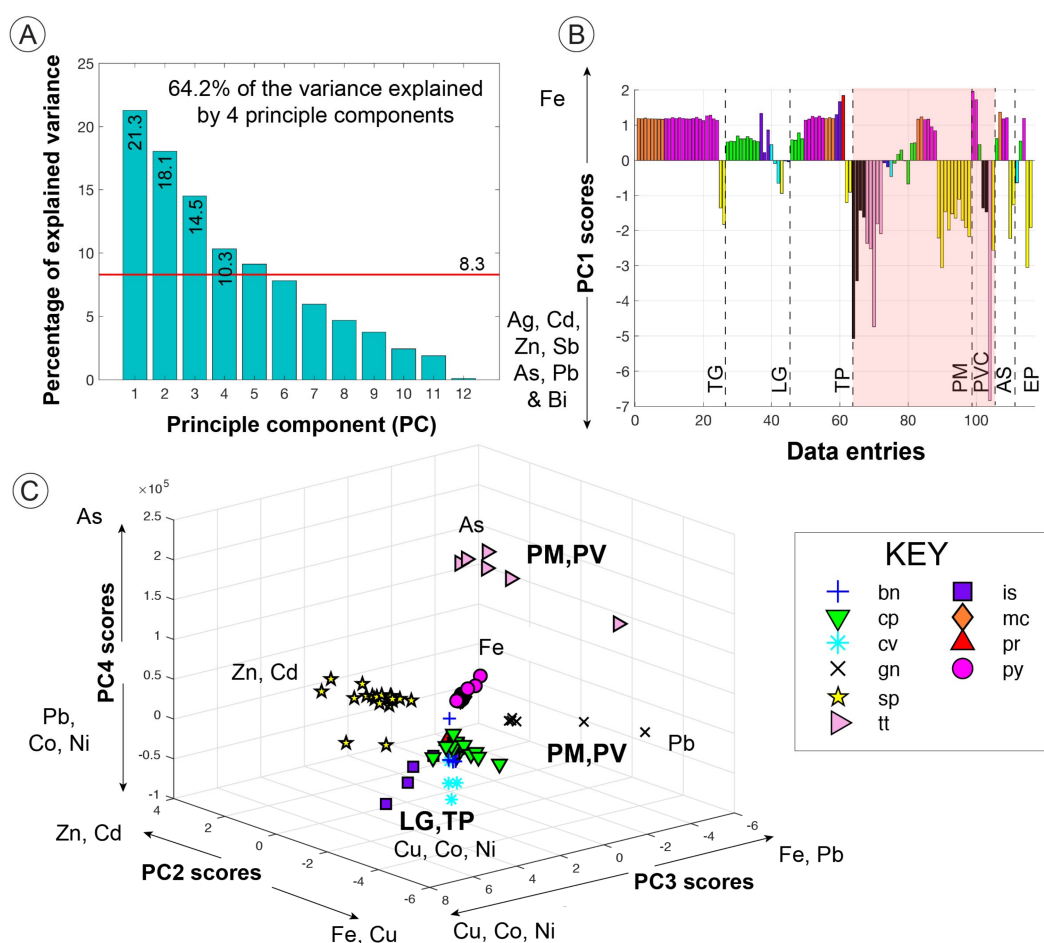
Figure 8. Principle component analysis (PCA) was undertaken across the z-scored LA-ICP-MS dataset including Fe, Cu, Zn, As, Sb, Pb, Cd, Mn, Co, Ni, Ag and Bi to identify principle components that control the concentrations of elements. (**A**) Four major principle components can explain 64.2% of the

variance in the dataset (**B**) The largest principle component (PC1) explains 21.3% of the variance. Based on the coefficients of each element (also known as loadings), those that positively contribute to PC1 are magmatophile elements Ag, Cd, Zn, Sb, As, Pb and Bi, whereas Fe negatively contributes. When PC1 scores of each data entry (mineral phase within each sample) are compared, those from Pacmanus and Palinuro are significantly higher, highlighting geological setting (arc-type) as a major control on element distribution, with mineralogy superimposed (sphalerite from other settings is a significant carrier of elements that could be toxic). (**C**) PC2 can be attributed to mineralogy, with Zn and Cd showing positive contributions (highlighting sphalerite), whereas Fe and Cu negatively attribute, separating pyrite/marcasite from chalcopyrite, galena and tennantite-tetrahedrite from sphalerite. Co and Ni contribute to both PC3 and PC4. PC3 highlights Cu-rich minerals including isocubanite, covellite, chalcopyrite and bornite from Logatchev and Turtle Pits (high-temperature and/or ultramafic-hosted), separating them from Fe and Pb minerals (pyrite, marcasite and galena). PC4 distinguishes the tennantite-tetrahedrite mineral series (Pacmanus and Palinuro) from all other sulfide minerals. Both PC3 and PC4 highlight a mineralogical control of trace elements that is superimposed on overarching geological setting and hydrothermal fluid temperature that provide elevated bulk concentrations of As, Pb, Co and Ni.

Factor PC2 accounts for 18.1% of the variance and is related to the mineralogy—specifically sphalerite (Zn) where it is the principle carrier of Cd (distinct correlation of the two, Figure 8C). Sphalerite from Pacmanus, Palinuro, East Pacific Rise and Axial Seamount in particular demonstrates the highest PC2 scores and thus the strongest association with Cd. Factor PC3 (14.5%) distinguishes Cu-rich mineralogy (isocubanite, covellite), from high-temperature sites Logatchev and Turtle Pits (sample TP4B) specifically, where Co and Ni are strongly correlated and PC4 (10.3%) highlights a positive association between Pb, Co and Ni and negative correlation with As, distinguishing tennantite-tetrahedrite (only found in arc settings in this study) from all other sulfide minerals. When factors PC2, PC3 and PC4 are plotted against one another (Figure 8C), a clear discrimination based on mineralogy is highlighted, irrespective of geological setting.

6. Discussion

6.1. Control of Geological Setting on Trace Element Distribution

Several publications over the past years have demonstrated the controls of the geological setting on the bulk chemistry of seafloor massive sulfides [63,66,67,110,111]. With our samples, we have selected sites from various geotectonic settings in order to encompass the full range of minerals and chemistry focusing on elements considered likely to form toxic species including Cu, Zn, Pb, As, Sb, Cd, Co, Ni, Mn, Ag and Bi. Excluding major elements Fe, Cu and Zn, it is clear from our results (shown in Figures 8 and 9) that the tectonic setting (including host rock composition and/or source of magmatic volatiles) is one of the major controls (PC1) of the distribution of potentially toxic elements (Ag, Sb, As, Pb, Bi), confirming the general tectonic implications discussed in the published literature and reiterated in the Introduction.

It is clear that arc-related SMS deposits (Pacmanus and Palinuro) display a distinct enrichment of Pb, As, Sb, Ag and Bi when compared to all other geological settings, consistent with studies in the literature [63,66,67,84], also highlighted in Figure S2. At these settings, the felsic host rocks and/or source of magmatic volatiles give rise to elevated contents of Pb, As, Sb and Ag, with volatiles more specifically associated with As, Sb and Bi ($\pm$Hg) [63,66,67,84,86]. This is shown in our study by the higher concentrations of these elements in Satanic Mills (Pacmanus) and Palinuro where magmatic volatiles are expected to be present based on low S-isotope ratios [112]. Whilst high bulk Zn and Cd concentrations are often observed in arc settings based on published studies [63,66,67], we demonstrate that they are not restricted to a particular setting as we also observe high Zn and Cd contents at both immature and hotspot associated MORs (Figure 9). It is clear from this that trace elements are not solely controlled by geological setting as emphasised by principle component analysis.
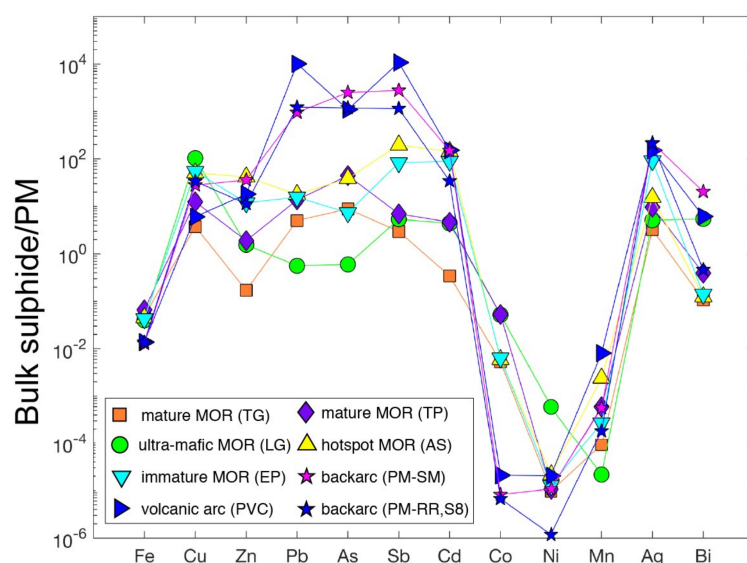
Figure 9. Bulk metal pattern (wt %) for the hydrothermal fields analysed in this study, split for Pacmanus into Satanic Mills where a magmatic fluid source is prevalent and Roman Ruins/Solwara-8 where it is not. Bulk metal pattern calculated based on average elements in each sulfide mineral normalised to modal sulfide mineral abundance according to XRD semi-quantitative data of each sample.

High Co in this study is exclusively associated with high-temperature sites (~400 °C) at MORs (Logatchev and Turtle Pits: (500 to 1000 ppm, Figure 9)), consistent with observations in the literature [108,113–115] and attributed to the solubility of cobalt at high temperature [116,117]. The presence of Ni is exclusively associated with ultramafic-hosted settings (here Logatchev, Figure 9) where Cu, Co and Bi are also enriched (Figure 9), which is in agreement with other studies at Logatchev [66,77,83,118] as well as other ultramafic-hosted sites including Rainbow Vent, Mid-Atlantic Ridge (see Figure 6A: middle grey symbols, [114,119,120]). Ultramafic-hosted as well as mature SMS deposits (LG, TAG) demonstrate a distinct absence of As, Sb, Pb, Hg, Ag, Mn and Cd when compared to other settings; consistent with the primitive host rock from these sites. In the case of TAG, Cu, Zn, Co and Ni concentrations are also considerably lower than Logatchev (Figure 9) due to extensive reworking and recrystallisation [121].

Immature, high-temperature and hot-spot related hydrothermal deposits (EP, TP, AS) lie in between the mature, ultramafic-hosted and arc-related end members in terms of metal content, where concentrations of As, Pb, Sb and Ag are generally 2–3 orders of magnitude lower than in arc-related settings (1 to 100s of ppm), consistent with observations from the literature. Instead of tectonic setting, it is clear that the trace content of these deposits is controlled by an interaction of a number of other variables.

6.2. Control of Mineralogy on Trace Element Distribution

Whilst tectonic setting (host rock and magmatic volatile contribution) has been identified as a significant control and ultimate source of trace elements (producing PC1 of 21.3%), it is clear from our observations that trace element distribution is also controlled by the physical properties of the hydrothermal fluid including H_2S contents, temperature and pH as well as subsequent oxidation and weathering [122–126] all of which are exemplified in the mineralogy we observe. This is evident whereby superimposed on PC1 is mineralogy, with galena, tennantite-tetrahedrite and sphalerite showing the highest scores, and high PC1 scores of sphalerite are also observed at MOR settings (Figure 8B). Factor PC2, (19% of the variance, Figure 8A), can solely be attributed to mineralogy, in particular—phalerite composition, again unrestricted to geological setting. Similarly,

PC3 and PC4 distinguish mineralogy with isocubanite/covellite showing the highest PC3 scores and tennantite-tetrahedrite showing the highest PC4 scores (albeit with temperature and tectonic setting superimposed respectively). If principle components 2, 3 and 4 are all linked to mineralogy (and ultimately the properties of the hydrothermal fluid), it can be stated that mineralogy is the largest control of the trace element distribution in our dataset (42.9%). Where mineralogy is the dominant control, the trace element distribution is a function of availability (source), the lattice sites available within each sulfide mineral and any subsequent substitution for major elements.

Combined with observations of trace element distribution in different sulfide minerals, the correlation coefficients between trace elements in selected mineral types were calculated (Table 5 and Figure 10). If trace elements are observed to be associated with one another in a particular sulfide, this information can be used to inform which minerals, textures and deposits have higher potential toxicity and which require stricter monitoring in terms of mining activity in the future. Based on sample size, P-values were calculated for each R-value present in the dataset. The P-value is the probability that the current result would be found if the correlation coefficient were zero (null hypothesis). If the P value (probability) is greater than 0.05 (at 95% confidence internal), the correlation coefficient is considered statistically insignificant and the associated R-value is no longer considered (presented as a dashed line on Figure 10).

Table 5. Correlation coefficients (R^2) for element pairs categorised by hydrothermal fields, minerals and texture. (-) Hyphens represent correlation coefficients that were calculated but are statistically insignificant: if the p-value is >0.05, see text for discussion. n.d. indicate where correlation coefficients could not be calculated as the element(s) were not analysed, e.g., Hg. Abbreviations used in this table include py (pyrite), mc (marcasite), pyr (pyrrhotite), cp (chalcopyrite), is (isocubanite), sp (sphalerite), cc-cv (chalcocite-covellite), bn (bornite), td (tennantite-tetrahedrite), gn (galena), I (colloform), II (porous) and III (massive).

	Mineral	Texture	As-Sb	As-Pb	Pb-Sb	Sb-Ag	Pb-Ag	Cd-Pb	Cd-Mn	Co-Ni	Fe-Mn	Cd-Fe	Sb-Hg
TAG	mc	III	0.3910	0.5970	-	0.5879	0.5078	-	-	-	-	-	n.d.
	mc	I	0.8947	-	-	-	-	-	-	-	−0.8609	-	n.d.
	py	III	-	-	0.6814	0.7214	0.7733	-	-	-	-	-	n.d.
	py	II	0.8340	0.7025	0.6486	0.8850	-	-	-	-	-	0.6667	n.d.
	py	I	0.9229	0.5772	0.6365	-	-	-	-	-	-	-	n.d.
	cp	III	-	-	0.5724	0.6688	0.7296	-	0.6748	-	−0.5522	-	n.d.
	cp	II	-	-	0.6588	-	-	0.3766	-	-	0.4722	-	n.d.
	sp	III	-	-	−0.9980	-	-	-	-	-	-	-	n.d.
	sp	II	-	0.8021	-	−0.7756	-	-	-	-	0.7768	-	n.d.
LOG	cp	III	0.3841	0.3999	0.4609	-	-	-	-	0.8784	-	-	n.d.
	is	III	0.7775	0.5228	0.5357	-	0.6280	-	0.4834	-	-	-	n.d.
	cv	III	0.4727	-	0.9537	-	−0.4673	0.5046	-	0.9927	0.9030	-	n.d.
	sp	III	-	-	0.9933	-	-	0.9817	0.9687	-	0.9639	0.9736	n.d.
	bn	III	-	-	0.8962	-	-	0.8747	-	-	-	-	n.d.

Table 5. *Cont.*

	Mineral	Texture	As-Sb	As-Pb	Pb-Sb	Sb-Ag	Pb-Ag	Cd-Pb	Cd-Mn	Co-Ni	Fe-Mn	Cd-Fe	Sb-Hg
TP	cp	III	-	-	0.9529	-	-	0.8056	0.8830	-	-	-	n.d.
	cp	I	-	0.7265	-	-	-	-	-	-	0.5826	-	n.d.
	py	I	-	−0.8105	-	-	-	-	-	-	-	-	n.d.
	py	II	0.8512	0.7216	0.6849	-	-	-	-	-	-	-	n.d.
	py	III	0.9082	-	0.7846	0.9665	0.7546	-	-	0.5881	-	-	n.d.
	mc	I	0.6872	-	-	-	-	-	-	-	−0.8707	-	n.d.
	mc	II	0.7659	0.9732	0.8402	-	-	-	-	-	−0.7547	-	n.d.
	is	III	-	-	-	-	-	-	-	-	-	-	n.d.
	pyr	III	-	-	-	-	-	-	-	-	-	-	n.d.
	sp	I	-	-	-	-	-	-	-	-	0.6190	-	n.d.
PM	gn	III	−0.8121	0.9629	−0.8394	0.7539	−0.7365	0.7186	0.5471	-	-	-	n.d.
	tt	III	-	-	-	0.6048	0.8267	0.8928	-	-	-	−0.8718	n.d.
	bn	III	0.9328	0.8261	0.6841	0.7776	0.8736	0.9702	0.8788	-	-	-	n.d.
	cv	III	-	-	-	-	-	-	-	-	-	-	n.d.
	mc	III	-	-	-	-	-	-	-	-	-	-	n.d.
	mc	I	-	-	-	-	-	-	-	-	-	-	n.d.
	py	III	-	−0.9489	0.7237	0.8683	0.8958	-	-	-	-	-	n.d.
	py	I	-	-	-	−0.9594	-	-	-	-	-	-	n.d.
	sp	I	-	0.9056	0.4871	0.8836	0.4133	-	-	-	0.7466	-	n.d.
	sp	III	−0.6794	-	-	0.9321	-	0.6272	-	-	0.9692	-	n.d.
	cp	I	0.8763	0.6385	0.8045	0.7283	0.6610	-	-	-	-	-	n.d.
	cp	III	-	-	-	-	-	-	-	-	-	-	n.d.

Table 5. *Cont.*

	Mineral	Texture	As-Sb	As-Pb	Pb-Sb	Sb-Ag	Pb-Ag	Cd-Pb	Cd-Mn	Co-Ni	Fe-Mn	Cd-Fe	Sb-Hg
AS	cp	III	-	0.8681	-	-	-	-	-	-	-	−0.7135	n.d.
	mc	III	-	-	-	-	-	-	-	-	-	-	n.d.
	py	III	-	-	-	-	-	-	-	-	-	-	n.d.
	py	I	-	−0.9071	0.9789	-	-	-	-	-	-	-	n.d.
	sp	III	0.9931	0.9731	0.9550	0.8374	-	-	-	-	-	-	n.d.
SEPR	cv	III	-	-	-	-	-	-	-	-	-	-	n.d.
	cp	III	-	0.9699	-	0.9681	-	-	-	-	-	-	n.d.
	py	III	-	-	-	0.9802	-	-	-	-	-	-	n.d.
	sp	III	-	-	-	-	-	-	0.9549	-	-	0.9653	n.d.
	sp	I	-	−0.9817	-	-	0.9957	-	0.9555	-	0.9750	-	n.d.
PV	gn	I	−0.5416	0.5472	−0.9764	-	0.4812	-	-	−0.5954	-	-	0.4438 * $p = 0.0851$
PV	py	I	-	-	-	-	-	-	-	−0.7288	-	-	n.d.
PV	tt	I	−0.9958	-	-	-	-	-	−0.8467	0.8309	0.7781	−0.7794	0.6772 * $p = 0.0650$
PV	cp	I	-	0.7924	-	-	-	-	-	-	-	-	n.d.
PV	sp	I	-	-	0.9774	-	-	-	-	-	-	-	n.d.

* $p > 0.05$.
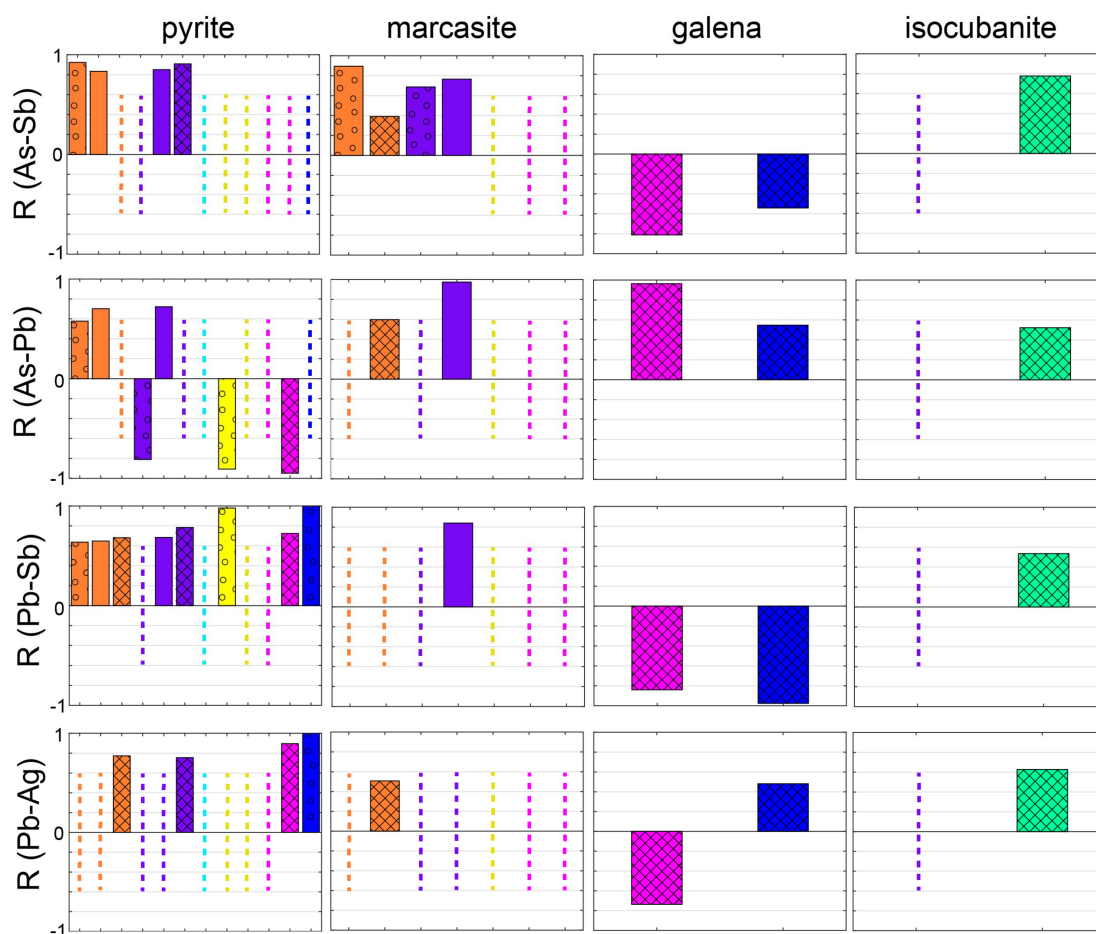
Figure 10. Correlation coefficients (R) for LA-ICP-MS trace data for pyrite, marcasite, isocubanite, and galena categorised by sample suite and texture using the elemental pairs As-Sb, As-Pb, Pb-Sb and Sb-Ag. Colour indicates sample suite where orange: TAG (*Trans-Atlantic Geotraverse*), purple: TP (*Turtle Pits*), cyan: SEPR (*South East Pacific Rise*), yellow: AS (*Axial Seamount*), magenta: PM (*Pacmanus*), blue: PVC (*Palinuro Volcanic Complex*) and green: LOG (*Logatchev*). Patterns highlight texture where circles: colloform, blank: porous and diamond: massive). Dashed lines indicate where any correlation is statistically insignificant.

6.2.1. Sphalerite (Cd, Pb, Cu, As, Sb, Mn and Hg)

The association of Cd with sphalerite (up to 1 wt %, Figures 5B and 8C) is a common observation and a reflection of the substitution of Cd for Zn in the sphalerite lattice [79]. Thermodynamic modelling has demonstrated that high temperature (Fe-rich) sphalerite is expected to be enriched in Cd [127], however based on this study and data from the literature, Cd does not appear to discriminate between low- and high-Fe sphalerite. The enrichment of these minerals is not limited to arc-related settings, with high Cd also observed in our samples from Axial Seamount and southern East Pacific Rise. Aside from Cd, sphalerite is also a significant host of Pb, As, Cu and Sb. High Pb concentrations (>1000 ppm Pb) is common in sphalerite from all settings, with elevated Pb identified in Fe-poor sphalerite from arc-related settings and the East Pacific Rise, consistent with literature [77,84,109,115,128], (Figure 5B. Petersen et al., 2014, 2004 [84,109]). The association of Pb with Fe-poor sphalerite could be due to the higher availability of lattice sites when Fe is lacking where Fe preferentially substitutes for Zn over Pb as a result of the similar ionic radii. Another (although unlikely) explanation is the presence of evenly distributed nano-inclusions of galena in Fe-poor sphalerite, which are associated with each other at lower temperatures.

Arsenic, Cu and Sb are abundant in sphalerite, consistent with data from the published literature (Figures 4A and 5A, grey stars). Whilst Cu and Sb appear to be present in a wide range of concentrations within Fe-poor sphalerite (10 ppm to 1 wt % Cu and 1–1000 ppm Sb), Fe-rich sphalerite is dominated by high concentrations (hundreds of ppm). This has been attributed to the high temperature reduced fluids that increase the solubility of these elements [77,129] and allow for coupled substitution of Sb^{3+} for $2Fe^{2+}$ with Cu^+ [97]. If this is the case, it might be expected that As^{3+} would take part in this coupled substitution to a higher extent as a result of its more similar ionic radius to Fe^{2+}; this is not observed in this study. This is likely to be a function of the strong temperature dependence of the equilibrium constants of As and Sb species/complexes where As has higher solubility than Sb at high temperature reduced conditions [130–133]. Similar solubility-controlled precipitation has been documented in geothermal waters, where stibnite (Sb_2S_3) is often observed as a precipitate, but no orpiment (As_2S_3) [133].

Based on data from this study and backed up by evidence from the literature, aside from making its own sulfosalt mineral (referred to as Hg fahlore by Petersen et al. (2014) [84]), Hg has a larger affinity for sphalerite than any other sulfide mineral, including galena. Whilst direct substitution of Hg^{2+} for Zn^{2+} and Pb^{2+} is suggested, the larger affinity of Hg for sphalerite over galena when both are present is perplexing. The size of the Hg^{2+} ion is within 15% of the Pb^{2+} ionic radius in galena, but well outside 15% of the ionic radius of Zn^{2+} in sphalerite. A likely suggestion put forward to explain this disparity, is that Hg^{2+} substitution is facilitated by direct solid solution with Hg-minerals including metacinnabar (HgS), tiemannite (HgSe) and coloradoite (HgTe) [97,134] that share the same structure as sphalerite.

Elevated Mn is clearly associated with Fe-rich samples and phases, particularly pyrite/marcasite and more commonly sphalerite (Figure 4B). The association of Fe, Mn, Cd and Zn in sphalerite is highlighted by positive R^2 values between Cd-Mn, Fe-Mn and Cd-Fe (Table 5, all >0.6) and can be explained by lattice substitution. Fe^{2+} and Mn^{2+} both substitute for Zn^{2+} in the sphalerite lattice; due to their similar ionic radius, they are both equally partitioned into the lattice; creating a positive correlation. Since Cd^{2+} is outside of the 15% ionic radius window of Zn^{2+}, it would be expected that Cd and Fe compete for lattice sites; with Fe preferentially partitioned creating a negative R^2 for the Fe-Cd element pair [79,97]. Instead, we observe a positive correlation of Fe with both Cd and Mn in sphalerite. This can be linked to the precipitation mechanisms that result in a co-enrichment of Fe and other trace elements in sphalerite precipitation from high-temperature fluids [108]. This is consistent with observations by Wohlgemuth-Ueberwasser et al. (2015) [77], who also observe a positive correlation of Fe with As, Sb, Au, Pb and Cu in sphalerite. The positive R-value for Fe-Mn is particularly important in terms of oxidation as Chen et al. (2010) [135] highlight that impurities of Mn, Fe, Ni, Cu, Sn and Pb favour the oxidation of sphalerite. The positive effect of Fe content in sphalerite on its dissolution rate is known from the published literature [136,137]. The association of Fe with elevated metal content combined with its higher potential for oxidation suggest that abundant Fe-rich sphalerite in SMS deposits poses high potential toxicity during mining.

Correlation coefficients for the element pairs As-Pb, Pb-Sb and Pb-Ag in sphalerite are generally positive, indicating that these elements are not in direct competition for lattice sites. Coupled substitution is playing a critical role based on the difference in oxidation states between the elements paired. Iron-rich sphalerite is often associated with high temperature reducing fluids, which have the ability to transport elevated concentrations of As, Sb, Pb and Ag, which could also explain the positive correlation. Furthermore, the presence of nano-inclusions of Pb-As sulfosalts may also occur and have been observed in sphalerite from Pacmanus (this study), and the East Pacific Rise [138]. For Fe-poor sphalerite at mature (sediment-poor) MOR settings (e.g., TAG, Turtle Pits, Logatchev) nano-inclusions of sulfosalts or galena are difficult to conceive due to low concentrations of As, Sb, Pb and Ag (in the vent fluids and bulk samples [77,83,124,139]). This positive correlation could simply be a result of the coupled substitution or general enrichment of As and Pb within Zn-rich assemblages extensively documented in the literature [122,138]. In contrast, sphalerite

shows inconsistent or statistically insignificant R^2 values of As-Sb in both this study and that of Wohlgemuth-Ueberwasser et al. (2015) [77]. Based on the similar size and ionic charge of As and Sb, a negative correlation might be expected, as a result of the difference in solubility of As and Sb at higher temperatures. A positive correlation has only been observed in Fe-rich sphalerite from Axial Seamount (AS), likely a result of increased solubility of both elements at higher temperatures as discussed earlier.

6.2.2. Galena (Sb, Zn, Ag, Cd and As)

With the exception of Sb-bearing sulfosalts, galena is a principle carrier of Sb in our sample suite (>1 wt %; Figure 5A). This is consistent with previous observations from various deposits such as Pacmanus, Okinawa Trough and Marianas Trench; [140–142]) and is explained by the coupled substitution of Pb^{2+} with Sb^{3+} and Ag^+. The latter also explains some of the highest Ag concentrations measured not only in this study (up to 1000 ppm Ag, Figure 6B), but also consistent with results from various hydrothermal fields across the globe regions [84,109,140–143]. Arsenic, Zn and Cd in galena on the other hand are variable (1 to 1000 ppm), likely a function of the presence of sulfosalt and/or sphalerite inclusions within galena.

In terms of R^2 values, negative correlations of As-Sb, Pb-Ag and Pb-Sb are observed due to direct competition for the Pb^{2+} lattice site (Figure 10) and in the case of As-Sb, Sb wins out due to its closeness in ionic radius to Pb^{2+} [97]. As-Pb, Pb-Cd and Sb-Ag R^2 values for galena are positive. As-Pb and Pb-Cd positive correlations are difficult to explain, where direct competition (similar to Pb-Sb) would be expected, however the presence of Pb-As sulfosalt and sphalerite nano-inclusions respectively could play a factor. Positive correlations between Cd-Pb are observed in Zn-rich bulk SMS samples from East Pacific Rise [138] and were likely due to the association of Zn-sulfides and galena.

In the computational (density-functional theory) studies of Chen et al. (2011) [70] for galena, it was suggested that trace impurities of Mn, and Sb lead to higher oxidation rates of galena. If applied to our context, elevated contents of Sb in galena are consistently seen in both this study and the published literature and could indicate a high potential toxicity during mining.

6.2.3. Tennantite-Tetrahedrite (Zn, Pb, Cd, Ag and Hg)

Sulfosalts, in particular, the tennantite-tetrahedrite solid solution series can be considered as the most significant carrier of potentially toxic elements found in SMS deposits. As a result of their complex crystal structure and large number of atoms [144], there is abundant opportunity for substitution with a wide range of elements. Zinc, Pb, Cd, Ag and Hg are all expected to substitute for Cu^{2+}/Fe^{2+}, with Zn > Pb > Cd/Ag, largely a function of availability whereas Bi^{3+} substitutes for As and Sb. As a result of the presence of Cu^+ as well as Cu^{2+} in tennantite-tetrahedrite, there are more available sites for Ag and Hg (present as monovalent cations), which may explain elevated concentration. This is consistent with published literature [84,109,141]. Minerals from the tennantite-tetrahedrite solid solution series are not only an important carrier of Cu, As and Sb (wt %), in our samples from Pacmanus and Palinuro they commonly also contain high concentrations of Zn (1000 ppm to 1 wt %), Pb (100s to 1000s of ppm) and Ag (10s to 1000s of ppm). This is consistent with observations from other hydrothermal fields elsewhere (Hook Ridge and the Okinawa Trough: grey diamonds, Figures 4A, 5B and 6B; [77,84,109,128,141,142,145]). Elevated Cd concentrations have also been found in tennantite-tetrahedrite from Pacmanus (Figure 5B, 10s to 1000s of ppm) and are observed to be at least an order of a magnitude higher in this study than those from Okinawa Trough—the only other study where Cd is analysed in tennantite-tetrahedrites [141]. Bi concentrations in tennantite-tetrahedrite are variable but can be high (10s of ppm). No other analyses of Bi concentrations in tennantite-tetrahedrite from SMS have been reported in the literature. Hg concentrations in tennantite-tetrahedrite from Palinuro are substantial (1000s of ppm Hg), although they are lower than those observed in associated sphalerite (Figure 7).

Analyses of minerals from the tennantite-tetrahedrite solid solution series show a positive correlation for the element pairs Pb-Ag and Cd-Pb (R = 0.827 and 0.893 respectively). This can be

explained by their substitution for different lattice sites, e.g., Ag^+/Ag^{2+} and Cd^{2+} for $Cu^+/Cu^{2+}/Fe^{2+}$ and Pb substituting into the As/Sb site involving a coupled substitution with a monovalent ion [98]. There is also a positive correlation between Sb-Hg in tennantite-tetrahedrite from Palinuro, with highest concentrations of Hg being observed in the Sb-rich end member (tetrahedrite) (mean 3200 ppm Hg, Table S6).

6.2.4. Pyrrhotite (Pb, Co, Ni, Cu and Zn)

The high-temperature mineral, pyrrhotite, has only been observed in one sample from Turtle Pits in this study. Based on published data, it is more common in SMS deposits from MORs (both volcanic and sediment-hosted) than back-arc spreading centres [66,146]. Aside from Fe, pyrrhotite hosts considerable concentrations of Co and Ni (100s to 1000s ppm), consistent with published literature from high temperature Rainbow vent field [114]. Our study also demonstrates some of the first analyses of Pb in pyrrhotite with elevated Pb concentrations (up to 1000 ppm) observed as well as 1000s of ppm Cu and 100s ppm Zn. All can be explained by either substitution for Fe^{2+} in pyrrhotite based on the similar ionic radii of Fe^{2+}, Zn^{2+} and Co^{2+} or the high-temperature fluids that increase solubility in the case of the larger Pb^{2+} cation.

6.2.5. Isocubanite (Zn, Co and Ni) and Chalcopyrite (Zn, As, Sb, Pb, Ag, Bi, Co and Ni)

Similar to pyrrhotite, isocubanite and chalcopyrite are high-temperature minerals. Isocubanite is largely found in MORs rather than arc-related settings and has only been observed in samples from Turtle Pits and Logatchev in this study. Aside from Fe and Cu, isocubanite shows the highest concentrations of Zn and Co (+Ni in the case of those from Logatchev) when compared to other minerals (>1000 ppm Zn, 100s of ppm Co and up to 1000 ppm Ni, consistent with published literature from high-temperature, ultramafic-hosted) Rainbow and Kairei vent fields [114,115]. Isocubanite from Logatchev demonstrates positive correlations for element pairs As-Sb, As-Pb, Pb-Sb and Pb-Ag (Figure 10).

In contrast, chalcopyrite is ubiquitous across SMS deposits, and can be considered a "relatively poor" trace element carrier [97]. Concentrations vary considerably as a function of geological setting (host rock) and temperature. Zinc concentrations in chalcopyrite from our dataset are variable (1 ppm up to 1 wt % Zn). This is consistent with observations of Zn in chalcopyrite from the literature (Figure 4A; [77,84,114,115,120,128,147]. Chalcopyrite from arc-related deposits often shows the highest concentrations of Sb, As, Pb and Ag; in particular—As and Sb, where concentrations >1 wt % have been observed (Figure 5A). Lead and Ag concentrations on the other hand are commonly <1000 ppm Pb (Figure 5B) and ~100 ppm Ag (Figure 6B), consistent with literature (grey triangles with unknown Bi, [113,146]). Chalcopyrite from the ultramafic-hosted Logatchev field shows elevated Ni (100s ppm), Co concentrations (up to 1000 ppm) with chalcopyrite from the basalt-hosted Turtle Pit field displays only elevated Co (up to 1000 ppm).

Lack of fully ionic structure of Cu-Fe sulfides makes it difficult to explain the partitioning we observe. Despite this, it is generally agreed that Cu^+ is the dominant valence state, explaining high concentrations of Ag, where both Ag^+ and Ag^{2+} can substitute for either Cu^+ or Cu^{2+} [97]. Similarly, Pb^{2+}, Ag^+, Bi^{3+}, As^{3+} and Sb^{3+} may take part in a coupled substitution with Fe^{2+}, Cu^{2+} and Cu^+, explaining the strong association of these elements with Cu-sulfides from arc-related settings. Elevated Zn, Co and Ni could be explained by a similar coupled substitution or direct substitution for Fe^{2+} in either isocubanite or chalcopyrite. Another explanation could be the potential presence of evenly distributed nano-inclusions of sulfosalts although this is deemed highly unlikely. More likely is the high temperature reducing fluids that carry elevated trace elements in the case of isocubanite. This can also explain the strong positive correlations between As-Sb (cp), As-Pb (all Cu minerals), Pb-Sb (all Cu minerals) and Sb-Ag (cp) that we observe, consistent with those observed in chalcopyrite from Pacmanus and Logatchev by Wohlgemuth-Ueberwasser et al. (2015) [77], where

coupled substitutions and fast precipitation of sulfide minerals from high-temperature fluids, reduce competition for lattice sites.

6.2.6. Secondary Cu Sulfides (Bornite, Covellite—Cu, Zn, Ag, Co, Ni, As, Sb and Bi)

Secondary Cu sulfides are similar to chalcopyrite in that concentrations vary considerably as a function of geological setting (host rock) and temperature. Zn in secondary copper sulfides varies between 100s of ppm up to >1 wt %, however the elevated concentrations are largely dictated by the intimate intergrowth of covellite and sphalerite in some cases (Logatchev, East Pacific Rise). Secondary copper sulfides from arc-related settings show elevated concentrations of As, Sb, Pb and Ag (100 s of ppm); all consistent with sparse published data from Pacmanus, Menez Gwen Field, Sonne Sulfide Field, Carlsberg Ridge and Hook Ridge [109,120,128,148,149]. Whilst highly variable, the highest Bi concentrations (only up to 100 ppm) are often associated with secondary Cu sulfides from arc-related settings as well as Logatchev and Turtle Pits. Similarly, some of the highest cobalt and Ni concentrations are observed in secondary copper sulfides from Logatchev, with concentrations up to 1000s of ppm. However, a positive R^2 value of element pair Co-Ni is seen in not only covellite, but also chalcopyrite and pyrite and likely reflects a temperature and host rock influence (geological setting) rather than mineral. The site-specific elevated concentrations seen in these secondary Cu-phases are also likely to be the result of secondary enrichment during oxidation of primary sulfides [76,150,151].

6.2.7. Pyrite/Marcasite (Zn, Cu, Mn, Pb, As, Co and Sb)

Pyrite demonstrates the widest range of trace metal concentrations, a conclusion also found by Libbey and Williams-Jones (2016) [116] and attributed to its stability over a wide temperature range and thus its abundant presence (and subsequent copious analysis) across a suite of SMS deposits that have formed at different conditions. In contrast, marcasite has a smaller stability field, explaining the lesser variation observed when compared to pyrite (Figures S3 and S4). Copper concentrations in pyrite and marcasite are variable but are commonly observed at concentrations >100 ppm Cu in our samples. This is consistent with published data (Figure 4A; [114,147,152]). Commonly, Zn concentrations lie above 100 ppm and are more often associated with pyrite than marcasite (Figure S3). Again, published Zn concentrations for pyrite are consistent with our study [84,109,114,115,140,152]. Pyrite that shows elevated concentrations of Cu, Zn (up to 1 wt %) is not restricted to a specific geological setting, largely due to the availability of these two metals across all sample suites. Based on their similar ionic radii, both Cu^{2+} and Zn^{2+} could substitute stoichiometrically for Fe^{2+} and explain the significant concentrations. In the case of Cu however, it is widely argued that in most ore-forming systems Cu is transported as Cu^+ and would therefore require a more complex substitution. Charge coupled substitutions involving Cu^+ with a 3^+ cation (Au, Ag and As) have been suggested in the literature [116,153–155]. Another potential explanation that is often put forward to explain not only high Cu and Zn, but also Pb are inclusions of other sulfide minerals. However, based on the uniform LA-ICP-MS signals (any data points with spikes have been removed from the dataset) and the unlikeliness of evenly distributed nano-scale inclusions, it is suggested that these high concentrations do exist in the crystal lattice of pyrite.

Elevated As and Pb concentrations are consistently observed in both in pyrite and marcasite, where they can reach 1 wt % As and 1000s of ppm Pb. The highest concentrations are commonly observed in samples from arc-related settings. Pyrite regularly shows As > Sb, where Sb concentrations may reach up to 100 ppm (only in arc-related settings). Arsenic occurs in several oxidation states, allowing it to substitute as either a divalent or trivalent cation for Fe^{2+} or anion (−) for S^- (perisulfide) in pyrite. It is has been suggested that substitution as an anion is most energetically favourable [69,116,154,156]. There is also suggestion that As^- non-stoichiometrically substitutes for S^{2-} to form AsS^{3-}, which is then involved in a charge coupled substitution for S_2^{2-} and a trivalent cation (Au, Ag, Tl and Mo) for Fe^{2+} [69]. Analogous to As, it is expected that Sb may be substituted in a similar fashion (SbS^{3-}) or through coupled substitutions with monovalent cations. However, the lower abundance in bulk

samples and lower solubility of Sb in comparison to As, could explain the lower Sb concentrations. Elevated Pb is more difficult to explain, because its large ionic radius when compared to Fe^{2+} should limit stoichiometric substitution. Also, the lack of Pb-spikes in the LA-IC-MS signals suggests that galena inclusions are unlikely. In the case of arc-related samples, elevated concentrations could simply be due to higher availability. High concentrations of Pb have also been found in pyrite from the basalt-hosted Turtle Pits (up to 400 ppm Pb). As these vents are characterised by some of the highest exit temperatures (>407 °C; [157]), these higher temperatures may provide a higher solubility of Pb when compared to other MOR sites.

The element pairs As-Sb, Pb-Sb and Pb-Ag all positively correlate within pyrite and marcasite (of all textures) from TAG and Turtle Pits (Figure 10) consistent with As-Sb behaviour in pyrite from Wohlgemuth-Ueberwasser et al. (2015) and Grant et al. (2018) [77,152]. Positive correlations between As-Sb are unexpected, where direct competition for lattice sites might be conceived unless there are substitutions occurring as both anions and cations for either As and/or Sb. Coupled substitutions or substitution for different sites can explain the correlation between the element pairs Pb-Sb and Pb-Ag.

Whilst elevated Mn is often observed with Fe-bearing phases due to their chemical similarity, Mn shows variable concentrations in pyrite/marcasite. This is largely a function of the overall Fe-content of the sample (and oxidation) rather than mineral or geological setting. Similarly, Co concentrations are variable in pyrite, ranging from 0.1 ppm up to 1000s of ppm. Highest Co concentrations in pyrite are observed in pyrite from high-temperature vent Turtle Pits, consistent with the geological setting (MOR) and the exit temperature-controlled solubility of Co. Where Co is available, stoichiometric substitution of Co^{2+} for Fe^{2+} is readily expected due to their very similar ionic radii.

When considering toxicity of mineral liberation, it should be noted that pyrite can be characterised as either primary p-type or n-type semiconductor by both stoichiometry (defects) and trace elements. The n-type pyrite semi-conductors are commonly found to contain high concentrations of Co and Ni and low concentrations of As whereas p-types have been shown to contain high As [69,158]. The type of semiconductor has a direct link with its oxidation behaviour, with n-type semiconductors (electron donators) generally being observed to have higher conductivities and ultimately higher oxidation rate. Thus, pyrite from TAG and Turtle Pits, where high Co and Ni concentrations are observed, can be predicted to have a higher oxidation rate over those from, for instance, Pacmanus.

6.3. Control of Texture on Trace Element Distribution

Three textures (colloform, porous and massive) have been distinguished and assigned to pyrite, marcasite, chalcopyrite and sphalerite during this study (Figure 11). These textures represent initial crystallisation (immature) through to fully recrystallised (mature) mineral phases. How replacement and recrystallisation processes impact trace concentrations can be discussed by comparing distributions within each texture. As the major control on trace element distribution is geological setting, it is only where data is available from multiple textures within one hydrothermal vent site that interpretations can be made with full confidence. Arrows in Figure 11 highlight a change in trace element concentration between different types of textures (colloform to porous/massive) observed within the same sample suite. Only discernible and consistent decreases in trace contents between colloform to massive textures are discussed; other changes are attributed to a range of initial trace contents between samples (Turtle Pits: py, mc). Minimal changes between textures observed in TAG (pyrite, chalcopyrite) can be accounted to the extensive reworking and replacement that has occurred throughout the deposits history [108,122,159].
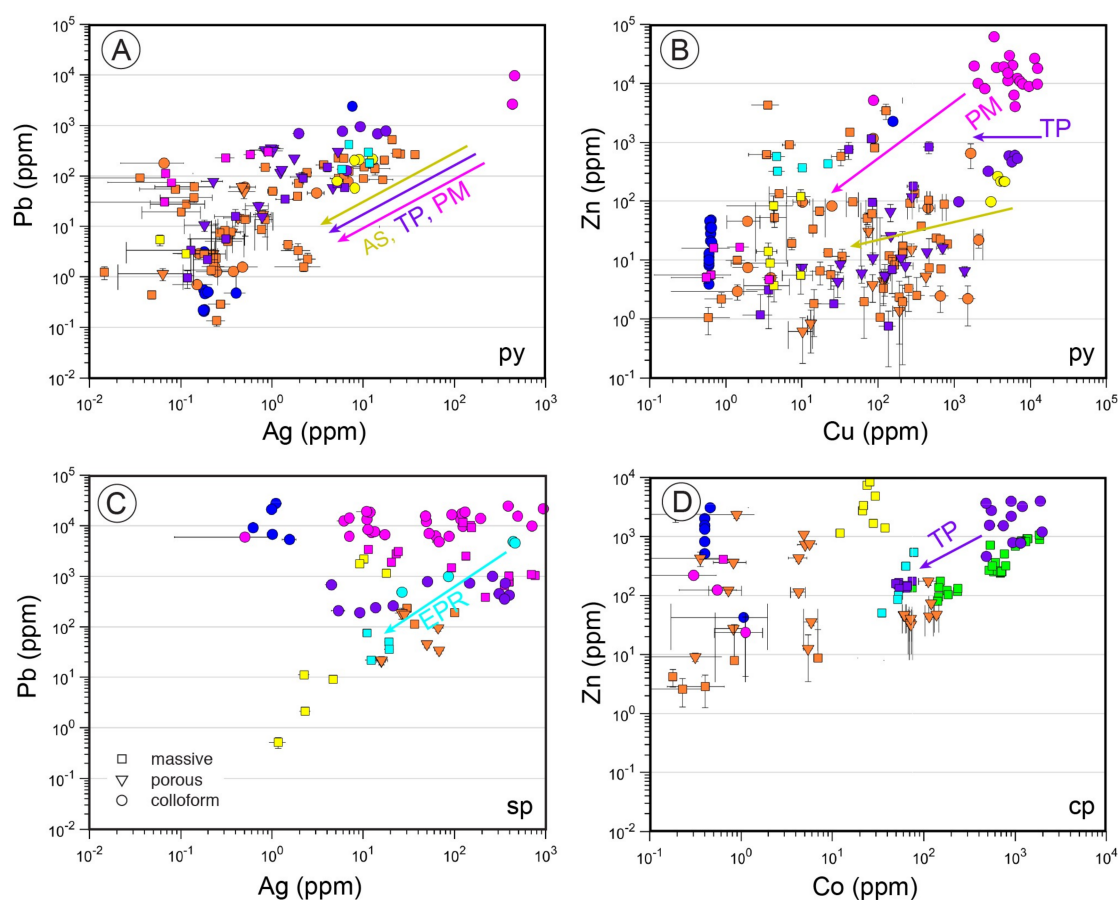
Figure 11. Trace element concentrations (Pb, Ag, Zn, Cu and Co) categorised by mineral type, sample suite (colour), and textures observed (shape). Logarithmic plots displaying the range of trace element concentrations (Pb, Ag, Zn, Cu and Co) for different textures (shape) of pyrite, chalcopyrite and sphalerite coloured by sample suite. Abbreviations for sample suite include AS (*Axial Seamount*, yellow), TP (*Turtle Pits*, purple), PM (*Pacmanus*, magenta), EPR (*East Pacific Rise*, cyan). (**A**) Pb versus Ag (pyrite); (**B**) Zn versus Cu (pyrite) (**C**) Pb versus Ag (sphalerite) (**D**) Zn versus Co (chalcopyrite). Coloured arrows highlight a change in texture from colloform to massive across one sample suite.

Colloform pyrite from Pacmanus, Turtle Pits and Axial Seamount displays some of the highest concentrations of Cu and Zn (Figure 11B) and Pb and Ag (Figure 11A) when compared to porous and massive textures. Grains from Pacmanus in particular are shown to host considerable quantities of potentially toxic elements, with As, Cu, Zn, Pb, Ag and Cd being abundant (Table S4). Across our study, only sphalerite in samples from the from Southern East Pacific Rise has different textures that also show a distinct decrease in As, Pb and Ag from colloform to massive textures (Figure 11C, cyan). Similarly, TAG, Turtle Pits and Pacmanus chalcopyrite demonstrate an order of magnitude decrease in particular trace elements (Zn: TAG; Zn and Co: Turtle Pits; Sb and Ag: Pacmanus) between colloform/porous to massive textures (Figure 11D, Table S6). There is a clear association of non-typical elements (As, Pb, Ag, Sb; >15% ionic radius than Zn^{2+}/Cu^+, Cu^{2+} in chalcopyrite and sphalerite) with immature (initial) crystallisation textures that are ultimately lost during recrystallisation.

Whilst particular samples show an association between colloform texture (pyrite, chalcopyrite) and higher concentrations of specific trace elements (Pb, Ag, Zn, Co and Cu), trends observed are not consistent across every site, mineral and/or element. In contrast, Lein et al. (2010) and Wohlgemuth-Ueberwasser et al. (2015) [77,120], consistently observed colloform and porous textures containing higher concentrations of trace elements. This is likely due to a larger sample set across a narrower range of sites. Our observations across a wide range of sites were unlikely to capture this

detail. Instead, our observations highlight the varied initial trace impurity and subsequent site and mineral specific recrystallisation. This ultimately emphasises the greater controls of tectonic setting, and mineralogy on the distribution of trace elements. However, on a site-by-site basis, due to their greater association of elevated trace contents and high surface area, we suggest that colloform minerals could pose a higher potential toxicity during mining than samples with more massive textures.

6.4. Potential Toxicity

Based on the current (but limited) published data of oxidation rates of individual sulfides in seawater (unavailable for secondary Cu sulfides, sulfosalts), vent sites with ores that contain a high abundance of pyrrhotite and marcasite are likely to oxidise faster, assuming all other variables equal (e.g., grain size, surface area) [24,160–164]. In terms of galvanic coupling, ores that contain abundant pyrrhotite, sphalerite, sulfosalts and/or galena in the presence of pyrite, chalcopyrite and/or marcasite have the potential to oxidise and release metals at a faster rate [12,165–169] and therefore need to be thoughtfully considered. This is due to their lower galvanic potential and subsequent predisposition to act as an anode and preferentially dissolve. In reality, mining will only occur where there is a high abundance of economically interesting sulfide minerals and their base metals including chalcopyrite, isocubanite, secondary Cu sulfides (Cu) for their Cu content, sphalerite/wurtzite (for Zn) and possible galena (for Pb) as well as high concentrations of precious and/or critical metals. In most cases, pyrite and/or marcasite will be present, and galvanic coupling is expected to occur and lead to an increase in preferential dissolution and release of metals to the water column, if not adequately balanced by oxidation. Furthermore, any minerals with colloform or porous textures that have higher surface areas should also be considered thoughtfully due to their higher potential to oxidise.

Ultimately, toxicity is dictated not only by the major and trace element concentrations of these more reactive minerals, but also by the realities of SMS mining and subsequent leaching, speciation and bioavailability of any leached metals as well as tolerance levels in these unique systems. Due to our limited understanding of these variables, we have no quantitative measure of toxicity of specific elements or minerals. However, based on the tendency of certain elements to form toxic species; as observed in submarine mine tailing studies, bioavailability studies including observations of bioaccumulation and behavioral avoidance as well as toxicity tests on deep-sea vent and background fauna (highlighted in the Introduction), we can discuss "potential toxicity" in this study [12,35]. These toxic species include non-essential micronutrients of Pb, Hg, Cd and Ag as well as essential (and more bioavailable) micronutrients Cu, Zn, As, Co and Ni. There is no information on the bioavailability or toxic nature of Sb and Bi within this context in the published literature; as a result, discussion of both is included under the assumption that they behave similar to As.

Certain minerals and deposits can be highlighted as posing more of a toxicity risk than others and thus might be avoided or dealt with appropriately during mining and mine closure. Major factors to be considered are the trace element distribution of certain mineral phases, textures and geological settings discussed above; with greater emphasis on mineralogy according to PCA. When these are combined with the abundance of mineral phases and pre-existing knowledge of oxidation rate of individual minerals and galvanic potential, the potential toxicity of different SMS deposit types can begin to be assessed (Figure 12).
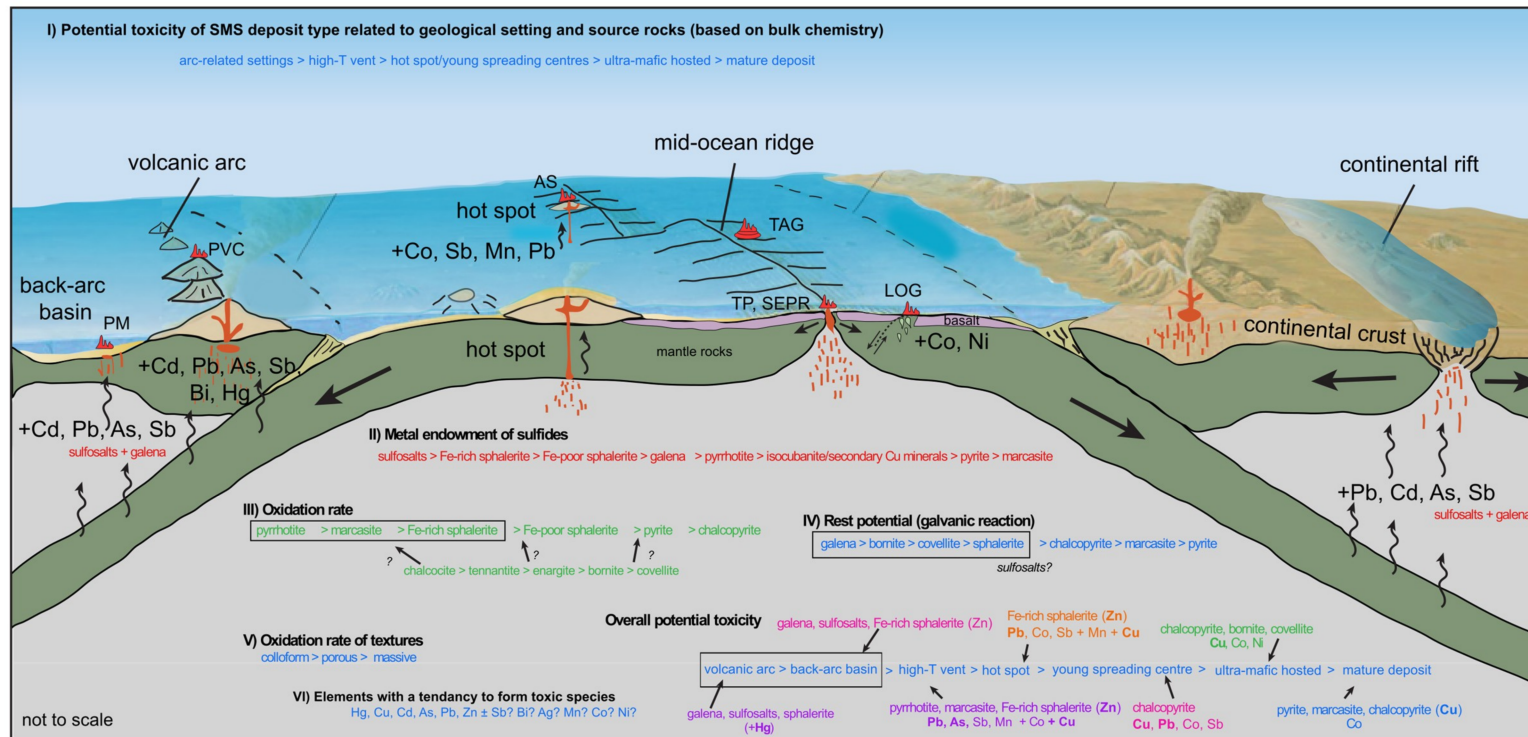
Figure 12. Visual representation of the variables that effect potential toxicity with assessments of inferred toxicity versus seafloor massive sulfides (SMS) ore deposit type (with schematic of geological settings) and mineralogy derived from the analyses performed in this study. (I) Potential toxicity based on bulk chemistry of different deposit types, (II) metal endowment (potentially toxic content) of sulfide minerals, (III) oxidation rate of each sulfide mineral, (IV) rest potential (galvanic reaction potential) of each sulfide mineral, (V) oxidation rate of mineral textures and (VI) elements with a tendency to form toxic species. The overall potential toxicity of deposit types (tectonic settings) is stated based on all variables to demonstrate the variation and highlight particular minerals and elements of concern for each. It is important to note that this is potential toxicity, and no recommendations of mining targets can be made without further quantitative toxicity data. Also shown are the potentially toxic trace elements commonly associated with each tectonic setting.

Based on the potential for oxidation as a function of oxidation rate and galvanic coupling (rest potential), the minerals that are the highest risk of oxidative dissolution are marcasite, pyrrhotite, sphalerite, sulfosalts and galena; even more so if they demonstrate colloform or porous textures. The presence of some of these minerals is ultimately controlled by a combination of geological setting and ore type (galena, sulfosalt) and temperature of the venting hydrothermal fluid (isocubanite/pyrrhotite associated with higher temperature, marcasite and galena with lower temperature and sphalerite and sulfosalts with both). These can then be combined with metal content/endowment (metals with a tendency to form toxic species in these environments) to evaluate potential toxicity.

Galena and sulfosalts (tennantite-tetrahedrite) analysed for this study are from volcanic-arc/back-arc ridge geological settings (Pacmanus and Palinuro). Galena is not restricted to these types of settings, however it is clearly a minor component of other geological settings [63,66]. Aside from the obvious potential Pb toxicity, Sb, Ag and Zn concentrations can be a concern as they are enriched in galena. Based on a recent dissolution study in seawater [164], galena is predicted to have one of the lowest dissolution rates across major sulfide minerals; albeit at high pH and non-oxidative conditions. Despite this, galena is known to have one of the lowest galvanic potentials across all sulfide minerals, making it important to consider in terms of potential toxicity. There is little known on the galvanic potential of sulfosalts, however, they are shown to oxidise quicker than other sulfide minerals [170]. Of all sulfide mineral phases, sulfosalts are the largest sink for toxic elements (many non-essential micronutrients with no metabolic function) including As, Sb, Pb, Cu, Zn, Ag, Cd and Hg and therefore have high potential to be toxic if liberated during oxidative dissolution.

Oxidation rates of sphalerite in seawater are limited to one study but indicate a quicker oxidation rate than that of pyrite and chalcopyrite which is consistent with acid mine drainage studies. In terms of galvanic potential, sphalerite would be anodically dissolved when in a cell with pyrite, marcasite or chalcopyrite, but would be protected if present with secondary Cu sulfides and/or galena. Sphalerite is not limited to a particular deposit type or geological setting, so has the potential to be toxic in all cases. All seafloor sphalerite is consistently shown to contain high concentrations of Cd (hundreds to thousands of ppm), irrespective of Fe concentrations (e.g., high or low temperature formation) and geological setting. However, Fe-rich sphalerite has much higher potential toxicity due to its higher oxidation rate than Fe-poor sphalerite, where elevated trace contents of Sb, Pb, As and Mn can be observed. It should be noted that at sites where Hg is present, sphalerite is the most likely of any other mineral phase to hold considerable quantities of Hg, demonstrating their potential toxicity. Mining sites where high Hg concentrations are present within sphalerite and sulfosalts need to be fully understood and constrained prior to mining. However, these type of deposits (e.g., Pacmanus) could be considered a preferential alternative when compared to vent sites such as the Bay of Plenty north of New Zealand which has a similar grade but higher Hg contents that produce native mercury and Hg-sulfides, i.e., cinnabar [68]. Further comparison of potential toxicity could be made if oxidation rates and galvanic potential of native mercury and Hg-sulfides were available.

Pyrrhotite has the highest oxidation rate of all sulfide minerals which makes it important to consider. Pyrrhotite analysed in this study is limited to one deposit (TP4B, Turtle Pits) representing typical sediment-free mid-ocean ridge deposits and is not seen in abundance in other geological settings analysed here. Abundant pyrrhotite has, however, been observed in sediment-hosted mid-ocean ridge deposits such as Middle Valley, Guaymas Basin and Southern Pescadero Basin [171–174]. The lack of pyrrhotite in other sediment-free settings is largely related to the presence of more oxidised fluids in the reaction zone of hydrothermal systems associated with subduction zones and volcanic arcs. Also, pyrrhotite becomes quickly oxidised in seawater [108]. Where pyrrhotite is observed in Turtle Pits, dissolved rims and replacement textures are common features. The texture together with the typical habit of pyrrhotite (lath shaped), leads to reduced areas available for LA-ICP-MS analysis. This explains not only the small trace element dataset available in this study, but also in the published

literature. The limited data show that pyrrhotite can host elevated concentrations of Cu, Pb and Co, and due to its oxidation rate, has high potential for toxicity.

Marcasite also requires some special consideration due to its high oxidation rate and presence across all geological settings. However, marcasite is not consistently associated with any particular trace element [122], where it is clear that ore deposit type and geological setting are the dominant controls of trace metal distribution within marcasite. Based on these inconsistent trends, the potential toxicity of marcasite-rich deposits should be considered on a site-by-site basis with detailed trace element studies at the site in question.

In terms of geological setting, SMS deposits formed in arc-related settings appear to pose high potential for toxicity when compared to other deposit types. Their combination of mineral phases with low rest potential or high oxidation rate (galena, sulfosalts) and endowment in a wide range of metals with a tendancy to form toxic species (Pb, As, Pb, Cd, Mn, Hg and Ag) result in a high risk of toxicity impact during mining. It is these deposits that are often host to the highest abundance of economic and precious metals (Cu, Zn, Pb, Au and Ag) and have gained the most interest in recent times [51].

Basalt-hosted SMS deposits that are mature after extensive natural weathering, reworking and replacement (TAG in this study) represent lower potential for toxicity and reduced environmental concern. Ultramafic-hosted sites have a high abundance of both relatively barren and less reactive chalcopyrite, resulting in a Cu-rich deposit that distinctly lacks As, Sb, Pb, Hg, Ag and Mn (Logatchev). Ultimately, ultramafic-hosted deposits like Logatchev could be of significant interest in terms of mining potential as a result of their abundance of Cu (economic worth) and reduced suite of other potentially toxic elements. However, the main concern with this style of deposit is what makes it of economic interest—Cu—which is consistently shown to be one of the most toxic trace metals in these systems [33]. Whilst chalcopyrite may oxidise slower, oxidation will still occur, and Cu will be released. Without quantitative data on relative toxicities between elements, it is difficult to compare toxicity associated with mining ultra-mafic versus arc-related deposits. Elevated Co and Ni could also be a concern based on their higher bioavailability, although predominantly observed in lesser abundant secondary copper phases (bornite/covellite). The oxidation rate of secondary Cu sulfides in comparison to chalcopyrite is quicker, but unknown in comparison to other sulfide minerals (e.g., sphalerite/pyrite; [170] and they are shown to have relatively low rest potentials. That being said, having only a few potentially toxic elements that are elevated enough to be an issue could be much easier to mitigate against during mining activities, in contrast to arc-related SMS deposits. This would be the case if time-intensive, element-specific assessments, avoidance measures and/or remediation is required e.g., Cd related toxicity may require different mitigation methods than Hg or As.

For the remaining basalt-hosted SMS deposits studied here (including the very high-temperature vent site Turtle Pits; the hot spot associated Axial Seamount fields and the young vent sites of the southern East Pacific Rise) where As, Pb and Mn are still present in considerable quantities lie somewhere in between in terms of potential toxicity. Here it ultimately comes down to the sample specific mineralogy rather than geological setting (e.g., mineral abundances, their trace contents and texture e.g., Fe-rich sphalerite, galena, marcasite, pyrrhotite, colloform/porous). An inactive chimney from Turtle Pits (sample TP4B) contains abundant colloform marcasite, Fe-rich sphalerite and pyrrhotite (~24, 34 and 2 wt % respectively, Table 4) that show higher potentially toxic trace contents and can be assumed to have a higher potential toxicity than the samples from Axial Seamount (sample AS1) and the southern East Pacific Rise (sample SEPR). Comparing the latter two sites, the abundance of Fe-rich sphalerite in our sample AS1 (29% sphalerite, Table 4) would indicate a higher potential toxicity than the sample from the southern East Pacific Rise (10% sphalerite, Table 4). However, without further quantitative data on the relative toxicity of different elements, no recommendations of mining targets can be made. This study can however, guide where precautions may be required to mitigate impact.

7. Conclusions

This study indicates how the characterisation of a deposits geological setting, mineralogy, trace element distribution, and texture can be used as a tool to help predict potential toxicity. When mineral types and the trace element distribution associated with specific ore deposits, are considered along with our current knowledge of oxidation rates, galvanic coupling and tendency of specific elements to form toxic species that are bioavailable, then deposit types and individual samples can begin to be characterised as having more or less potential toxicity. This information can highlight deposits of particular concern, and guide where precautions may be necessary during mining in order to minimise environmental impact.

Whilst deposits from arc-related settings do contain significant economic wealth, they also show some of the highest potential for toxicity in comparison to other deposit types. The combination of abundant As, Sb, Pb, Mn and Ag $\pm$ Hg (and subsequently more reactive galena and sulfosalts) along with the presence of Fe-rich sphalerite that contain considerable Cd give rise to high toxicity risk.

The potential toxicity of deposits that contain lower but still considerable contents of Pb, As, Sb, Mn and Cd can be considered on a sample by sample basis, where potential toxicity is ultimately related to mineralogy (mineral abundances and their specific toxic trace element content) rather than geological setting. Marcasite and sphalerite in particular are highlighted, which are ubiquitous across all SMS deposits, have higher oxidation rates in contrast to other sulfide minerals and can be host to elevated trace contents that have potential to be toxic.

Basalt-hosted, high-temperature vent formed deposits in particular are associated with elevated Co, Fe-rich sphalerite (themselves linked to high Sb) and pyrrhotite, which based on our limited analyses contains elevated Cu, Pb and Co, but requires further evaluation. Both of these minerals are known to have higher potential for oxidative dissolution (quick oxidation rate and low galvanic potential) when compared to other sulfide minerals, which when combined with metals with a tendency to form toxic species, could produce toxicity. Furthermore, deposits formed at lower temperatures with abundant colloform textures need to assessed carefully due to their higher potential for oxidation and likelihood of elevated concentrations of toxic elements in comparison to their massive textured counterparts.

It needs to be emphasised that the trade-off between economic value and toxicity may not always be negative. High temperature Cu-rich ultramafic-hosted deposits (Logatchev in this study) provide an interesting prospect where the abundance of the less reactive chalcopyrite (>80% in these samples) and distinct lack of As, Pb, Sb, Hg and Mn in comparison to other deposits leads to a low potential for a wide range of toxicity. However, before recommendations of this type of mining target can be made, quantitative toxicity data regarding Cu is required.

Clearly, characterisation through mineral identification and trace element analysis can be considered a useful primary tool to aid in identifying the potential toxicity associated with mining specific deposit types. However, it needs to be emphasised that deposits are heterogeneous and for individual sites it is still important to consider the risk on a deposit-by-deposit basis.

In the future, supplementary leaching experiments would help to quantify any potential toxicity, and ensure a firm understanding of the leaching, adsorption (onto Fe oxy-hydroxides) and speciation processes. Whilst the characterisation study presented here and published leaching studies begin to highlight the potential for toxicity, neither can quantify toxicity without toxicity data which is specific to organisms, elements and speciation. This study clearly highlights our lack of understanding of metal tolerance levels for species living at active, inactive vent, weathering deposit sites as well as the surrounding deep ocean. Due to the impossible nature of predicting thresholds for local fauna as indicated by Hauton et al. (2017) [35], combining leaching experiments with relevant biological proxy organisms to assess "bulk lethal toxicity" will be necessary. Without determining this, it is impossible to fully constrain true toxicity and impact on these environments during mining based on our study alone. Combining initial "bulk lethal toxicity" assessments with a characterisation study such as ours that can be used throughout the stages of a mining project would allow areas that have

more or less potential for toxicity to be highlighted and provide recommendations of where to focus exploitation. Furthermore, if a particular area or mineral phases within a deposit cannot be avoided, this type of characterisation can provide an idea of where greater care needs to be taken during the mining process; guiding where extra operational precautions must be taken during extraction to limit environmental impact.

Author Contributions: Conceptualization, data curation, formal analysis, investigation, methodology, visualization, writing—original draft, writing—review and editing: E.K.F.; Data curation, formal analysis, investigation, methodology, supervision, writing—review and editing: M.F.; Funding acquisition, investigation, project administration, resources, supervision, writing—review and editing: S.P.; Funding acquisition, supervision, writing—review and editing: R.A.B.; Funding acquisition, project administration, resources: T.B.S.

Conflicts of Interest: The authors declare no conflict of interest.

Appendix A.

Appendix A.1. TAG, Mid-Atlantic Ridge

Mineralogy within the TAG active mound is dominated by pyrite but varies as a function of depth and locality. In general, TAG samples can be characterised as massive sulfide, massive pyrite breccias or semi-massive pyrite-anhydrite breccias [99,107]. The three samples from TAG-1 (20 m SE of Black Smoker Complex) are dominated by porous and massive pyrite, with no marcasite observed. Sphalerite is also not observed in any of these samples, consistent with the observations of low Zn (<700 ppm) in the general TAG-1 area [175]. Porous chalcopyrite is common in two samples from TAG-1 (6F, 27), consistent with high bulk Cu observed within TAG-1 (up to 6 wt %; [175]) however is only large enough for LA-ICP-MS analysis in one sample (6F). Intergrown chalcopyrite and isocubanite is also observed in TAG-27 (representative of high temperature assemblage), however is too porous and fine grained for LA-ICP-MS analysis.

The majority of TAG samples investigated during this study are from TAG-4, 20 m west of the active Black Smoker Complex (6 samples, Table 5). Consistent with all TAG samples, those from TAG-4 are dominated by pyrite, with additional marcasite also common, all occurring in massive, porous and colloform textures. Sphalerite is common in shallow samples from TAG-4 (intermediate temperature assemblage) and is predominantly porous in texture and exclusively intergrown or present as inclusions within euhedral marcasite and pyrite. Sphalerite large enough for LA-ICP-MS analysis is only observed in two samples (TAG-H and TAG-47). Based on EMPA data, sphalerite has Fe contents that range from 0.8 to 3.27 wt % with inclusions in TAG-46 showing highest Fe concentrations ranging from 7.8 and 8.6 wt % (Table S4, major elemental data—sphalerite). With greater depth (within borehole 957K of TAG), chalcopyrite becomes more abundant as observed in TAG-46 and TAG-J (higher temperature assemblage). Chalcopyrite is exclusively porous in texture and fine-grained covellite is common within its pore spaces, although covellite is not large enough for LA-ICP-MS analysis.

Two pyrite-anhydrite breccia samples from the TAG-5 region (20–30 m north of the Black Smoker Complex) were also investigated, with anhydrite being the major component (Table 4). Nodular to

angular massive grains of pyrite are observed in each sample. Massive chalcopyrite is commonly observed in both whilst sphalerite is not (Table 5), consistent with bulk chemical data for the TAG-5 region as a whole where Zn contents are low (0.03 wt % Zn and Cu contents are observed to be high (3.7 wt % Cu [107]).

Appendix A.2. Turtle Pits, Mid-Atlantic Ridge

Two samples from Turtle Pits were investigated in this study, one from an outer part of an inactive chimney talus piece lying on the flanks of a sulfide mound (TP2L) and the other from an active chimney wall from "Southern Tower" (TP4B). Pyrite makes up the majority of TP2L, present in both colloform (with growth banding) and massive textures, with euhedral marcasite also common (Table 5). Massive chalcopyrite grains are present, often observed to be sub-angular, cracked and lie within pore spaces. Whilst sphalerite is observed as inclusions (too small for LA-ICP-MS analysis), it is likely to be present at <1 wt % in the bulk sample based on XRD patterns.

In contrast, TP4B represents high-temperature Cu-rich sulfide from the interior of the chimney. Intergrown chalcopyrite and isocubanite are common, display colloform texture and are often intergrown with minor colloform sphalerite and associated with early and later formed colloform marcasite (Figure 2B). Pyrrhotite laths are present in trace amounts (Figure 2B', Table 5), are observed in pore spaces, intergrown with high-temperature associated isocubanite but commonly display oxidised rims. As a result of their grain size and shape (10–30 um wide), pyrrhotite was inherently difficult to analyse using LA-ICP-MS, however a few analyses were completed. Chalcopyrite dominant areas are also common, where it is observed to overgrow high-temperature isocubanite. Pyrite makes up the highest proportion of sulfide (Table 5), and displays euhedral massive textures, often replacing marcasite around its rims.

Appendix A.3. Logatchev, Mid-Atlantic Ridge

Two samples were investigated from Logatchev-1 hydrothermal field along the Mid-Atlantic Ridge; one from an inactive chimney at "Candelabra" (LOG11) and the other from the talus of an active black smoker chimney at "Irina" (LOG13) as shown in Figure 1E. Both samples are representative of the interior of a fresh black smoker chimney higher temperature assemblage as well as the replacement zone. The majority of both samples consist of massive chalcopyrite (recrystallised to massive from colloform banding in the case of LOG13), with LOG11 commonly displaying intergrowths with isocubanite either as exsolution lamellae or veins (latter seen in Figure 2C). Minor secondary copper sulfides including bornite and covellite are observed along grain boundaries, fractures, pore spaces and between growth banding of chalcopyrite-isocubanite in LOG11. Similarly, bornite, covellite-digenite and atacamite are observed between the growth bands of chalcopyrite in LOG13. Rare to minor sphalerite is observed in both samples, within pore spaces and where present shows porous textures and dissolved rims. Iron concentrations in sphalerite range from 6.6 to 10.5 wt % (Table S4) in LOG11, indicative of the high temperatures and low volatiles associated with this vent system [83,129]. In contrast, sphalerite in LOG13 was not large enough for LA-ICP-MS analysis, and iron concentrations by EMPA are lower (1.1 to 2.2 wt %, Table S4).

Appendix A.4. Axial Seamount, Juan de Fuca Ridge

A fresh, unoxidised Cu-rich inactive chimney was collected from the ASHES vent field and investigated during this study. Chalcopyrite and sphalerite make up the majority of the sample (representative of high and intermediate temperature zones) and are commonly observed with massive textures, with sphalerite also displaying colloform. Only massive textures were analysed due to the smaller grain size of the colloform textures. Based on EMPA, iron concentrations in sphalerite are high and range from 9.2 to 15.5 wt % (Table S4), suggestive of either high temperature or low sulfidation conditions; based on the setting and high abundance of chalcopyrite, it is more likely to be indicative of high temperature [129]. Pyrite is abundant and present in a range of forms including

colloform, colloform with growth banding, massive euhedral and replacing marcasite; with colloform textures being most common (Figure 2E). Marcasite is only present in minor quantities and either forms colloform or massive textures, only massive textures were analysed with LA-ICP-MS.

Appendix A.5. 16°43'S hydrothermal Field, South East Pacific Rise

A sample (SEPR) was taken from an inactive chimney at a hydrothermal field located at 16°43'S. Sample SEPR is most representative of a higher temperature assemblage with its high abundance of massive chalcopyrite, however some areas are a mix of high and intermediate due to their abundance of pyrite and sphalerite. The sample shows abundant sedimentary textures (conglomerate layers, Figure 2D) indicating incorporation of fine sulfide talus and sand into the chimney. Pyrite is often observed replacing marcasite evidenced by the stalactitic marcasite crystal habit, however more massive and euhedral pyrite grains are present in sedimented areas (Figure 2D); only pyrite crystals replacing marcasite were large enough for LA-ICP-MS analysis. Sphalerite is observed in pore spaces and displays both colloform and massive textures; both are analysed using LA-ICP-MS. Iron concentrations in colloform sphalerite range from 0.3 to 0.97 wt % whereas massive sphalerite (often showing dissolved rims) display between 2.2 and 3.2 wt % (Table S5). Trace fine-grained covellite and bornite are also observed, occasionally intergrown with sphalerite.

Appendix A.6. Pacmanus Basin, Papua New Guinea

A total of four samples from the Pacmanus hydrothermal field were investigated during this study (Table 5): two samples from an active chimney in the Satanic Mills area (PM5E, PM6B), one sample from an inactive chimney in the Roman Ruins area (PM2D) and the last from talus of a large chimney in the Solwara-8 area (PM2F) as shown in Figure 1F.

Sample PM5E is representative of a mixture of high and intermediate temperature assemblages with its high abundance of chalcopyrite, tennantite-tetrahedrite and sphalerite whereas sample PM6B is more representative of intermediate to lower temperature assemblage due to its higher abundance of sphalerite and pyrite, and minor presence of chalcopyrite (Table 5). Barite concentrations are significant in both samples. Chalcopyrite is always colloform and associated with tennantite-tetrahedrite and sphalerite. Massive euhedral marcasite is observed as trace in both, rimming earlier colloform sphalerite. Sphalerite forms exclusively colloform textures in both samples (Figure 2G). It is, however, associated with different mineral assemblages. Where sphalerite is intimately intergrown with chalcopyrite, it can be considered a high temperature mineral whereas sphalerite mainly intergrown with colloform pyrite, galena and Pb-sulfosalts suggests a lower formation temperature. Sample PM6B is dominated by this latter mineral assemblage. Iron concentrations in sphalerite from both samples range from 0.28 to 3.2 wt % (Table S4). Sample PM6B contains higher concentration of pyrite and galena than PM5E. Lead sulfosalts and fine-grained colloform chalcopyrite were not large enough for LA-ICP-MS, however EMPA analysis was undertaken on the colloform chalcopyrite.

Sample PM2D represents the lower temperature pyrite-sphalerite assemblage that is common for Roman Ruins; [176,177]. PM2D consists of abundant dacite clasts and significant barite, both of which have formed early in the paragenetic sequence, with sulfide minerals forming onto and around the rims of these clasts and crystals. Sphalerite is most commonly observed in colloform textures, and iron concentrations range significantly from 1.3 to 8.9 wt % (Table S4). Fine-grained euhedral galena and Pb-sulfosalts are observed as trace (galena up to 4.3 wt %, Table 5), and exclusively associated with sphalerite. Trace (<1 wt %) chalcopyrite is observed, but usually fine-grained and colloform in texture. Pyrite is observed in colloform, porous and massive textures, however only massive (early formed) is analysed using LA-ICP-MS. Later formed finer grained colloform pyrite (exclusively intergrown with colloform sphalerite) was too small for LA-ICP-MS, however some EMPA analyses were undertaken. Euhedral marcasite is also present in minor concentrations, associated with early-formed massive pyrite.

Sample PM2F is most representative of a higher temperature mineral assemblage, one that is also experienced oxidation, based on its high abundance of chalcopyrite, tennantite, secondary copper sulfides and atacamite (Figure 2F). Aside from barite, chalcopyrite is the most abundant mineral and forms anhedral textures with complex intergrowths with other sulfides indicating intermediate temperatures of formation. Secondary copper sulfides (bornite, covellite-chalcocite) and atacamite are abundant and always associated with the chalcopyrite that they are replacing during oxidation (along grain boundaries and pore spaces). Sphalerite is present, exclusively euhedral in texture and demonstrates variable formation temperature. Iron concentrations in sphalerite are low and range from 0.18 to 1.6 wt % (Table S4). Tennantite is intergrown with chalcopyrite and sphalerite forming both massive and rare euhedral textures, only massive were analysed with LA-ICP-MS.

Appendix A.7. Palinuro Volcanic Complex, Aeolian Island Arc, Italy

Two samples (851-RD and 932-RD) were collected from the sub-seafloor SMS deposit located in the Palinuro Volcanic Complex. The two samples used in this study are from the vuggy-barite zone, and most likely formed at lower temperatures as indicated by the dendritic and sometimes colloform textures (Figure 2H). Sample 851-RD consists of abundant barite and fine-grained sphalerite, pyrite, galena as well as other non-sulfide minerals (Figure 2H, Table 5). Iron concentrations in sphalerite are very low and range from 0.25 to 0.32 wt %, which is expected based on evidence of intermediate to high sulfidation conditions at this site [84]. Sample 932-RD contains a higher abundance of pyrite, lower sphalerite and less galena (Table 5). Similar to 851-RD, colloform textures occur, although coarser and euhedral crystals are more common. Sulfosalts are common in both samples, with tennantite-tetrahedrite observed in 932-RD whereas jordanite (Pb-sulfosalts) was more common in 851-RD, associated with galena.

References

1. CLCS Oceans and Law of the Sea, United Nations. Available online: http://www.un.org/depts/los/clcs_new/commission_submissions.htm (accessed on 4 March 2019).
2. Organisation for Economic Co-Operation and Development (OECD). *The Ocean Economy in 2030*; IWA Publishing: London, UK, 2017; ISBN 1780408919.
3. Gwyther, D. *Environmental Impact Statement, Solwara 1 Project*; Coffey Natural Systems Pty Ltd.: Brisbane, Australia, 2008; Report No.: CR 7008_09_v4.
4. Fallon, E.K.; Niehorster, E.; Brooker, R.A.; Scott, T.B. Experimental leaching of massive sulphide from TAG active hydrothermal mound and implications for seafloor mining. *Mar. Pollut. Bull.* **2018**, *126*, 501–515. [CrossRef] [PubMed]
5. Fuchida, S.; Ishibashi, J.; Shimada, K.; Nozaki, T.; Kumagai, H.; Kawachi, M.; Matsushita, Y.; Koshikawa, H. Onboard experiment investigating metal leaching of fresh hydrothermal sulfide cores into seawater. *Geochem. Trans.* **2018**, *19*, 15. [CrossRef] [PubMed]
6. Fuchida, S.; Yokoyama, A.; Fukuchi, R.; Ishibashi, J.; Kawagucci, S.; Kawachi, M.; Koshikawa, H. Leaching of Metals and Metalloids from Hydrothermal Ore Particulates and Their Effects on Marine Phytoplankton. *ACS Omega* **2017**, *2*, 3175–3182. [CrossRef] [PubMed]
7. Simpson, S.; Angel, B.; Hamilton, I.; Spadaro, D.; Binet, M. *Water and Sediment Characterisation and Toxicity Assessment for the Solwara 1 Project*; Coffey Natural Systems Pty Ltd.: Brisbane, Australia, 2007; CSIRO Land and Water Science Report 68/07.
8. Parry, D.L. *Solwara 1 Project Elutriate Report Phase 1 and 2*; Coffey Natural Systems Pty Ltd.: Brisbane, Australia, 2008; Tropical Futures: Mineral Program Charles Darwin University Report.
9. Knight, R.D.; Roberts, S.; Cooper, M.J. Investigating monomineralic and polymineralic reactions during the oxidation of sulphide minerals in seawater: Implications for mining seafloor massive sulphide deposits. *Appl. Geochem.* **2018**, *90*, 63–74. [CrossRef]
10. Rimstidt, J.D.; Chermak, J.A.; Gagen, P.M. Rates of reaction of galena, sphalerite, chalcopyrite, and arsenopyrite with Fe (III) in acidic solutions. In *Environmental Geochemistry of Sulfide Oxidation*; Alpers, C.N., Blowes, D.W., Eds.; American Chemical Society: Washington, DC, USA, 1994; pp. 2–13.

11. Corkhill, C.L. *The Mineralogical and Biogeochemical Transformations Associated with As-Bearing Sulphide Minerals in Acid Mine Drainage System*; The University of Manchester: Manchester, UK, 2008.

12. Koski, R.A.; Munk, L.; Foster, A.L.; Shanks, W.C.; Stillings, L.L. Sulfide oxidation and distribution of metals near abandoned copper mines in coastal environments, Prince William Sound, Alaska, USA. *Appl. Geochem.* **2008**, *23*, 227–254. [CrossRef]

13. Lizama, H.M.; Suzuki, I. Interaction of chalcopyrite and sphalerite with pyrite during leaching by Thiobacillus ferrooxidans and Thiobacillus thiooxidans. *Can. J. Microbiol.* **1991**, *37*, 304–311. [CrossRef]

14. Vera, M.; Schippers, A.; Sand, W. Progress in bioleaching: Fundamentals and mechanisms of bacterial metal sulfide oxidation-part A. *Appl. Microbiol. Biotechnol.* **2013**, *97*, 7529–7541. [CrossRef] [PubMed]

15. Ahonen, L.; Hiltunen, P.; Tuovinen, O. The role of pyrrhotite and pyrite in the bacterial leaching of chalcopyrite ores. In *Fundamental and Applied Biohydrometallurgy*; Lawrence, R.W., Branion, R.M.R., Ebner, H.G., Eds.; Elsevier: Amsterdam, The Netherlands, 1986; pp. 13–22.

16. Berry, V.K.; Murr, L.E.; Hiskey, J.B. Galvanic interaction between chalcopyrite and pyrite during bacterial leaching of low-grade waste. *Hydrometallurgy* **1978**, *3*, 309–326. [CrossRef]

17. Jyothi, N.; Sudha, K.N.; Natarajan, K.A. Electrochemical aspects of selective bioleaching of sphalerite and chalcopyrite from mixed sulphides. *Int. J. Miner. Process.* **1989**, *27*, 189–203. [CrossRef]

18. Mehta, A.P.; Murr, L.E. Kinetic study of sulfide leaching by galvanic interaction between chalcopyrite, pyrite, and sphalerite in the presence of *T. ferrooxidans* (30 °C) and a thermophilic microorganism (55 °C). *Biotechnol. Bioeng.* **1982**, *24*, 919–940. [CrossRef] [PubMed]

19. Natarajan, K.A.; Iwasaki, I. Role of Galvanic Interactions in the Bioleaching of Duluth Gabbro Copper-Nickel Sulfides. *Sep. Sci. Technol.* **1983**, *18*, 1095–1111. [CrossRef]

20. Meier, D.V.; Pjevac, P.; Bach, W.; Markert, S.; Schweder, T.; Jamieson, J.; Petersen, S.; Amann, R.; Meyerdierks, A. Microbial metal-sulfide oxidation in inactive hydrothermal vent chimneys suggested by metagenomic and metaproteomic analyses. *Environ. Microbiol.* **2019**. [CrossRef] [PubMed]

21. Wong, J.W.C.; Xiang, L.; Chan, L.C. pH Requirement for the Bioleaching of Heavy Metals from Anaerobically Digested Wastewater Sludge. *Water Air Soil Pollut.* **2002**, *138*, 25–35. [CrossRef]

22. Cui, X.; Wang, X.; Li, Y.; Lu, A.; Hao, R.; Wang, C.; Ding, H. Bioleaching of a Complex Co-Ni-Cu Sulfide Flotation Concentrate by *Bacillus megaterium* QM B1551 at Neutral pH. *Geomicrobiol. J.* **2016**, *33*, 734–741. [CrossRef]

23. McBeth, J.M.; Little, B.J.; Ray, R.I.; Farrar, K.M.; Emerson, D. Neutrophilic iron-oxidizing "Zetaproteobacteria" and mild steel corrosion in nearshore marine environments. *Appl. Environ. Microbiol.* **2011**, *77*, 1405–1412. [CrossRef] [PubMed]

24. Bilenker, L.D.; Romano, G.Y.; McKibben, M.A. Kinetics of sulfide mineral oxidation in seawater: Implications for acid generation during in situ mining of seafloor hydrothermal vent deposits. *Appl. Geochem.* **2016**, *75*, 20–31. [CrossRef]

25. Boschen, R.E.; Rowden, A.A.; Clark, M.R.; Pallentin, A.; Gardner, J.P.A. Seafloor massive sulfide deposits support unique megafaunal assemblages: Implications for seabed mining and conservation. *Mar. Environ. Res.* **2016**, *115*, 78–88. [CrossRef] [PubMed]

26. Boschen, R.E.; Rowden, A.A.; Clark, M.R.; Gardner, J.P.A. Mining of deep-sea seafloor massive sulfides: A review of the deposits, their benthic communities, impacts from mining, regulatory frameworks and management strategies. *Ocean Coast. Manag.* **2013**, *84*, 54–67. [CrossRef]

27. Van Dover, C.L. The biological environment of polymetallic sulphide deposits, the potential impact of exploration and mining on this environment and data required to establish environmental baselines in exploration areas. In *Polymetallic Sulphides and Cobalt-rich Ferromanganese Crusts Deposits: Establishment of Environmental Baselines and an Associated Monitoring Programme During Exploration*; International Seabed Authority: Kingston, Jamaica, 2007; pp. 169–190.

28. Van Dover, C.L. Mining seafloor massive sulphides and biodiversity: What is at risk? *ICES J. Mar. Sci.* **2010**, *68*, 341–348. [CrossRef]

29. Van Dover, C.L. Impacts of anthropogenic disturbances at deep-sea hydrothermal vent ecosystems: A review. *Mar. Environ. Res.* **2014**, *102*, 59–72. [CrossRef] [PubMed]

30. Collins, P.C.; Croot, P.; Carlsson, J.; Colaço, A.; Grehan, A.; Hyeong, K.; Kennedy, R.; Mohn, C.; Smith, S.; Yamamoto, H.; et al. A primer for the Environmental Impact Assessment of mining at seafloor massive sulfide deposits. *Mar. Policy* **2013**, *42*, 198–209. [CrossRef]

31. Newman, M.C.; McIntosh, A.W. *Metal Ecotoxicology: Concepts & Applications*; Lewis Publishers: Chelsea, MI, USA, 1991; ISBN 0873714113.

32. Simpson, S.L.; Spadaro, D.A. Bioavailability and Chronic Toxicity of Metal Sulfide Minerals to Benthic Marine Invertebrates: Implications for Deep Sea Exploration, Mining and Tailings Disposal. *Environ. Sci. Technol.* **2016**, *50*, 4061–4070. [CrossRef] [PubMed]

33. Edgcomb, V.P.; Molyneaux, S.J.; Saito, M.A.; Lloyd, K.; Boer, S.; Wirsen, C.O.; Atkins, M.S.; Teske, A. Sulfide Ameliorates Metal Toxicity for Deep-Sea Hydrothermal Vent Archaea. *Appl. Environ. Microbiol.* **2004**, *70*, 2551–2555. [CrossRef] [PubMed]

34. Koski, R. Metal Dispersion Resulting from Mining Activities in Coastal Environments: A Pathways Approach. *Oceanography* **2012**, *25*, 170–183. [CrossRef]

35. Hauton, C.; Brown, A.; Thatje, S.; Mestre, N.C.; Bebianno, M.J.; Martins, I.; Bettencourt, R.; Canals, M.; Sanchez-Vidal, A.; Shillito, B.; et al. Identifying Toxic Impacts of Metals Potentially Released during Deep-Sea Mining—A Synthesis of the Challenges to Quantifying Risk. *Front. Mar. Sci.* **2017**, *4*, 368. [CrossRef]

36. Llanos, J.; Capasso, C.; Parisi, E.; Prieur, D.; Jeanthon, C. Susceptibility to Heavy Metals and Cadmium Accumulation in Aerobic and Anaerobic Thermophilic Microorganisms Isolated from Deep-Sea Hydrothermal Vents. *Curr. Microbiol.* **2000**, *41*, 201–205. [CrossRef] [PubMed]

37. Vetriani, C.; Chew, Y.S.; Miller, S.M.; Yagi, J.; Coombs, J.; Lutz, R.A.; Barkay, T. Mercury adaptation among bacteria from a deep-sea hydrothermal vent. *Appl. Environ. Microbiol.* **2005**, *71*, 220–226. [CrossRef] [PubMed]

38. Ruelas-Inzunza, J.; Soto, L.A.; Páez-Osuna, F. Heavy-metal accumulation in the hydrothermal vent clam Vesicomya gigas from Guaymas basin, Gulf of California. *Deep Sea Res. Part I Oceanogr. Res. Pap.* **2003**, *50*, 757–761. [CrossRef]

39. Kádár, E.; Costa, V.; Santos, R.S.; Powell, J.J. Tissue partitioning of micro-essential metals in the vent bivalve Bathymodiolus azoricus and associated organisms (endosymbiont bacteria and a parasite polychaete) from geochemically distinct vents of the Mid-Atlantic Ridge. *J. Sea Res.* **2006**, *56*, 45–52. [CrossRef]

40. Wang, C.L.; Michels, P.C.; Dawson, S.C.; Kitisakkul, S.; Baross, J.A.; Keasling, J.D.; Clark, D.S. Cadmium removal by a new strain of Pseudomonas aeruginosa in aerobic culture. *Appl. Environ. Microbiol.* **1997**, *63*, 4075–4078. [PubMed]

41. Auguste, M.; Mestre, N.C.; Rocha, T.L.; Cardoso, C.; Cueff-Gauchard, V.; Le Bloa, S.; Cambon-Bonavita, M.A.; Shillito, B.; Zbinden, M.; Ravaux, J.; et al. Development of an ecotoxicological protocol for the deep-sea fauna using the hydrothermal vent shrimp Rimicaris exoculata. *Aquat. Toxicol.* **2016**, *175*, 277–285. [CrossRef] [PubMed]

42. Martins, I.; Goulart, J.; Martins, E.; Morales-Román, R.; Marín, S.; Riou, V.; Colaço, A.; Bettencourt, R. Physiological impacts of acute Cu exposure on deep-sea vent mussel Bathymodiolus azoricus under a deep-sea mining activity scenario. *Aquat. Toxicol.* **2017**, *193*, 40–49. [CrossRef] [PubMed]

43. Mestre, N.C.; Rocha, T.L.; Canals, M.; Cardoso, C.; Danovaro, R.; Dell'Anno, A.; Gambi, C.; Regoli, F.; Sanchez-Vidal, A.; Bebianno, M.J. Environmental hazard assessment of a marine mine tailings deposit site and potential implications for deep-sea mining. *Environ. Pollut.* **2017**, *228*, 169–178. [CrossRef] [PubMed]

44. Brown, A.; Thatje, S.; Hauton, C. The Effects of Temperature and Hydrostatic Pressure on Metal Toxicity: Insights into Toxicity in the Deep Sea. *Environ. Sci. Technol.* **2017**, *51*, 10222–10231. [CrossRef] [PubMed]

45. Luther, G.W.; Rickard, D.T.; Theberge, S.; Olroyd, A. Determination of Metal (Bi)Sulfide Stability Constants of Mn^{2+}, Fe^{2+}, Co^{2+}, Ni^{2+}, Cu^{2+}, and Zn^{2+} by Voltammetric Methods. *Environ. Sci. Technol.* **1996**, *30*, 671–679. [CrossRef]

46. Metz, S.; Trefry, J.H. Chemical and mineralogical influences on concentrations of trace metals in hydrothermal fluids. *Geochim. Cosmochim. Acta* **2000**, *13*, 2267–2279. [CrossRef]

47. Brown, A.; Wright, R.; Mevenkamp, L.; Hauton, C. A comparative experimental approach to ecotoxicology in shallow-water and deep-sea holothurians suggests similar behavioural responses. *Aquat. Toxicol.* **2017**, *191*, 10–16. [CrossRef] [PubMed]

48. Jou, L.-J.; Chen, B.-C.; Chen, W.-Y.; Liao, C.-M. Sensory determinants of valve rhythm dynamics provide in situ biodetection of copper in aquatic environments. *Environ. Sci. Pollut. Res.* **2016**, *23*, 5374–5389. [CrossRef] [PubMed]

49. Mevenkamp, L.; Brown, A.; Hauton, C.; Kordas, A.; Thatje, S.; Vanreusel, A. Hydrostatic pressure and temperature affect the tolerance of the free-living marine nematode Halomonhystera disjuncta to acute copper exposure. *Aquat. Toxicol.* **2017**, *192*, 178–183. [CrossRef] [PubMed]

50. Koschinsky, A.; Borowski, C.; Halbach, P. Reactions of the Heavy Metal Cycle to Industrial Activities in the Deep Sea: An Ecological Assessment. *Int. Rev. Hydrobiol.* **2003**, *88*, 102–127. [CrossRef]

51. Petersen, S.; Krätschell, A.; Augustin, N.; Jamieson, J.; Hein, J.R.; Hannington, M.D. News from the seabed-Geological characteristics and resource potential of deep-sea mineral resources. *Mar. Policy* **2016**, *70*, 175–187. [CrossRef]

52. GESAMP. Proceeding of the GESAMP International Workshop on the Impacts of Mine Tailings in the Marine Environment (IMO/FAO/UNESCO-IOC/UNIDO/WMO/IAEA/UN/UNEP/UNDP Joint Group of Experts on the Scientific Aspects of Marine Environmental Protection). *Rep. Stud. GESAMP* **2016**, *94*, 84.

53. Dold, B. Bernhard Submarine Tailings Disposal (STD)—A Review. *Minerals* **2014**, *4*, 642–666. [CrossRef]

54. Lindsay, M.B.J.; Moncur, M.C.; Bain, J.G.; Jambor, J.L.; Ptacek, C.J.; Blowes, D.W. Geochemical and mineralogical aspects of sulfide mine tailings. *Appl. Geochem.* **2015**, *57*, 157–177. [CrossRef]

55. Vare, L.L.; Baker, M.C.; Howe, J.A.; Levin, L.A.; Neira, C.; Ramirez-Llodra, E.Z.; Reichelt-Brushett, A.; Rowden, A.A.; Shimmield, T.M.; Simpson, S.L.; et al. Scientific Considerations for the Assessment and Management of Mine Tailings Disposal in the Deep Sea. *Front. Mar. Sci.* **2018**, *5*, 17. [CrossRef]

56. Josefson, A.B.; Hansen, J.L.S.; Asmund, G.; Johansen, P. Threshold response of benthic macrofauna integrity to metal contamination in West Greenland. *Mar. Pollut. Bull.* **2008**, *56*, 1265–1274. [CrossRef] [PubMed]

57. Elberling, B.; Asmund, G.; Kunzendorf, H.; Krogstad, E.J. Geochemical trends in metal-contaminated fiord sediments near a former lead–zinc mine in West Greenland. *Appl. Geochem.* **2002**, *17*, 493–502. [CrossRef]

58. Perner, K.; Leipe, T.; Dellwig, O.; Kuijpers, A.; Mikkelsen, N.; Andersen, T.J.; Harff, J. Contamination of arctic Fjord sediments by Pb–Zn mining at Maarmorilik in central West Greenland. *Mar. Pollut. Bull.* **2010**, *60*, 1065–1073. [CrossRef] [PubMed]

59. Andrade, S.; Moffett, J.; Correa, J.A. Distribution of dissolved species and suspended particulate copper in an intertidal ecosystem affected by copper mine tailings in Northern Chile. *Mar. Chem.* **2006**, *101*, 203–212. [CrossRef]

60. Lee, M.R.; Correa, J.A.; Zhang, H. Effective metal concentrations in porewater and seawater labile metal concentrations associated with copper mine tailings disposal into the coastal waters of the Atacama region of northern Chile. *Mar. Pollut. Bull.* **2002**, *44*, 956–961. [CrossRef]

61. Sanders, J.G.; Riedel, G.F.; Osman, R.W. Arsenic cycling and its impact in estuarine and coastal marine ecosystems. In *Arsenic in the Environment. Part 1: Cycling and Characterisation*; Nriagu, J.O., Ed.; John Wiley & Sons, Inc.: New York, NY, USA, 1994; pp. 289–308.

62. Price, R.E.; Pichler, T. Distribution, speciation and bioavailability of arsenic in a shallow-water submarine hydrothermal system, Tutum Bay, Ambitle Island, PNG. *Chem. Geol.* **2005**, *224*, 122–135. [CrossRef]

63. Hannington, M.D.; de Ronde, C.E.J.; Petersen, S. Modern seafloor tectonics and submarine hydrothermal systems. *Econ. Geol. One Hundredth Anniv. Vol.* **2005**, *100*, 111–141.

64. German, C.R.; Petersen, S.; Hannington, M.D. Hydrothermal exploration of mid-ocean ridges: Where might the largest sulfide deposits be forming? *Chem. Geol.* **2016**, *420*, 114–126. [CrossRef]

65. Hannington, M.; Jamieson, J. Estimating the metal content of SMS deposits. In Proceedings of the Oceans'11 MTS/IEEE Kona, Waikoloa, HI, USA, 19–22 September 2011.

66. Monecke, T.; Petersen, S.; Hannington, M.D.; Grant, H.; Samson, I. The minor element endowment of modern sea-floor massive sulfide deposits and comparison with deposits hosted in ancient volcanic successions. *Rev. Econ. Geol.* **2016**, *18*, 245–306.

67. Hannington, M.D.; Jamieson, J.; Monecke, T.; Petersen, S. Modern Sea-Floor Massive Sulfides and Base Metal Resources: Toward an Estimate of Global Sea-Floor Massive Sulfide Potential. *Soc. Econ. Geol. Spec. Publ. 15* **2010**, *15*, 317–338.

68. Stoffers, P.; Hannington, M.; Wright, I.; Herzig, P.; Ronde, C. de Elemental mercury at submarine hydrothermal vents in the Bay of Plenty, Taupo volcanic zone, New Zealand. *Geology* **1999**, *27*, 931–934. [CrossRef]

69. Abraitis, P.; Pattrick, R.A.D.; Vaughan, D.J. Variations in the compositional, textural and electrical properties of natural pyrite: A review. *Int. J. Miner. Process.* **2004**, *74*, 41–59. [CrossRef]

70. Chen, J.; Wang, L.; Chen, Y.; Guo, J. A DFT study of the effect of natural impurities on the electronic structure of galena. *Int. J. Miner. Process.* **2011**, *98*, 132–136. [CrossRef]

71. Chen, Y.; Chen, J.; Guo, J. A DFT study on the effect of lattice impurities on the electronic structures and floatability of sphalerite. *Miner. Eng.* **2010**, *23*, 1120–1130. [CrossRef]

72. Lehner, S.; Savage, K.; Ciobanu, M.; Cliffel, D.E. The effect of As, Co, and Ni impurities on pyrite oxidation kinetics: An electrochemical study of synthetic pyrite. *Geochim. Cosmochim. Acta* **2007**, *71*, 2491–2509. [CrossRef]

73. Liu, R.; Wolfe, A.L.; Dzombak, D.A.; Stewart, B.W.; Capo, R.C. Comparison of dissolution under oxic acid drainage conditions for eight sedimentary and hydrothermal pyrite samples. *Environ. Geol.* **2007**, *56*, 171–182. [CrossRef]

74. Wei, D. Semiconductor Electrochemistry of Particulate Pyrite: Dissolution via Hole and Electron Pathways. *J. Electrochem. Soc.* **1996**, *143*, 3192. [CrossRef]

75. Jamieson, H.E.; Walker, S.R.; Parsons, M.B. Mineralogical characterization of mine waste. *Appl. Geochem.* **2015**, *57*, 85–105. [CrossRef]

76. Fallon, E.K.; Petersen, S.; Brooker, R.A.; Scott, T.B. Oxidative dissolution of hydrothermal mixed-sulphide ore: An assessment of current knowledge in relation to seafloor massive sulphide mining. *Ore Geol. Rev.* **2017**, *86*, 309–337. [CrossRef]

77. Wohlgemuth-Ueberwasser, C.C.; Viljoen, F.; Petersen, S.; Vorster, C. Distribution and solubility limits of trace elements in hydrothermal black smoker sulfides: An in-situ LA-ICP-MS study. *Geochim. Cosmochim. Acta* **2015**, *159*, 16–41. [CrossRef]

78. Butler, I.B.; Nesbitt, R.W. Trace element distributions in the chalcopyrite wall of a black smoker chimney: Insights from laser ablation inductively coupled plasma mass spectrometry (LA–ICP–MS). *Earth Planet. Sci. Lett.* **1999**, *167*, 335–345. [CrossRef]

79. Cook, N.J.; Ciobanu, C.L.; Pring, A.; Skinner, W.; Shimizu, M.; Danyushevsky, L.; Saini-Eidukat, B.; Melcher, F. Trace and minor elements in sphalerite: A LA-ICPMS study. *Geochim. Cosmochim. Acta* **2009**, *73*, 4761–4791. [CrossRef]

80. Ye, L.; Cook, N.J.; Ciobanu, C.L.; Yuping, L.; Qian, Z.; Tiegeng, L.; Wei, G.; Yulong, Y.; Danyushevskiy, L. Trace and minor elements in sphalerite from base metal deposits in South China: A LA-ICPMS study. *Ore Geol. Rev.* **2011**, *39*, 188–217. [CrossRef]

81. Petersen, S.; Herzig, P.M.; Hannington, M.D. Third dimension of a presently forming VMS deposit: TAG hydrothermal mound, Mid-Atlantic Ridge, 26°N. *Miner. Depos.* **2000**, *35*, 233–259. [CrossRef]

82. Haase, K.M.; Petersen, S.; Koschinsky, A.; Seifert, R.; Devey, C.W.; Keir, R.; Lackschewitz, K.S.; Melchert, B.; Perner, M.; Schmale, O.; et al. Young volcanism and related hydrothermal activity at 5°S on the slow-spreading southern Mid-Atlantic Ridge. *Geochem. Geophys. Geosyst.* **2007**, *8*. [CrossRef]

83. Petersen, S.; Kuhn, K.; Kuhn, T.; Augustin, N.; Hékinian, R.; Franz, L.; Borowski, C. The geological setting of the ultramafic-hosted Logatchev hydrothermal field (14°45′N, Mid-Atlantic Ridge) and its influence on massive sulfide formation. *Lithos* **2009**, *112*, 40–56. [CrossRef]

84. Petersen, S.; Monecke, T.; Westhues, A.; Hannington, M.D.; Gemmell, J.B.; Sharpe, R.; Peters, M.; Strauss, H.; Lackschewitz, K.; Augustin, N.; et al. Drilling Shallow-Water Massive Sulfides at the Palinuro Volcanic Complex, Aeolian Island Arc, Italy. *Econ. Geol.* **2014**, *109*, 2129–2158. [CrossRef]

85. Yang, K.; Scott, S.D. Possible contribution of a metal-rich magmatic fluid to a sea-floor hydrothermal system. *Nature* **1996**, *383*, 420–423. [CrossRef]

86. Binns, R.A. *Data Report: Geochemistry of Massive and Semimassive Sulphides from Site 1189, Ocean Drilling Program Leg 193*; Barriga, F.J.A.S., Binns, R.A., Miller, D.J., Herzig, P.M., Eds.; Texas A&M University: College Station, TX, USA, 2006; pp. 1–22.

87. Beaulieu, S.E.; Baker, E.T.; German, C.R.; Maffei, A. An authoritative global database for active submarine hydrothermal vent fields. *Geochem. Geophys. Geosyst.* **2013**, *14*, 4892–4905. [CrossRef]

88. Fietzke, J.; Frische, M. Experimental evaluation of elemental behavior during LA-ICP-MS: Influences of plasma conditions and limits of plasma robustness. *J. Anal. At. Spectrom.* **2016**, *31*, 234–244. [CrossRef]

89. Barakat, M.A. New trends in removing heavy metals from industrial wastewater. *Arab. J. Chem.* **2011**, *4*, 361–377. [CrossRef]

90. Kearns, J.; Turner, A. An evaluation of the toxicity and bioaccumulation of bismuth in the coastal environment using three species of macroalga. *Environ. Pollut.* **2016**, *208*, 435–441. [CrossRef] [PubMed]

91. Jeanthon, C.; Prieur, D. Resistance to heavy metals of heterotrophic bacteria isolated from the deep-sea hydrothermal vent polychaete, Alvinella pompejana. *Prog. Oceanogr.* **1990**, *24*, 81–88. [CrossRef]

92. Luoma, S.N.; Ho, Y.B.; Bryan, G.W. Fate, bioavailability and toxicity of silver in estuarine environments. *Mar. Pollut. Bull.* **1995**, *31*, 44–54. [CrossRef]

93. Hogstrand, C.; Wood, C.M. Toward a better understanding of the bioavailability, physiology, and toxicity of silver in fish: Implications for water quality criteria. *Environ. Toxicol. Chem.* **1998**, *17*, 547–561. [CrossRef]

94. Barriada, J.L.; Tappin, A.D.; Evans, E.H.; Achterberg, E.P. Dissolved silver measurements in seawater. *TrAC Trends Anal. Chem.* **2007**, *26*, 809–817. [CrossRef]

95. Wohlgemuth-Ueberwasser, C.C.; Viljoen, F.; McClung, C.R. Metamorphic alteration of the massive sulfide horizon from the Salt River VMS deposit (South Africa). *Ore Geol. Rev.* **2014**, *56*, 45–52. [CrossRef]

96. Jochum, K.P.; Stoll, B.; Herwig, K.; Willbold, M.; Hofmann, A.W.; Amini, M.; Aarburg, S.; Abouchami, W.; Hellebrand, E.; Mocek, B.; et al. MPI-DING reference glasses for in situ microanalysis: New reference values for element concentrations and isotope ratios. *Geochem. Geophys. Geosyst.* **2006**, *7*. [CrossRef]

97. George, L.L.; Cook, N.J.; Ciobanu, C.L. Partitioning of trace elements in co-crystallized sphalerite–galena–chalcopyrite hydrothermal ores. *Ore Geol. Rev.* **2016**, *77*, 97–116. [CrossRef]

98. George, L.; Cook, N.; Ciobanu, C. Minor and Trace Elements in Natural Tetrahedrite-Tennantite: Effects on Element Partitioning among Base Metal Sulphides. *Minerals* **2017**, *7*, 17. [CrossRef]

99. Humphris, S.E.; Herzig, P.M.; Miller, J. *Ocean Drilling Program: Leg 158 Preliminary Report, TAG: Drilling an Active Hydrothermal System on a Sediment-Free Slow-Spreading Ridge*; Texas A&M University: College Station, TX, USA, 1994.

100. Haase, K. *Cruise Report M064/1—MARSUED II*; Leitstelle Meteor: Hamburg, Germany, 2005.

101. Kuhn, T. *Cruise Report M060/3—HYDROMAR I—Mineralogical, Geochemical, and Biological Investigations of Hydrothermal Systems on the Mid-Atlantic Ridge between 14°45′N and 15°05′N (No. 03-04)*; Leitstelle Meteor: Hamburg, Germany, 2004.

102. Herzig, P.; Suess, E.; Linke, P. *RV Sonne Cruise Report SO109 Hydrotrace*; GEOMAR Report 58; GEOMAR: Kiel, Germany, 1997.

103. Marchig, V. *Cruise Report: SO 62: GEOMETEP 5 04.04.1989-03.07*; Bundesanstalt für Geowissenschaften und Rohstoffe: Hannover, Germany, 1989.

104. Herzig, P.; Kuhn, T.; Petersen, S. *Detailed Investigation of the Magmatic-Hydrothermal Gold Mineralisation at Conical Seamount (New Ireland Basin) and of Massive Sulphides at PACMANUS (Eastern Manus Basin)*; Papua New Guinea by shallow drilling: Cruise Report: SO-166 CONDRILL; Freiberg University of Mining and Technology: Freiberg, Germany, 2003.

105. Bach, W.; Dubilier, N.; Borowski, C.; Breuer, C.; Brumner, B.; Franke, P.; Herschelmann, O.; Hourdez, S.; Jonda, L.; Jons, N.; et al. *Report and Preliminary Results of RV SONNE Cruise SO 216, Townsville (Australia)-Makassar (Indonesia), June 14–July 23, 2011. BAMBUS, Back-Arc Manus Basin Underwater Solfataras*; University of Bremen: Bremen, Germany, 2011.

106. Petersen, S.; Monecke, T. *Cruise Report M073/2—Shallow Drilling of Hydrothermal Sites in the Tyrrhenian Sea (Palindrill) (No. 30)*; IFM-GEOMAR: Kiel, Germany, 2009.

107. Humphris, S.E.; Herzig, P.M.; Miller, D.J.; Alt, J.C.; Becker, K.; Brown, D.; Brügmann, G.; Chiba, H.; Fouquet, Y.; Gemmell, J.B.; et al. The internal structure of an active sea-floor massive sulphide deposit. *Nature* **1995**, *377*, 713–716. [CrossRef]

108. Hannington, M.D.; Jonasson, I.R.; Herzig, P.M.; Petersen, S. Physical and chemical processes of seafloor mineralization at mid-ocean ridges. In *Seafloor Hydrothermal Systems: Physical, Chemical, Biological, and Geological Interactions*; American Geophysical Union: Washington DC, USA, 1995; pp. 115–157. ISBN 9781118663998.

109. Petersen, S.; Herzig, P.M.; Schwarz-Schampera, U.; Hannington, M.D.; Jonasson, I.R. Hydrothermal precipitates associated with bimodal volcanism in the Central Bransfield Strait, Antarctica. *Miner. Depos.* **2004**, *39*, 358–379. [CrossRef]

110. Monecke, T.; Petersen, S.; Hannington, M.M.D. Constraints on Water Depth of Massive Sulfide Formation: Evidence from Modern Seafloor Hydrothermal Systems in Arc-Related Settings. *Econ. Geol.* **2014**, *109*, 2079–2101. [CrossRef]

111. Fouquet, Y.; Cambon, P.; Etoubleau, J.; Charlou, J.L.; Ondréas, H.; Barriga, F.J.A.S.; Cherkashov, G.; Semkova, T.; Poroshina, I.; Bohn, M.; et al. Geodiversity of Hydrothermal Processes Along the Mid-Atlantic Ridge and Ultramafic-Hosted Mineralization: A New Type of Oceanic Cu-Zn-Co-Au Volcanogenic Massive Sulfide Deposit. *Divers. Hydrotherm. Syst. Slow Spread. Ocean Ridges* **2010**, *188*, 321–367.

112. Binns, R.A.; Barriga, F.J.A.S.; Miller, J. *Proceedings of the Ocean Drilling Program*; Initial Reports; Anatomy of an Active Felsic-Hosted Hydrothermal System, Eastern Manus Basin, 193; Texas A&M University: College Station, TX, USA, 2002.

113. Fouquet, Y.; Wafik, A.; Cambon, P.; Mevel, C.; Meyer, G.; Gente, P. Tectonic setting and mineralogical and geochemical zonation in the Snake Pit sulfide deposit (Mid-Atlantic Ridge at 23°N). *Econ. Geol.* **1993**, *88*, 2018–2036. [CrossRef]

114. Marques, A.F.A.; Barriga, F.; Chavagnac, V.; Fouquet, Y. Mineralogy, geochemistry, and Nd isotope composition of the Rainbow hydrothermal field, Mid-Atlantic Ridge. *Miner. Depos.* **2006**, *41*, 52–67. [CrossRef]

115. Wang, Y.; Han, X.; Petersen, S.; Jin, X.; Qiu, Z.; Zhu, J. Mineralogy and geochemistry of hydrothermal precipitates from Kairei hydrothermal field, Central Indian Ridge. *Mar. Geol.* **2014**, *354*, 69–80. [CrossRef]

116. Libbey, R.B.; Williams-Jones, A.E. Relating sulfide mineral zonation and trace element chemistry to subsurface processes in the Reykjanes geothermal system, Iceland. *J. Volcanol. Geotherm. Res.* **2016**, *310*, 225–241. [CrossRef]

117. Migdisov, A.A.; Zezin, D.; Williams-Jones, A.E. An experimental study of Cobalt (II) complexation in Cl^- and H_2S-bearing hydrothermal solutions. *Geochim. Cosmochim. Acta* **2011**, *75*, 4065–4079. [CrossRef]

118. Mozgova, N.N.; Efimov, A.; Borodaev, Y.S.; Krasnov, S.G.; Cherkashov, G.A.; Stepanova, T.V.; Ashadze, A.M. Mineralogy and chemistry of massive sulfides from the Logatchev hydrothermal field (14 degrees 45'N Mid-Atlantic Ridge). *Explor. Min. Geol.* **1999**, *8*, 379–395.

119. Marques, A.F.A.; Barriga, F.J.A.S.; Scott, S.D. Sulfide mineralization in an ultramafic-rock hosted seafloor hydrothermal system: From serpentinization to the formation of Cu–Zn–(Co)-rich massive sulfides. *Mar. Geol.* **2007**, *245*, 20–39. [CrossRef]

120. Lein, A.Y.; Bogdanov, Y.A.; Maslennikov, V.V.; Li, S.; Ulyanova, N.V.; Maslennikova, S.P.; Ulyanov, A.A. Sulfide minerals in the Menez Gwen nonmetallic hydrothermal field (Mid-Atlantic Ridge). *Lithol. Miner. Resour.* **2010**, *45*, 305–323. [CrossRef]

121. Hannington, M.; Galley, A. Comparison of the TAG Mound and Stockwork Complex with Cyprus-Type Massive Sulfide Deposits. *Proc. Ocean Drill. Program. Sci. Results* **1998**, *158*.

122. Hannington, M.; Herzig, P.; Scott, S.; Thompson, G.; Rona, P.A. Comparative mineralogy and geochemistry of gold-bearing sulfide deposits on the mid-ocean ridges. *Mar. Geol.* **1991**, *101*, 217–248. [CrossRef]

123. Butterfield, D.; Massoth, G.; McDuff, R.; Lupton, J. Geochemistry of hydrothermal fluids from Ashes Vent Field, Axial Seamount, Juan de Fuca Ridge: Subseafloor boiling and subsequent fluid-rock. *J. Geophys. Res* **1990**, *95*, 12895–12921. [CrossRef]

124. Chiba, H.; Masuda, H.; Lee, S.-Y.; Fujioka, K. Chemistry of hydrothermal fluids at the TAG Active Mound, MAR 26°N, in 1998. *Geophys. Res. Lett.* **2001**, *28*, 2919–2922. [CrossRef]

125. Reeves, E.P.; Seewald, J.S.; Saccocia, P.; Bach, W.; Craddock, P.R.; Shanks, W.C.; Sylva, S.P.; Walsh, E.; Pichler, T.; Rosner, M. Geochemistry of hydrothermal fluids from the PACMANUS, Northeast Pual and Vienna Woods hydrothermal fields, Manus Basin, Papua New Guinea. *Geochim. Cosmochim. Acta* **2011**, *75*, 1088–1123. [CrossRef]

126. Klevenz, V.; Bach, W.; Schmidt, K.; Hentscher, M.; Koschinsky, A.; Petersen, S. Geochemistry of vent fluid particles formed during initial hydrothermal fluid-seawater mixing along the Mid-Atlantic Ridge. *Geochem. Geophys. Geosyst.* **2011**, *12*. [CrossRef]

127. Schwartz, M.O. Cadmium in Zinc Deposits: Economic Geology of a Polluting Element. *Int. Geol. Rev.* **2000**, *42*, 445–469. [CrossRef]

128. Binns, R.A.; Scott, S.D. Actively forming polymetallic sulfide deposits associated with felsic volcanic rocks in the eastern Manus back-arc basin, Papua New Guinea. *Econ. Geol.* **1993**, *88*, 2226–2236. [CrossRef]

129. Keith, M.; Haase, K.M.; Schwarz-Schampera, U.; Klemd, R.; Petersen, S.; Bach, W. Effects of temperature, sulfur, and oxygen fugacity on the composition of sphalerite from submarine hydrothermal vents. *Geology* **2014**, *42*, 699–702. [CrossRef]

130. Spycher, N.F.; Reed, M.H. Evolution of a broadlands-type epithermal ore fluid along alternative P-T paths; implications for the transport and deposition of base, precious, and volatile metals. *Econ. Geol.* **1989**, *84*, 328–359. [CrossRef]

131. Spycher, N.F.; Reed, M.H. As (III) and Sb(III) sulfide complexes: An evaluation of stoichiometry and stability from existing experimental data. *Geochim. Cosmochim. Acta* **1989**, *53*, 2185–2194. [CrossRef]

132. Obolensky, A.A.; Gushchina, L.V.; Borisenko, A.S.; Borovikov, A.A.; Pavlova, G.G. Antimony in hydrothermal processes: Solubility, conditions of transfer, and metal-bearing capacity of solutions. *Russ. Geol. Geophys.* **2007**, *48*, 992–1001. [CrossRef]

133. Stauffer, R.E.; Thompson, J.M. Arsenic and antimony in geothermal waters of Yellowstone National Park, Wyoming, USA. *Geochim. Cosmochim. Acta* **1984**, *48*, 2547–2561. [CrossRef]

134. Kremheller, A.; Levine, A.K.; Gashurov, G. Hydrothermal preparation of two-component solid solutions from II–VI compounds. *J. Electrochem. Soc.* **1960**, *107*, 12. [CrossRef]

135. Chen, J.; Chen, Y. A first-principle study of the effect of vacancy defects and impurities on the adsorption of O_2 on sphalerite surfaces. *Colloid. Surf. A Physicochem. Eng. Asp.* **2010**, *363*, 56–63. [CrossRef]

136. Perez, I.P.; Dutrizac, J. The effect of the iron content of sphalerite on its rate of dissolution in ferric sulphate and ferric chloride media. *Hydrometallurgy* **1991**, *26*, 211–232. [CrossRef]

137. Weisener, C.G.; Smart, R.S.C.; Gerson, A.R. A comparison of the kinetics and mechanism of acid leaching of sphalerite containing low and high concentrations of iron. *Int. J. Miner. Process.* **2004**, *74*, 239–249. [CrossRef]

138. Fouquet, Y.; Auclair, G.; Cambon, P.; Etoubleau, J. Geological setting and mineralogical and geochemical investigations on sulfide deposits near 13°N on the East Pacific Rise. *Mar. Geol.* **1988**, *84*, 145–178. [CrossRef]

139. Wohlgemuth-Ueberwasser, C. Analysis of As and Sb in samples from Turtle Pits hydrothermal field using new standard material. *Mineral. Mag.* **2011**, *75*, 2169.

140. Iwaida, C.; Ueno, H. Ore and gangue minerals of seafloor hydrothermal deposits in the Mariana trough. *JAMSTEC Rep. Res. Dev.* **2005**, *1*, 1–12.

141. Suzuki, R.; Ishibashi, J.-I.; Nakaseama, M.; Konno, U.; Tsunogai, U.; Gena, K.; Chiba, H. Diverse Range of Mineralization Induced by Phase Separation of Hydrothermal Fluid: Case Study of the Yonaguni Knoll IV Hydrothermal Field in the Okinawa Trough Back-Arc Basin. *Resour. Geol.* **2008**, *58*, 267–288. [CrossRef]

142. Ueno, H.; Hamasaki, H.; Murakawa, Y.; Kitazono, S.; Takeda, T. Ore and gangue minerals of sulfide chimneys from the North Knoll. *JAMSTEC J. Deep Sea Res.* **2003**, *22*, 19–62.

143. Tivey, M.K.; Stakes, D.S.; Cook, T.L.; Hannington, M.D.; Petersen, S. A model for growth of steep-sided vent structures on the Endeavour Segment of the Juan de Fuca Ridge: Results of a petrologic and geochemical study. *J. Geophys. Res. Solid Earth* **1999**, *104*, 22859–22883. [CrossRef]

144. Chetty, R.; Bali, A.; Mallik, R.C. Tetrahedrites as thermoelectric materials: An overview. *J. Mater. Chem. C* **2015**, *3*, 12364–12378. [CrossRef]

145. Halbach, P.; Pracejus, B.; Maerten, A. Geology and mineralogy of massive sulfide ores from the central Okinawa Trough, Japan. *Econ. Geol.* **1993**, *88*, 2210–2225. [CrossRef]

146. Herzig, P.M.; Hannington, M.D. Polymetallic massive sulphides at the modern seafloor: A review. *Ore Geol. Rev.* **1995**, *10*, 95–115. [CrossRef]

147. Paradis, S.; Jonasson, I.R.; Le Cheminant, G.M.; Watkinson, D.H. Two zinc-rich chimneys from the plume site, Southern Juan de Fuca Ridge. *Can. Mineral.* **1988**, *26*, 637–654.

148. Halbach, P.; Blum, N.; Münch, U.; Plüger, W.; Garbe-Schönberg, D.; Zimmer, M. Formation and decay of a modern massive sulfide deposit in the Indian Ocean. *Miner. Depos.* **1998**, *33*, 302–309. [CrossRef]

149. Wang, Y.; Han, X.; Petersen, S.; Frische, M.; Qiu, Z.; Li, H.; Li, H.; Wu, Z.; Cui, R. Mineralogy and trace element geochemistry of sulfide minerals from the Wocan Hydrothermal Field on the slow-spreading Carlsberg Ridge, Indian Ocean. *Ore Geol. Rev.* **2017**, *84*, 1–19. [CrossRef]

150. Hannington, M.D.; Thompson, G.; Rona, P.A.; Scott, S.D. Gold and native copper in supergene sulphides from the Mid-Atlantic Ridge. *Nature* **1988**, *333*, 64–66. [CrossRef]

151. Herzig, P.M.; Hannington, M.D.; Scott, S.D.; Maliotis, G.; Rona, P.A.; Thompson, G. Gold-rich sea-floor gossans in the Troodos Ophiolite and on the Mid-Atlantic Ridge. *Econ. Geol.* **1991**, *86*, 1747–1755. [CrossRef]

152. Grant, H.L.J.; Hannington, M.D.; Petersen, S.; Frische, M.; Fuchs, S.H. Constraints on the behavior of trace elements in the actively-forming TAG deposit, Mid-Atlantic Ridge, based on LA-ICP-MS analyses of pyrite. *Chem. Geol.* **2018**, *498*, 45–71. [CrossRef]

153. Goh, S.W.; Buckley, A.N.; Lamb, R.N.; Rosenberg, R.A.; Moran, D. The oxidation states of copper and iron in mineral sulfides, and the oxides formed on initial exposure of chalcopyrite and bornite to air. *Geochim. Cosmochim. Acta* **2006**, *70*, 2210–2228. [CrossRef]

154. Chouinard, A.; Paquette, J.; Williams-Jones, A.E. Crystallographic controls on trace-element incorporation in Auriferous pyrite from the Pascua epithermal high-sulfidation deposit, Chile-Argentina. *Can. Mineral.* **2005**, *43*, 951–963. [CrossRef]

155. Archibald, S.M.; Migdisov, A.A.; Williams-Jones, A.E. An experimental study of the stability of copper chloride complexes in water vapor at elevated temperatures and pressures. *Geochim. Cosmochim. Acta* **2002**, *66*, 1611–1619. [CrossRef]

156. Blanchard, M.; Wright, K.; Richard, C.; Catlow, A. Arsenic incorporation into FeS_2 pyrite and its influence on dissolution: A DFT study. *Geochim. Cosmochim. Acta* **2006**, *71*, 624–630. [CrossRef]

157. Koschinsky, A.; Garbe-Schönberg, D.; Sander, S.; Schmidt, K.; Gennerich, H.-H.; Strauss, H. Hydrothermal venting at pressure-temperature conditions above the critical point of seawater, 5°S on the Mid-Atlantic Ridge. *Geology* **2008**, *36*, 615–618. [CrossRef]

158. Savage, K.S.; Stefan, D.; Lehner, S.W. Impurities and heterogeneity in pyrite: Influences on electrical properties and oxidation products. *Appl. Geochemistry* **2008**, *23*, 103–120. [CrossRef]

159. Rona, P.A.; Bogdanov, Y.A.; Gurvich, E.G.; Rimski-Korsakov, N.A.; Sagalevitch, A.M.; Hannington, M.D.; Thompson, G. Relict hydrothermal zones in the TAG Hydrothermal Field, Mid-Atlantic Ridge 26°N, 45°W. *J. Geophys. Res.* **1993**, *98*, 9715. [CrossRef]

160. Bilenker, L. *Abiotic Oxidation Rate of Chalcopyrite in Seawater: Implications for Seafloor Mining*; University of California, Riverside: Riverside, CA, USA, 2011.

161. Feely, R.A.; Lewison, M.; Massoth, G.J.; Robert-Baldo, G.; Lavelle, J.W.; Byrne, R.H.; Von Damm, K.L.; Curl, H.C. Composition and dissolution of black smoker particulates from active vents on the Juan de Fuca Ridge. *J. Geophys. Res.* **1987**, *92*, 11347–11363. [CrossRef]

162. Morse, J.W. Oxidation kinetics of sedimentary pyrite in seawater. *Geochim. Cosmochim. Acta* **1991**, *55*, 3665–3667. [CrossRef]

163. Romano, G.Y. *Kinetics of Pyrrhotite Oxidation in Seawater: Implications for Mining Seafloor Hotsprings*; University of California, Riverside: Riverside, CA, USA, 2012.

164. Embile, R.F.; Walder, I. Galena Non-oxidative Dissolution Kinetics in Seawater. *Aquat. Geochem.* **2018**, *24*, 107–119. [CrossRef]

165. Abraitis, P.; Pattrick, R.A.D.; Kelsall, G.H.; Vaughan, D.J. Acid leaching and dissolution of major sulphide ore minerals: Processes and galvanic effects in complex systems. *Mineral. Mag.* **2004**, *68*, 343–351. [CrossRef]

166. Heidel, C.; Tichomirowa, M.; Junghans, M. Oxygen and sulfur isotope investigations of the oxidation of sulfide mixtures containing pyrite, galena, and sphalerite. *Chem. Geol.* **2013**, *342*, 29–43. [CrossRef]

167. Kwong, Y.T.J.; Swerhone, G.W.; Lawrence, J.R. Galvanic sulphide oxidation as a metal-leaching mechanism and its environmental implications. *Geochem. Explor. Environ. Anal.* **2003**, *3*, 337–343. [CrossRef] [PubMed]

168. Li, Z.; Heping, L.; Liping, X. Galvanic interaction between galena and pyrite in an open system. *Chin. J. Geochem.* **2006**, *25*, 230–237. [CrossRef]

169. Liu, Q.; Li, H.; Zhou, L. Galvanic interactions between metal sulfide minerals in a flowing system: Implications for mines environmental restoration. *Appl. Geochem.* **2008**, *23*, 2316–2323. [CrossRef]

170. Fullston, D.; Fornasiero, D.; Ralston, J. Zeta potential study of the oxidation of copper sulfide minerals. *Colloid. Surf. A Physicochem. Eng. Asp.* **1999**, *146*, 113–121. [CrossRef]

171. Peter, J.M.; Scott, S.D. Mineralogy, composition and fluid-inclusion microthermometry of seafloor hydrothermal deposits in the Southern Trough of the Guaymas Basin, Gulf of California. *Can. Mineral.* **1988**, *26*, 567–587.

172. Zierenberg, R.A.; Fouquet, Y.; Miller, D.J.; Bahr, J.M.; Baker, P.A.; Bjerkgard, T.; Brunner, C.A.; Duckworth, R.C.; Gable, R.; Gieskes, J.; et al. The deep structure of a sea-floor hydrothermal deposit. *Nature* **1998**, *392*, 485–488. [CrossRef]

173. Berndt, C.; Hensen, C.; Mortera-Gutierrez, C.; Sarkar, S.; Geilert, S.; Schmidt, M.; Liebetrau, V.; Kipfer, R.; Scholz, F.; Doll, M.; et al. Rifting under steam—How rift magmatism triggers methane venting from sedimentary basins. *Geology* **2016**, *44*, 767–770. [CrossRef]

174. Paduan, J.B.; Zierenberg, R.A.; Clague, D.A.; Spelz, R.M.; Caress, D.W.; Troni, G.; Thomas, H.; Glessner, J.; Lilley, M.D.; Lorenson, T.; et al. Discovery of Hydrothermal Vent Fields on Alarcón Rise and in Southern Pescadero Basin, Gulf of California. *Geochem. Geophys. Geosyst.* **2018**, *19*, 4788–4819. [CrossRef]

175. Humphris, S.E.; Herzig, P.M.; Miller, D.J. *TAG-1 Area. Ocean Drilling Program: Leg 158 Preliminary Report*; Texas A&M University: College Station, TX, USA, 1996; pp. 65–140.

176. Moss, R.; Scott, S.D. Geochemistry and mineralogy of gold-rich hydrothermal precipitates from the Eastern Manus Basin, Papua New Guinea. *Can. Mineral.* **2001**, *39*, 957–978. [CrossRef]

177. Petersen, S.; Herzig, P.M.; Kuhn, T.; Franz, L.; Hannington, M.D.; Monecke, T.; Gemmell, J.B. Shallow Drilling of Seafloor Hydrothermal Systems Using the BGS Rockdrill: Conical Seamount (New Ireland Fore-Arc) and PACMANUS (Eastern Manus Basin), Papua New Guinea. *Mar. Geores. Geotechnol.* **2005**, *23*, 175–193. [CrossRef]